THESIS FOR THE DEGREE OF DOCTOR OF PHILOSOPHY

Improved Oxidation Resistance and Reduced Cr Vaporization from Thin-Film Coated Solid Oxide Fuel Cell Interconnects

Hannes Falk Windisch

Department of Chemistry and Chemical Engineering

CHALMERS UNIVERSITY OF TECHNOLOGY

Gothenburg, Sweden 2017

Improved Oxidation Resistance and Reduced Cr Vaporization from Thin-Film Coated Solid Oxide Fuel Cell Interconnects

HANNES FALK WINDISCH

Department of Chemistry and Chemical Engineering
Chalmers University of Technology
SE-412 96 Gothenburg
Sweden
Telephone + 46 (0)31-772 1000

Cover:
Scanning electron microscope images from broad ion beam milled cross-sections of the ferritic stainless steel Sanergy HT coated with 640 nm Co after 500 h of exposure in air-3% H_2O at 650 (left), 750 (middle) and 850 °C (right).

Improved Oxidation Resistance and Reduced Cr Vaporization from Thin-Film Coated Solid Oxide Fuel Cell Interconnects

Hannes Falk Windisch

Department of Chemistry and Chemical Engineering
Chalmers University of Technology

Abstract

High electrical efficiency, clean emissions, and the possibility to operate on a great variety of fuels, such as hydrogen, alcohols and hydrocarbons are some advantages of Solid Oxide Fuel Cell (SOFC) technology. Too short lifetimes and high production costs have, however, limited the commercialization of this technology. Volatilization of Cr(VI) species and the increased electrical resistance caused by a growing oxide scale are two major degradation mechanisms associated with the use of Cr_2O_3-forming ferritic stainless steels as interconnect material in a SOFC. In this thesis the possibility to mitigate Cr vaporization and improve oxidation resistance in a cost-effective way, by the application of thin-film metallic Co- and Ce/Co-coatings, was investigated. Uncoated and coated ferritic stainless steels were exposed for up to 3300 h at 650-850 °C. Cr vaporization, oxide scale growth, microstructural and chemical evolution of the oxide scales, as well as the effect these factors have on the electrical resistance of the oxide scale were studied. Cr vaporization was measured using the denuder technique. Oxide scale growth kinetics were studied mainly gravimetrically and the electrical scale resistance was measured ex-situ in an ASR setup using platinum as the electrode material. For chemical, structural and microstructural analysis, SEM/EDX, XRD, BIB/FIB, TEM/EELS and SIMS techniques were utilized. In order to study the oxide scale growth mechanism a two-stage, $^{18/16}$O-tracer exposure setup was used. Within the studied temperature interval it was shown that thin-film Co- and Ce/Co-coated ferritic stainless steels exhibit excellent properties as interconnect material in SOFCs. Cr vaporization can be mitigated with a Co-coating. The addition of a Ce-coating can improve the oxidation resistance, and thus decrease the electrical resistance of the oxide scale. The possibility to coat high volumes of steel using Physical Vapour Deposition (PVD) technology, and subsequently press the pre-coated steel into interconnects to allow for gas distribution, was also investigated. Cracks are formed within the coating as the coated steel is pressed into interconnects. The results in this study, however, show that these cracks are able to heal upon exposure at high temperatures.

Keywords: SOFC, Interconnect, Coating, Corrosion, Reactive Element, Cr Vaporization, ^{18}O-Tracer exposure

Acknowledgements

List of Publications

The thesis is based on the following papers, referred to by Roman numerals in the text:

Paper I

H. Falk-Windisch, J.-E. Svensson and J. Froitzheim

The Effect of Temperature on Chromium Vaporization and Oxide Scale Growth on Interconnect Steels for Solid Oxide Fuel Cells

Journal of Power Sources, Volume 287, 7 April 2015, Pages 25-35 (2015)

Paper II

A. Magraso; H. Falk-Windisch; J. Froitzheim; J-E. Svensson; R. Haugsrud

Reduced long term electrical resistance in Ce/Co-coated ferritic stainless steel for solid oxide fuel cell metallic interconnects

International Journal of Hydrogen Energy, Volume 40, Issue 27, 20 July 2015, Pages 8579–8585 (2015).

Paper III

H. Falk-Windisch, J. Claquesin, M. Sattari, J-E. Svensson and J. Froitzheim

Co- and Ce/Co-coated ferritic stainless steel as interconnect material for Intermediate Temperature Solid Oxide Fuel Cells

Journal of Power Sources, Volume 343, 1 March 2017, Pages 1-10 (2017)

Paper IV

H. Falk-Windisch, J. Claquesin, J-E. Svensson and J. Froitzheim

The effect of metallic Co-coating thickness on ferritic stainless steels intended for use as interconnect material in Intermediate Temperature Solid Oxide Fuel Cells

Submitted to Oxidation of Metals

Paper V

H. Falk-Windisch, M. Sattari, J-E. Svensson and J. Froitzheim

Chromium vaporization from mechanically deformed pre-coated interconnects in Solid Oxide Fuel Cells

Journal of Power Sources, Volume 297, 30 November 2015, Pages 217–223 (2015)

Paper VI

H. Falk-Windisch, I. Mertzidis, J-E. Svensson and J. Froitzheim

Pre-coated Ce/Co-coated steel: Mitigating Cr vaporization, increasing corrosion resistance at competitive cost

ECS Transactions, Volume 68, Issue 1, 2015, Pages 1617-1623 (2015)

Paper VII

H. Falk-Windisch, P. Malmberg, M. Sattari, J-E. Svensson and J. Froitzheim

^{18}O tracer experiments in combination with TEM and nanoSIMS to determine the oxide scale growth mechanism

Manuscript

Statement of author´s contribution

I was the main author of six of the seven papers this thesis is based on. In those six papers I was responsible for both the writing process and planning of the experiments. Moreover, I have also carried out the majority of the experimental work, including SEM/EDX and XRD analyses, with the following exceptions: In papers IV and VI a substantial part of the experimental work was carried out, under my supervision, by Ioannis Mertzidis and Julien Claquesin during their work for their master theses. Julien Claquesin has also conducted the ASR measurements in paper III. All TEM analyses shown in this thesis have been made by Mohammad Sattari and the SIMS analyses in paper VII were carried out by Per Malmberg. In paper II, I was the second author. For that paper I exposed all the samples that subsequently were electrically characterized by the main author, Anna Magraso. I was also involved in both the experimental planning, and in the writing process for this paper.

Related work:

The following papers are related to the work presented in this thesis:

Belma Talic, Hannes Falk-Windisch; Vinothini Venkatachalam; Peter Vang Hendriksen; Kjell Wiik; Hilde Lea Lein. *Effect of coating density on oxidation resistance and Cr vaporization from SOFC interconnects.* Submitted to Journal of Power Sources.

B.R. Sudireddy, J. Nielsen, Å. H. Persson, K. Thydén, K. Brodersen, S. Ramousse, D. Neagu E. Stefan, J.T.S. Irvine, H. Geisler, A. Weber, G. Reiss, R. Schauperl, J. Rechberger, J. Froitzheim, R. Sachitanand, H. Falk-Windisch, J. E. Svensson, M. W. Lundberg, R. Berger, J. Westlinder, S. Hornauer, T. Kiefer. *Development of robust metal supported SOFCs and stack components in EU-METSAPP consortium.* Submitted to Fuel Cells (EFCF Special Issue Series of FUEL CELLS) 2016.

Alnegren, P., Sachitanand, R., Nikumaa, M., Grolig, J., Falk Windisch, H., Sattari, M., Svensson, J.-E., Froitzheim, J. *Inhibiting chromium evaporation and oxide scale growth on SOFC metallic interconnects by nano coatings.* 20th World Hydrogen Energy Conference, WHEC 2014, Volume 1, 2014, Pages 423-426.

H. Falk-Windisch, J-E. Svensson and J. Froitzheim. *Influence of chromium evaporation and oxidation on interconnect steels at 650-850°C.* ECS Transactions, Volume 57, Issue 1, 2013, Pages 2225-2233.

Grolig, J.G., Abdesselam, H., Gas, M., Windisch, H.F., Froitzheim, J., Svensson, J.-E. *Copper based conversion coatings on ferritic stainless strip steel as solid oxide fuel cell interconnects: Oxidation performance and chromium evaporation.* ECS Transactions, Volume 57, Issue 1, 2013, Pages 2339-2347

Froitzheim, J., Magraso, A., Holt, T., Lundberg, M.W., Windisch, H.F., Berger, R., Sachitanand, R., Westlinder, J., Svensson, J.E., Haugsrud, R. *Nano coated interconnects for SOFC (NaCoSOFC).* ECS Transactions, Volume 57, Issue 1, 2013, Pages 2187-2193.

Preface

This thesis summarises most of the research carried out by the author, Hannes Falk Windisch, within the Swedish Competence Centre for High Temperature Corrosion (HTC), from 2012-2017. The work was performed within the Fuel Cell Group (FCG) at the Division of Energy and Materials at the Department of Chemistry and Chemical Engineering, Chalmers University of Technology, Gothenburg, Sweden, under the supervision of Professor Jan-Erik Svensson and Associate Professor Jan Froitzheim. The work was funded by the High Temperature Corrosion Centre (HTC), the Swedish Research Council, the Swedish Energy Agency, the Nordic NaCoSOFC project and the European Union's Fuel Cells and Hydrogen Joint Technology Initiative (METSAPP project).

List of acronyms

ASR	Area Specific Resistance
BIB	Broad Ion Beam
EDX	Energy Dispersive X-ray
EELS	Electron Energy-Loss Spectrometry
FIB	Focused Ion Beam
IC	Interconnect
LSCF	Lanthanum Strontium Cobalt Ferrite
LSM	Lanthanum Strontium Magnetite
MCO	Manganese-Cobalt Oxide
PVD	Physical Vapour Deposition
TEC	Thermal Expansion Coefficient
TEM	Transmission Electron Microscopy
SEM	Scanning Electron Microscopy
SIMS	Secondary Ion Mass Spectrometry
STEM	Scanning Transmission Electron Microscopy
SOFC	Solid Oxide Fuel Cell
XRD	X-Ray Diffraction
YSZ	Yttria Stabilized Zirconia

Table of Contents

1. Introduction

1.1 Background

The need to simultaneously meet the rapidly increasing demand for electricity, while reducing the emissions of greenhouse gases, is one of society's greatest challenges. Not only must more electricity be generated, the electricity also needs to be available, and reliable, everywhere on the globe. According to the International Energy Agency (IEA), in 2016 an estimated 1.2 billion people (16% of the global population) did not have access to electricity, most of them living in rural areas [1]. Fuel cells have emerged as a promising technology for clean and decentralized electricity production. Fuel cells generate electricity by converting chemical energy stored in the fuel through a chemical reaction, which makes them silent (no moving parts), clean (by avoiding combustion NO_x, SO_x, and particulate matter emissions are not created), and scalable (from portable systems to multi-MW installations). Furthermore, very high (>60%) electrical efficiencies have been demonstrated, not only in the lab, but also in kW systems [2]. Several types of fuel cells exist, however, the most common, and most mature, type of fuel cell today is the Proton Exchange Membrane Fuel Cell (PEM-FC). The PEM-FC has the advantages of high power density in combination with a low operating temperature (~80 °C). The low operating temperature allows these fuel cells to start up quickly, and results in less wear on the system during thermal cycling. The main disadvantages with this technique, however, are that the PEM-FC is limited to H_2 as a fuel, it is sensitive to contamination in the fuel (such as CO), and it requires expensive catalysts such as platinum [3]. In contrast to the PEM-FC, the Solid Oxide Fuel Cell (SOFC), which operates at high temperatures (> 600 °C), can utilize a large variety of fuels (H_2, biogas, natural gas, and even complex hydrocarbons such as diesel) without the need for expensive catalyst materials [2, 4-6]. The heat can also be utilized in Combined Heat and Power units (CHPs), allowing the waste heat from the SOFC stack to be used for heating a building's hot water loop, or alternatively for operating a gas turbine, thereby increasing the overall efficiency of the system.

A single cell consists of three components; an anode, a cathode and an electrolyte. To design a fuel cell system with a desired voltage, several cells must be connected in series to form a fuel cell stack. Each cell in the stack is separated and electrically connected by means of an interconnect. The interconnect material in a SOFC must fulfil several requirements, such as a Thermal Expansion Coefficient (TEC) similar to the other ceramic parts in the cell, be impermeable to gases, and possess a high thermal and electrical conductivity. The interconnect material must also be stable at high temperatures in both high and low pO_2 environments (air on the cathode side and fuel on the anode side) [7, 8].

Today, ferritic stainless steels that rely on the formation of a protective Cr_2O_3-scale are probably the most widely used type of interconnect material for planar SOFCs operating in temperature regimes between 600-850 °C. At such high temperatures two mechanisms that are associated to the interconnect material contribute to the rapid degradation of the fuel cell; increased electrical resistance due to a growing oxide scale [9] and poisoning of the cathode caused by volatilization of chromium (VI) species from the Cr-rich oxide scale at the interconnect surface

[10-13]. Custom-made, designed steels have been developed to improve the oxidation resistance, however, to mitigate Cr vaporization, these steels need to be coated. Furthermore, in order to avoid high electrical resistances caused by the coating, the coating material must possess high electrical conductivity at the desired operating temperature. Several types of coatings have been studied and proposed, but the most common type of coatings today are Manganese- (Mn) and Cobalt- (Co) based spinel (MCO) coatings. $(Co,Mn)_3O_4$-coatings have shown to mitigate Cr vaporization [14, 15], have a high electrical conductivity [16], and also have a matching TEC to the ferritic steel substrate [16, 17]. MCO-coatings can be applied using a variety of different techniques, such as wet powder spraying, dip-coating, screen printing, aerosol spray deposition, plasma spraying or with Physical Vapour Deposition (PVD) [15, 18-24]. Another alternative method for MCO-coatings is to coat the steel with metallic Co. This can be done by electroplating [25] or by a physical vapour-deposition method [26-29] etc. The metallic Co-coating is rapidly oxidized in air at elevated temperatures, forming a top-layer of Co_3O_4. If the steel contains Mn, the Co_3O_4 top-layer can convert into a $(Co,Mn)_3O_4$ top-layer, due to outward diffusion of Mn from the steel [25-27]. Moreover, by the application of coatings the oxidation resistance can also be improved. Reactive elements, such as Ce, La, Zr, and Y, are known to improve the high temperature oxidation resistance of Cr_2O_3-forming alloys [30, 31]. By adding reactive elements as a coating, the oxidation resistance of the steel can thus further be improved [25, 26, 32, 33].

Within the last decade custom-made designed alloys and the application of protective coatings have improved the performance of the SOFC, however, for SOFC technology to become commercially attractive the price per kWh has to be reduced. Material cost, power output and lifetime are considered to be important factors determining the price of this technology. It is therefore crucial to lower the production costs without reducing the efficiency and/or shorten the stack lifetime. The costs associated with the interconnect material can be significantly reduced by (1) using a more cost effective ferritic stainless steel and (2) by decreasing the total costs for coating the steel. Decreasing the operating temperature of the fuel cell would allow expensive specially designed steels to be substituted with cheaper steels that are produced in large volumes. Furthermore, today most coated interconnect materials are manufactured in two separate steps; (i) stamping the uncoated steel into the shape of the interconnect to allow for gas distribution, followed by (ii) coating the deformed steel plate in a second step. This two-step batch-coating concept is rather inefficient for mass production. By applying thin metallic coatings (e.g. thin Co-coatings), large volumes of steel can be pre-coated in a roll-to-roll process. The pre-coated steel coil can then be pressed into thousands of coated interconnects, which would allow for much more efficient large-scale production and lower overall cost.

1.2   Aim of this thesis

The principal aim of this thesis was to study the two degradation mechanisms, oxide scale growth and chromium (VI) species vaporization, in a typical SOFC cathode atmosphere, using uncoated and coated ferritic stainless steels as the interconnect material in SOFCs.

In order to make SOFCs commercially attractive it is crucial to lower production costs without reducing the performance of the SOFC stack. The work had a focus on improving the interconnect material (by the application of thin-film coatings) while at the same time reducing costs.

Today several SOFC manufacturers are manufacturing SOFC systems that operate within the temperature range of 600-700 °C, which is substantially lower than the common 750-850 °C for planar SOFC. As a consequence, limited data is available in this temperature region regarding Cr vaporization, oxide scale growth, and the effect a change in oxide scale microstructure has on the electrical scale resistance. A substantial part of this thesis was therefore aimed at studying the effect lower temperature has on these parameters (Papers I, III, and IV). Cost can also be reduced by using more cost-efficient coating methods. In papers V and VI the effects of pre-coating large volumes of steel and subsequently pressing the steel into interconnects was investigated. This would allow for high volume production and thus also for lower total costs of coated interconnects.

Furthermore, due to the very long expected lifetime of an SOFC (>40 000 h), accelerated tests must be developed to study the component materials. The method most frequently used to accelerate corrosion at elevated temperatures is to expose the material at a higher temperature than the normal operating temperature. For an accurate prediction detailed knowledge of the processes involved is necessary. Cr vaporization, oxide scale growth, electrical conductivity, microstructure and the chemical composition of the oxide scale are all differently affected by an increase in temperature. For this reason, the effect of temperature on all of these mechanisms was investigated in this thesis.

Finally, to improve high temperature corrosion, reactive elements such as Ce, La, and Y etc. can be added to the alloy, or as a coating. In papers II, III, and VI a substantial improvement in oxidation resistance was observed by the application of reactive element (Cerium) coatings. ^{18}O-tracer exposure experiments have previously been used to study the beneficial effect reactive elements have on Al_2O_3- and Cr_2O_3-forming alloys. However, due to limited lateral resolution, rough surface topography and thickness variation of the oxide scale over the analysed volume, SIMS depth profiling results are not entirely unambiguous and sometimes contradictory results can be found in the literature. The aim of paper VII was therefore to develop a method that eliminated these obstacles associated with conventional SIMS sputter depth profiles.

2. Theory

2.1 Fuel Cells

Fuel cells are electrochemical devices that generate electricity (and heat) by converting chemical energy stored in the fuel into electricity through a chemical reaction without combustion. They offer several advantages over traditional combustion technologies, such as high electrical efficiency, low emissions, scalability and for some types of fuel cells also high fuel flexibility [2-4]. Each cell is composed of two electrodes (an anode and a cathode) separated by an electrolyte. Similar to batteries, the principle of a fuel cell is to force electrons through an external circuit by utilizing an electrolyte material that is permeable to ions but not to electrons. When the cathode and the anode are electrically connected via an external circuit ion diffusion through the electrolyte will take place, driven by a concentration gradient. To maintain charge balance electrons give rise to a current in the external circuit [34]. An important difference between fuel cells and batteries is that fuel cells can generate electricity as long as fuel is available, unlike batteries which need to be recharged as the battery is discharged. These properties have made fuel cells highly attractive for most electrical applications ranging from small portable devices to large MW power plants. Today several types of fuel cells exist. These are generally classified according to the electrolyte material, since the type of electrolyte material determines which type of ions can diffuse across the electrolyte. Figure 1 illustrates the working principle of the most common fuel cell types.
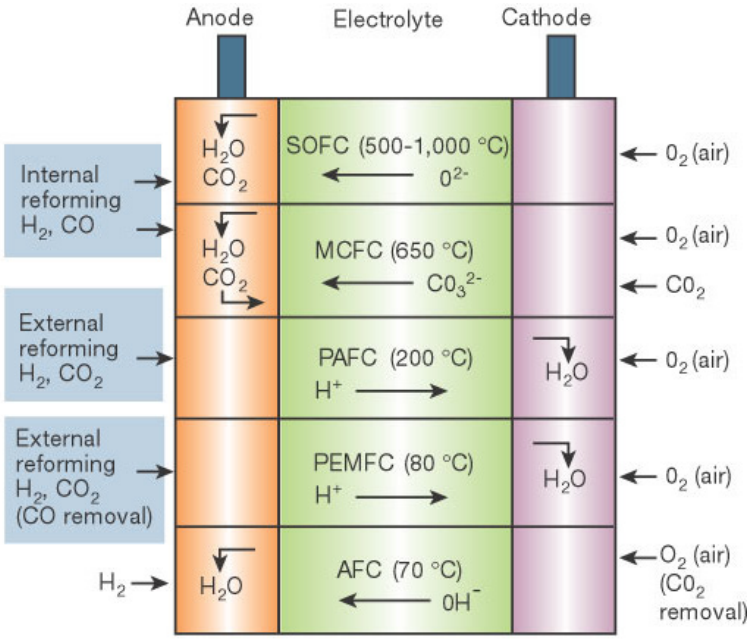
Figure 1: Some common types of fuel cells, their mobile ions and working temperatures. The image is reproduced with permission from [35].

The Polymer Exchange Membrane Fuel Cell (PEM-FC) has become the most common type of fuel cell today. The PEM-FC has the advantage that it operates at low temperature (~80 °C). Due to the low operating temperature, PEM Fuel Cells can be started up very quickly, making

4

them suitable for mobile applications. However, since the electrolyte material is a proton conductor, only H_2 can be used as a fuel. Furthermore, due to the low operating temperature, the PEM fuel cell is limited to expensive electrode materials such as platinum, which is sensitive to contamination in the fuel (such as CO) [3]. In contrast to the PEM-FC, the Solid Oxide Fuel Cell (SOFC), which operates at high temperatures (> 600 °C), can utilize a large variety of fuels (from H_2 to complex hydrocarbons such as diesel) without the need for expensive catalysts [4, 5].

2.2 Solid Oxide Fuel Cells (SOFCs)

The Solid Oxide Fuel Cell (SOFC) is based on an oxide-ion-conducting ceramic material as the electrolyte. The working principle of an SOFC during operation, using H_2 as the fuel, is illustrated in Figure 2. Oxidation of the fuel (half reaction 1) takes place on the anode side, where H_2 is oxidized into H_2O. Since the SOFC is based on an oxide-ion conducting electrolyte, carbon containing fuels can also be used as the fuel, and in that case the fuel is oxidized into both H_2O and CO_2. At the same time electrons are released and transferred through an external circuit to the cathode side where O_2 is reduced to O^{2-} (half reaction 2). The oxygen ions can then diffuse through the oxygen-ion-conducting electrolyte to the anode side, where half reaction (1) takes place again. The overall reaction, when hydrogen is used as the fuel, is shown in reaction (3) [34].

$$H_2 + O^{2-} \rightarrow H_2O + 2e^- \tag{1}$$

$$\tfrac{1}{2}O_2 + 2e^- \rightarrow O^{2-} \tag{2}$$

$$\tfrac{1}{2}O_2 + H_2 \rightarrow H_2O \tag{3}$$

Figure 2: Schematic drawing illustrating the operational concept of a Solid Oxide Fuel Cell (SOFC). Drawn by the author.

The oxygen-ion-conducting electrolyte enables the use of several types of fuels, such as H_2, NH_3, ethanol, natural gas, biogas and diesel. Furthermore, due to the high resistance towards impurities in the fuel, feedstocks such as coal and biomass can be gasified and used as the fuel in the SOFC [6]. The possibility to utilize a broad variety of fuels has made the SOFC an attractive candidate for a wide range of applications, ranging from a few kW in auxiliary power units to on-site power generation for residential and commercial applications and large scale MW SOFC power plants. Furthermore, very high electrical efficiencies (>60%) have been achieved for SOFC systems in the kW range [2]. Although the advantages of the SOFC are many, a few disadvantages, mainly associated with the high operating temperatures, such as chemical and mechanical degradation during long-term operation, too long start up times for mobile applications and mechanical failure during thermal cycling due to a mismatch in the thermal expansion coefficients between the different component materials in the fuel cell have limited its commercialization so far.

In order to make SOFCs commercially attractive it is generally stated that a lifetime of at least 40 000 h (~5 years) with a degradation rate of less than 0.5% per 1000 h must be guaranteed for stationary applications. Today several commercial systems can indeed guarantee 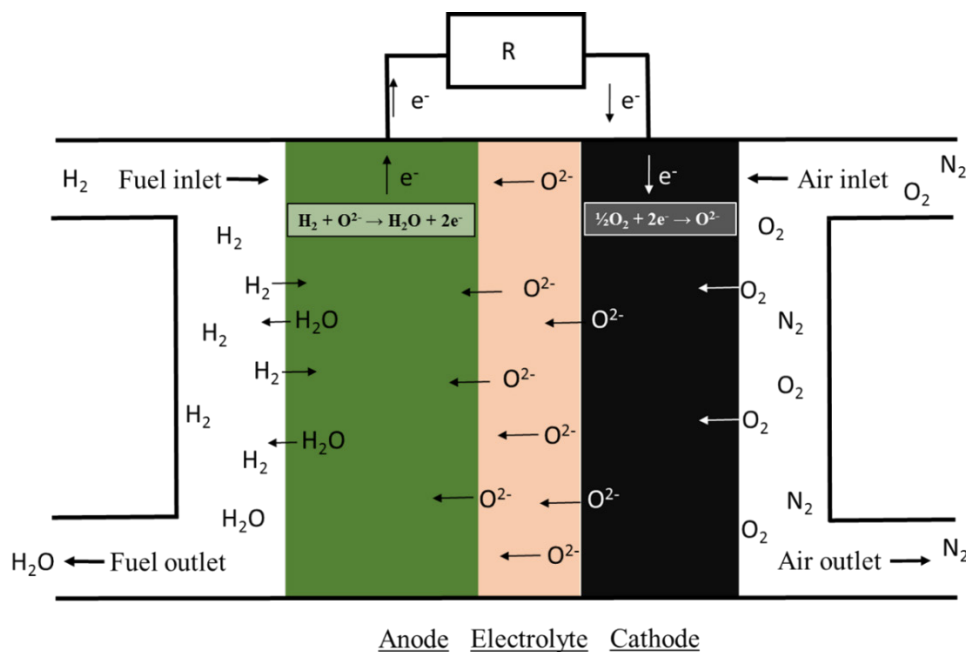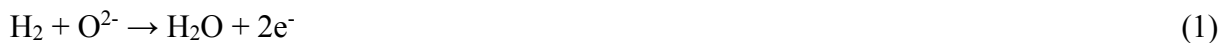such long lifetimes [36], however, expensive component materials are necessary, and as a consequence the cost for such a system is still very high. Furthermore, due to the great fuel flexibility of the SOFC, the SOFC is very attractive for mobile applications despite the issues mentioned above. However, shorter start up times and stable thermal cycling are two issues that need to be addressed before SOFCs can fully be an attractive power device for mobile applications.

Decreasing the operating temperature, improving the component materials and finding more economic manufacturing processes are therefore some of the most important steps towards real commercialization of the SOFC, both for stationary and mobile applications.

2.2.1 Electrolyte and electrode materials
The electrolyte material in SOFCs is an ionic conductor with a high oxygen-ion-conductivity and very low electrical conductivity. Furthermore, the electrolyte material must be stable in both oxidizing and reducing atmospheres and be impermeable towards gases (fuel on the anode side and air on the cathode side) [6]. The most common material today is Yttria Stabilized Zirconia (YSZ) [37]. In less common cases zirconia is stabilized with the significantly more expensive element scandia (ScSZ). For SOFCs intended to operate at lower temperatures Gadolina Doped Ceria (CGO) has become a popular alternative, enabling operation below 700 °C [5, 6]. At temperatures below 800 °C the ionic conductivity of doped Ceria is approximately one to two orders of magnitude greater than that of YSZ [38]. However, when Ceria-based oxides are subjected to reducing atmospheres Ce^{4+} can transform into Ce^{3+} leading to increased electronic conduction, and thus to higher leakage currents [39]. For this reason an electron blocking layer (such as YSZ) is frequently added between the doped Ceria electrolyte and the anode.

In contrast to the electrolyte, the electrodes must be porous (and remain so during operation at high temperatures) to allow for gas flow and to maintain a large catalytic surface area. The anode must be a good electrical conductor and catalytically active towards oxidation of the fuel.

A cermet consisting of nickel and the electrolyte material is considered to be the state of the art anode material today [37]. The cathode material must be catalytically active towards oxygen reduction, possess high oxygen-ion-conduction and be a good electrical conductor. Perovskite oxides, such as Strontium Doped Lanthanum Magnetite (LSM) and Lathanum Strontium Cobalt Ferrite (LSCF), are, therefore, frequently used as cathode materials [37].

2.2.2 The interconnect

The voltage from one single SOFC cell is only ~1 volt. To increase the total voltage of a fuel cell system several cells are connected in series, forming an array of single cells. Such an array of single cells is illustrated in Figure 3 and is called a stack. The interconnect (also frequently called a bipolar plate), is a current collector that separates the individual cells in a fuel cell stack. The main function of the interconnect is to electrically connect the anode to the cathode of the neighbouring cell and to separate the anode and cathode gases. This requires a gastight and electrically conductive material. The material must also be stable at high temperatures in both high and low,pO_2 environments (air on the cathode side and fuel on the anode side), chemically compatible with the electrode materials, and the Thermal Expansion Coefficient (TEC) of the interconnect material should be similar to the other ceramic parts in the stack to avoid mechanical failure during start up and cooling down. Furthermore, the material should be easy to shape and, since cost is a major obstacle to the commercialization of SOFCs, it is important that the material is inexpensive to manufacture in large volumes [7, 13].

Traditionally, ceramic materials such as doped-$LaCrO_3$ have been used as the interconnect material. However, the development of new and thinner electrolyte and electrode materials has enabled a decrease in SOFC operating temperature to below 900 °C, and as a consequence, ceramic interconnects have been replaced with significantly cheaper metallic interconnects. A wide range of alloys have been studied as possible candidates for use as interconnect material in SOFCs [7, 17, 40, 41]. From all the studied alloys, ferritic stainless steels, with a chromium content of 18-25 %wt. Cr, have become a very popular (probably the most popular) choice of interconnect material in Solid Oxide Fuel Cells today (see Section 3 for more details regarding the steels used as interconnect material today).

Although metallic interconnects have several advantages over ceramic ones, some challenges attributed to high temperature corrosion need to be improved to guarantee stable long-term performance. This is the topic of this thesis and will be discussed in more detail in the following sections.

7
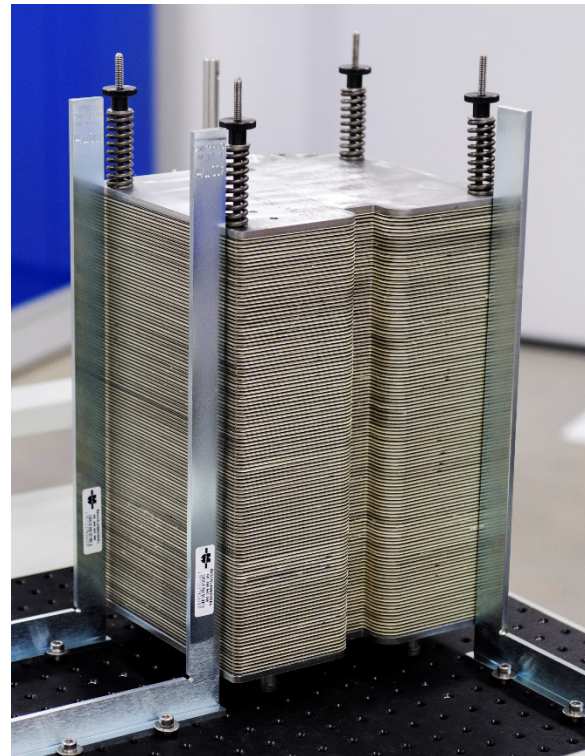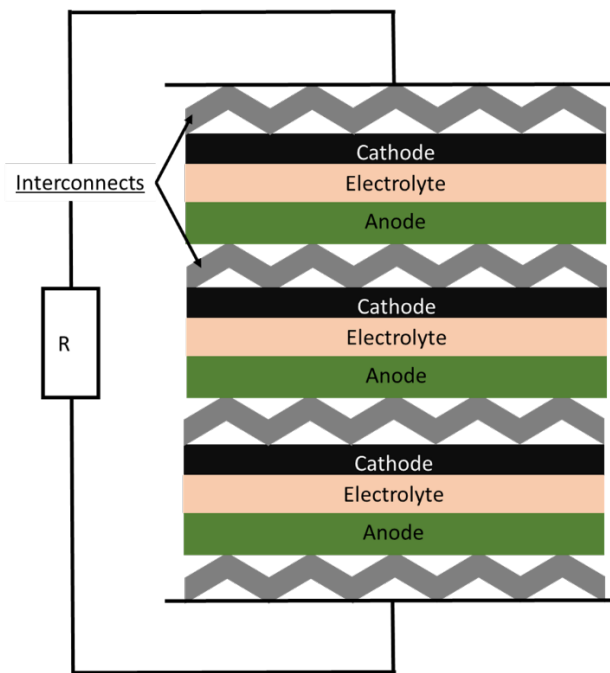
Figure 3: Left: A schematic drawing of a planar SOFC stack consisting of three cells separated and electrically connected with interconnects (drawn by the author). Right: A commercial 3kW stack (E3000), manufactured by Elcogen OY, Finland, consisting of 119 cells separated and electrically connected with interconnects [42].

2.3 Oxidation of metals

With the exception of a few noble metals, all metals oxidize according to reaction (4) when they are exposed to an oxygen-containing atmosphere [43]:

$$xM(s) + \frac{y}{2}O_2(g) \leftrightarrow M_xO_y(s) \tag{4}$$

For this reason the metal surface will immediately be covered by an oxide scale (metal oxide) that separates the metal from the oxygen-containing atmosphere (see Figure 5). For further oxidation of the metal to occur at least one of the reactants must penetrate the oxide scale [43].

2.3.1 Thermodynamics

Whether a metal will be oxidized or not at a certain temperature and in a certain environment can be predicted by thermodynamics. At constant temperature and pressure, Gibbs free energy can be utilized to measure the stability of a system according to equation (5) [44]:

$$G = H - TS \tag{5}$$

Where G is the Gibbs free energy, H is the enthalpy, S the entropy and T the absolute temperature. The change in Gibbs free energy determines if any reaction is spontaneous ($\Delta G < 0$), in equilibrium ($\Delta G = 0$) or non-spontaneous ($\Delta G > 0$). Three phases are important to consider when a metal oxidizes; the metal, the metal oxide, and the gas phase. The following equation can be utilized to reveal if a metal will oxidize or not (6):

$$\Delta G = \Delta G^0 + RT \ln K_{eq} = \Delta G^0 + RT \ln \frac{a_{(M_x O_y)(s)}}{a_{M(s)}^x a_{O_2(g)}^{\frac{y}{2}}} \tag{6}$$

Where ΔG^0 is the Gibbs free energy change at standard conditions, R is the gas constant and K_{eq} is the equilibrium constant for the reaction, which can be described in terms of quota of the activities for the products and reactants. Since the activity for pure solids can be considered to be 1 and the activity of a gas can be expressed as its partial pressure (p_{O_2}), the change in Gibbs free energy at a certain temperature can be expressed as a function of oxygen partial pressure, according to equation (7):

$$\Delta G = \Delta G^0 + RT \ln \frac{1}{p_{O_2}^{\frac{y}{2}}(g)} \tag{7}$$

This means that temperature and oxygen partial pressure determine if a metal will oxidize or not and which type of oxide is the most stable [45]. The stability of a metal oxide at a certain temperature and oxygen partial pressure can be illustrated using an Ellingham/Richardson diagram (Figure 4) [46]. It should be pointed out that there is an oxygen activity gradient across the oxide scale, giving rise to the possibility of a multi-layered structure, as is the case when pure iron oxidizes [47, 48].
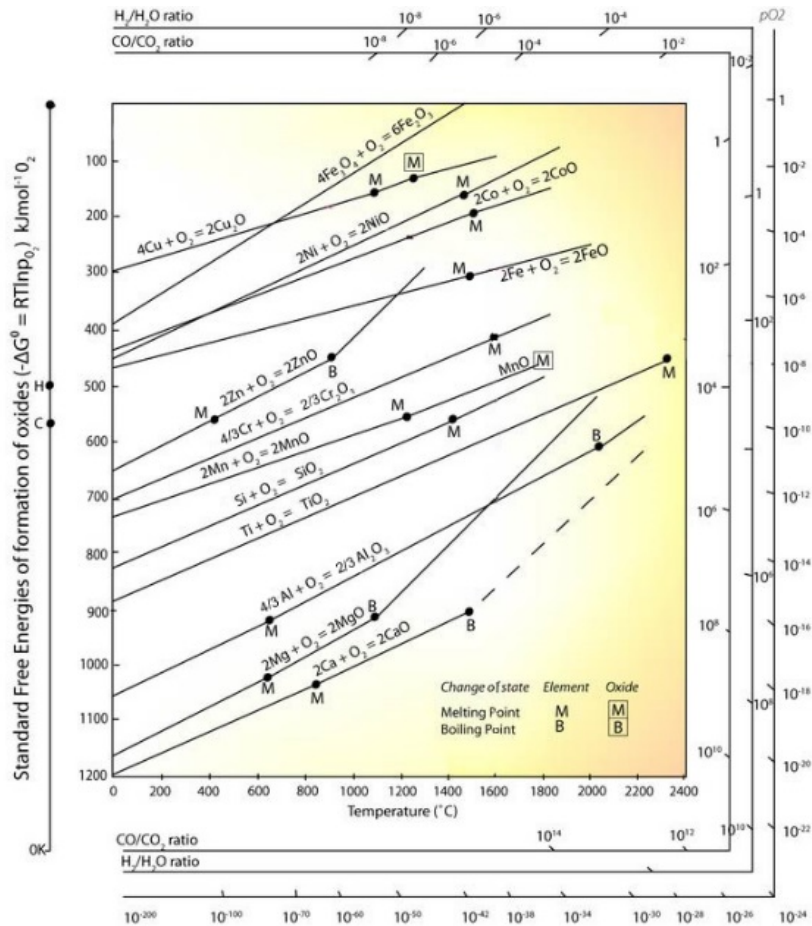
Figure 4: Ellingham/Richardson diagram for some metals and their metal oxides, reproduced with permission from [49].

2.3.2 Formation and growth of oxide scales

The formation and growth of an oxide scale can be separated into three steps, as illustrated in Figure 5 [43]. The first two steps are normally very rapid at high temperatures, and therefore step three is considered to be the rate determining step for continued scale growth.
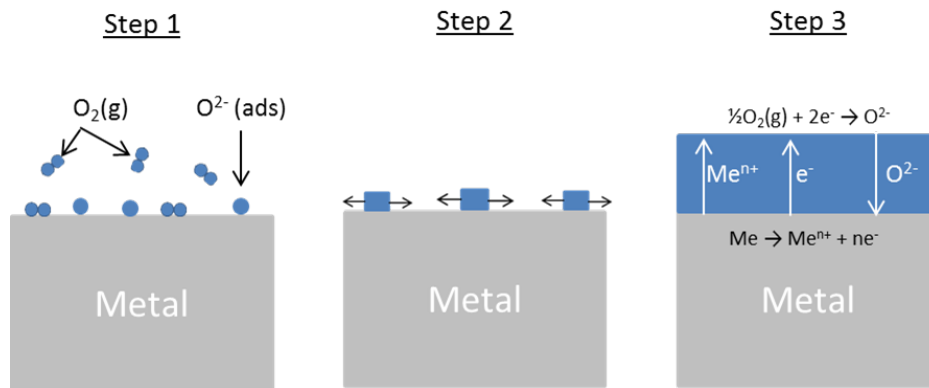
Figure 5: Schematic illustration of the formation (adsorption and oxide nucleation) and growth of an oxide scale, adapted from [43].

In step one, oxygen or water vapour molecules from the atmosphere adsorb on the metal surface. This weak physical adsorption of oxygen is followed by a charge transfer forming O^{2-} and Me^{n+} giving rise to an ionic bond between the oxygen and the metal. In step two, oxide formation of the metal oxide nucleus takes place at the metal surface. The growth of metal oxide nuclei then proceeds until a continuous layer of oxide covers the entire surface. From this stage on further oxidation can only take place by means of solid state diffusion through the oxide scale (step 3) [43].

Transient oxidation (the very beginning of the exposure):
For alloys containing several metals, all of the metals present at the surface will initially be oxidized (if the metal oxide is thermodynamically stable), forming a thin oxide scale rich in all the elements present at the surface of the alloy. Due to the fact that different metals also show different growth rates, the one with the highest growth rate will overgrow the other(s) (assuming the concentration is high enough). However, if the metal in the slow-growing oxide (A) is less noble than the metal in the fast-growing oxide (B), (A) will reduce the fast growing metal oxide (BO) according to following reaction (8):

A (in alloy) + BO → AO + B (in alloy) (8)

This reaction will proceed until the less noble metal (A) has formed a continuous oxide layer (AO). From this moment on, the rate-limiting step for further oxidation is determined by solid state diffusion through the slow growing oxide (AO), consisting of the less noble metal (A) [45, 48]. However, if the activity of the less noble metal (A) is too low no continuous oxide layer will form, and solid state diffusion through the fast growing oxide (BO) will be rate limiting [48].

Continued oxide scale growth:
Whether an oxide scale is fast- or slow-growing, primarily depends on the concentration of defects within the oxide scale [48]. Due to the minimization of free energy caused by the introduction of a certain amount of disorder, all crystalline materials contain defects, at all temperatures [50]. At higher temperatures more disorder is introduced to the oxide, and more defects will be created where diffusion can take place. These rules are true for all materials; however, fast-growing oxides contain more defects than slow-growing oxides. It is common to classify different oxides according to the predominant type of point defects, such as a metal/oxygen vacancy or interstitial, or a substitutional impurity atom [43, 48]. The two most common slow-growing oxides, Al_2O_3 and Cr_2O_3, are classified as stoichiometric oxides. This is because the only stable oxidation state for both of them is III (e.g. Al^{3+} and Cr^{3+}). As a consequence, the only significant types of defects are Schottky and Frenkel defects [43]. In comparison, iron (Fe) can be both Fe^{2+} and Fe^{3+}. By reducing Fe^{3+} in Fe_2O_3 to Fe^{2+} oxygen vacancies must be introduced into the crystal lattice to maintain charge neutrality. Such oxides are often referred to as anion-deficit oxides. Nickel oxide (NiO) provides another example of increased lattice defect concentration when a metal is stable in two oxidation states. Nickel normally forms Ni^{2+} in NiO, but can also be oxidized to Ni^{3+}. To maintain the charge balance

Ni^{2+} metal vacancies are created, and for this reason this type of oxide is referred to as a cation-deficit oxide. The formation of defects, such as cation or anion vacancies, in non-stoichiometric oxides can explain why alloys forming an oxide scale that consists of Fe or Ni-oxide tend to oxidize faster than alloys forming an oxide scale that consists of a stoichiometric oxide such as Al_2O_3 or Cr_2O_3. Although the prevalent type of lattice defects within the oxide scale is important to consider, non-lattice defects, such as dislocations and grain boundaries, also have a large impact on the rate of oxide scale growth. The diffusivity in polycrystalline materials can be ordered according to (9) [51]:

$$D \ll D_d \leq D_{gb} \leq D_s \tag{9}$$

Where D is the lattice diffusivity, D_d is the dislocation diffusivity, D_{gb} is the grain-boundary diffusivity and D_s is the diffusivity at the surface. This means that the fastest diffusion path through a dense oxide scale is via grain-boundary diffusion. For this reason, grain-boundary diffusion is commonly referred to as a short-circuit diffusion [43, 48]. Although grain-boundary diffusion is significantly faster than lattice diffusion, the volume in which grain-boundary diffusion can take place is normally small compared to the volume where lattice diffusion can take place. Furthermore, as the oxide scale grows grain coarsening is commonly observed, which will lead to fewer short-circuit paths. For the purpose of simplification, a general rule of thumb is that grain-boundary diffusion is the dominant diffusion path at temperatures below 0.6 of the melting temperature of the oxide [51], whereas at higher temperatures lattice diffusion is considered to be the dominant diffusion path. In this thesis Cr_2O_3-forming alloys were investigated at 650-850 °C. Cr_2O_3 has a melting temperature of 2265 °C in air according to Muan et al. [52], which means that grain boundary diffusion should be considered to be the main diffusion path according to this rule.

2.3.3 Oxidation kinetics
The growth of an oxide scale on a metal or alloy surface can be rather complex and is, in most cases, a mixture of several different mechanisms. Not only do ions diffuse within the lattice (as discussed above), but the flux of ions through a dense oxide scale is the sum of diffusion via the bulk, dislocations and grain boundaries. For this reason the combined oxidation process can be illustrated as a plot of oxide scale thickness against exposure time [43, 45, 48]. However, this has some practical limitations. A more common way to describe the oxidation process is instead to plot mass gain as a function of time, assuming that the gain in mass corresponds to the growth of an oxide scale [45]. Depending on the shape of such a mass gain plot, the growth of the oxide scale is commonly classified into linear, logarithmic or parabolic oxidation behaviour (Figure 6) [43, 45, 48].
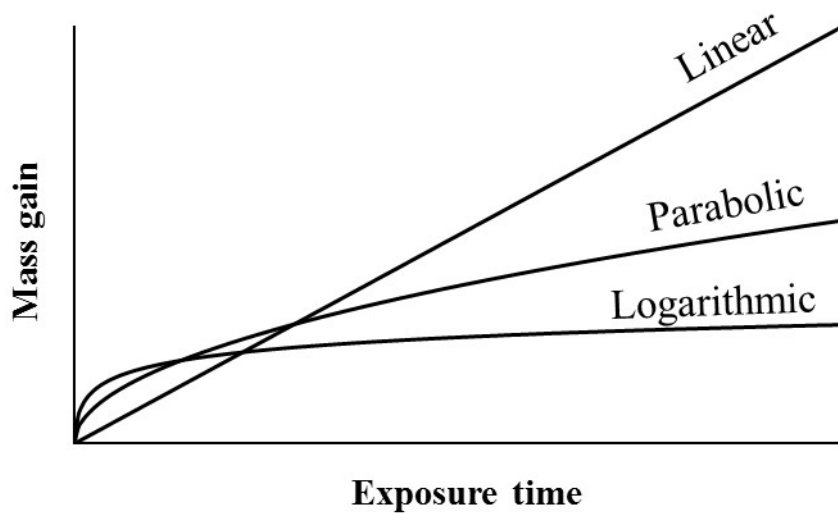
Figure 6: Mass gain curves illustrating linear, parabolic and logarithmic mass gain behaviour. Drawn by the author.

Linear rate law:
If the mass gain as a function of time is linear (Figure 6), the mass gain can be described according to (10):

$$\Delta m = k_l t \tag{10}$$

Where Δm is the mass gain, k_l is the linear rate constant and t is the exposure time. This behaviour is commonly observed under conditions where a surface or phase-boundary process is the rate-determining step [48]. In such a case, diffusion through the oxide scale is not the rate-limiting step, and therefore is commonly observed if the oxide is porous or very thin. Linear mass gain behaviour can also be observed if the thickness of the protective oxide scale is constant.

Logarithmic rate law:
If the mass gain as a function of time shows logarithmic behaviour (Figure 6), the mass gain is described according to the following equation (11):

$$\Delta m = k_{log} \log(t + t_0) + A \tag{11}$$

Where Δm is the mass gain, k_{log} is the logarithmic rate constant, t is the exposure time, and A is the integration constant. This is generally only observed at low temperatures and on extremely thin oxide scales [43, 48]. In this case electrons can be transferred from the metal to the gas-oxide surface by quantum mechanical tunnelling though the oxide scale. After a certain time period the oxide scale will become too thick for this mechanism to proceed. Due to the low temperatures, solid state diffusion will be too slow for continued growth, and the result will be that the rate drops to almost insignificant levels [48].

13

Parabolic rate law:

Alloys designed for high temperature applications commonly show parabolic oxidation behaviour (Figure 6). If an alloy shows parabolic behaviour the mass gain is described according to the following equation (12):

$$\Delta m^2 = k_p t + A \tag{12}$$

Where Δm is the mass gain, k_p is the parabolic rate constant, t is the exposure time and A is the integration constant. Parabolic behaviour is observed when oxide scale growth is controlled by solid-state diffusion through the scale [43, 45, 48]. The thicker the oxide scale becomes, the slower the diffusion though the scale, which leads to parabolic behaviour, and thus to equation 12. Parabolic behaviour is commonly associated with Carl Wagner's model for parabolic growth from 1933, which is based on the following assumptions: a continuous, well-adherent and dense oxide scale is formed; the growth rate is determined by solid-state diffusion; local equilibria exist at the metal-oxide and at the oxide-gas interfaces; and oxygen solubility in the metal/alloy is negligible [43].

Breakaway corrosion:

Breakaway or catastrophic corrosion is a term that refers to a certain mass gain behaviour, e.g. a parabolic mass gain behaviour that after a certain period of time is interrupted by a rapid increase in mass. Breakaway oxidation may result if the oxide grows parabolically to a critical thickness at which the cracking and the rupturing of the oxide reduce the thickness of the protective part [43]. Breakaway oxidation is also frequently observed when a protective oxide scale is transformed into a non-protective oxide scale by depletion of protective oxide-forming atoms, such as Cr in a chromia scale.

2.4 Cr Vaporization

For some oxides reaction between the oxide scale and the atmosphere can lead to the formation of volatile species, enabling the breakdown of the protective oxide scale [45, 53]. Chromium is such a metal. It forms volatile Cr(VI) species in an oxidizing atmosphere. In dry oxygen gaseous $CrO_3(g)$ will be formed according to reaction (13). At temperatures below 1000 °C the vapour pressure of $CrO_3(g)$ is rather low and the vaporization of the oxide scale will normally not be a critical issue [11]. However, if water vapour is present, as in air, volatile chromium oxyhydroxides can form. Several authors have shown that the most abundant volatile chromium oxyhydroxide species in air is $CrO_2(OH)_2$ [11, 54-56], which is formed according to reaction (14).

$$Cr_2O_3(s) + 1.5O_2(g) \rightarrow 2CrO_3(g) \tag{13}$$

$$Cr_2O_3(s) + 2H_2O(g) + 1.5O_2(g) \rightarrow 2CrO_2(OH)_2(g) \tag{14}$$
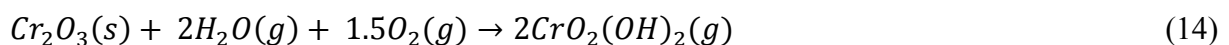
Hilpert et al. [11] have shown that even if the water vapour content is as low as 2% in air, $CrO_2(OH)_2(g)$ is still by far the most abundant Cr species at temperatures below 1000 °C (Figure 7).
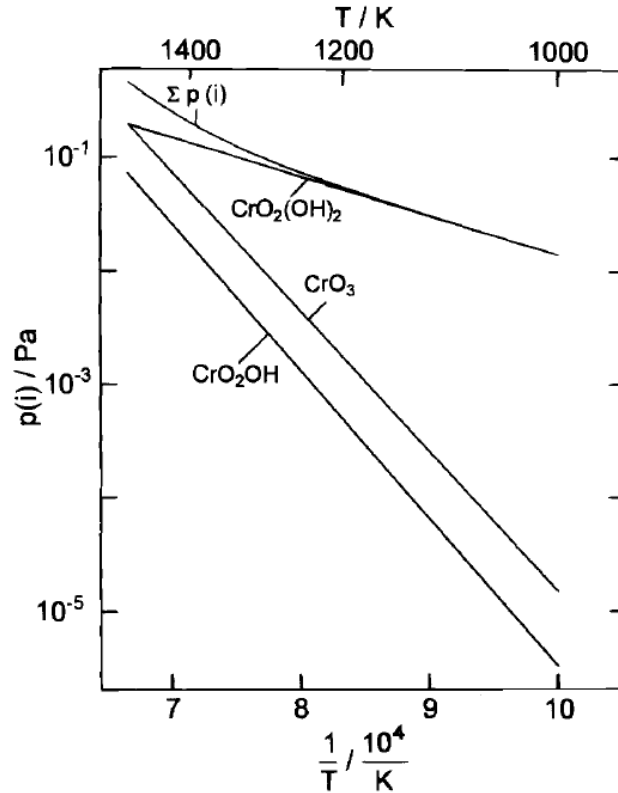
Figure 7: Partial pressures of the most abundant Cr-containing species over $Cr_2O_3(s)$ in humid air $[p(O_2) = 2.13*10^4$ Pa, $p(H_2O) = 2*10^3$ Pa] at different temperatures. This image was reproduced by permission of The Electrochemical Society, and is taken from publication [11].

Furthermore, the rate of Cr vaporization is dependent on the rate of gas flow. Figure 8 illustrates the effect of gas flow rate on Cr vaporization at 850 °C in air + 3% H_2O from a 21%wt. Cr ferritic stainless steel (Sanergy HT). If the gas flow rate is low, volatilization is proportional to the rate of gas flow (equilibrium regime). At higher flow rates a plateau can be observed (~6000 sml min^{-1}). This region is referred to as the flow-rate-independent region. At this stage the rate of Cr vaporization is instead limited by the kinetics of forming $CrO_2(OH)_2(g)$.
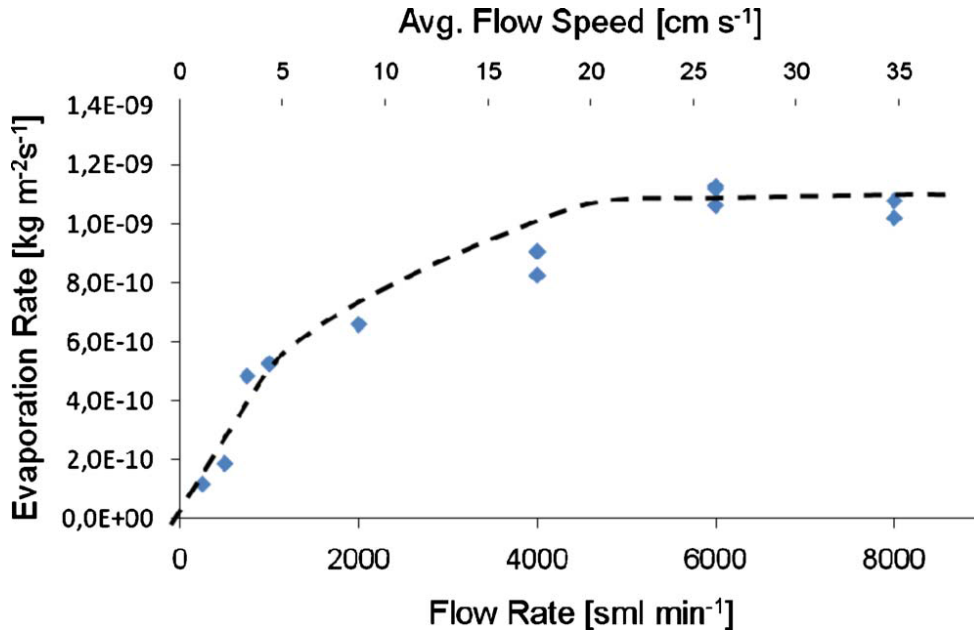
Figure 8: Rate of Cr vaporization as a function of gas flow rate at 850 °C in air + 3% H_2O on a 21% Cr steel (Sanergy HT). This image was reproduced by permission of The Electrochemical Society, and is taken from publication [57].

Paralinear oxidation

Vaporization of the oxide scale can have a significant influence on the oxidation behaviour. Tedmon [53] has described the phenomenon when a metal or an alloy shows parabolic oxide scale growth, but is simultaneously subjected to vaporization of the oxide scale. The total sum of the oxide scale thickness or mass gain is then a combination of two processes: (i) Parabolic oxide-scale growth by solid state diffusion through the oxide scale, and (ii) loss of the oxide scale due to volatilization. Initially, when the oxide scale is thin, scale growth is faster than vaporization, giving rise to parabolic oxidation behaviour. However, once a certain oxide scale thickness is reached, the oxide-scale growth rate is reduced to the same rate as the vaporization of the oxide scale. At this stage the oxide scale thickness remains constant. This gives rise to a mass gain behaviour called paralinear behaviour (see Figure 9). Initially mass gain behaviour is parabolic, but after a certain period of exposure parabolic mass gain behaviour turns into a linear mass loss, according to equation (15):

$$\Delta m = \sqrt{k_p t} - k_v t \tag{15}$$

Where Δm is the mass gain, k_p is the parabolic rate constant, k_v is the vaporization constant and t is the exposure time.
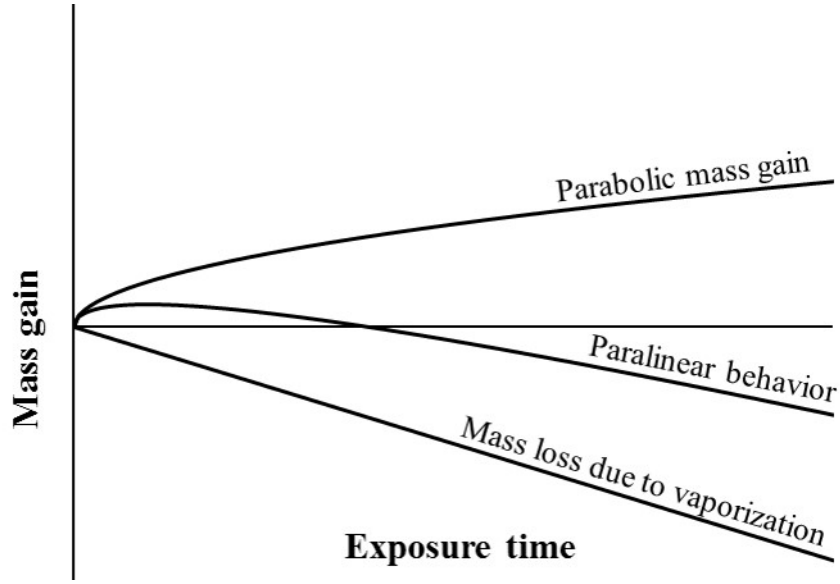
Figure 9: Paralinear mass gain behaviour illustrated as a combination of parabolic mass gain and linear mass loss due to vaporization. Drawn by the author.

2.5 Electrical conductivity of oxide scales

For metallic interconnects the electrical resistance caused by a growing oxide scale is of great importance. The total conductivity of a metal oxide is given by the sum of the conductivities of the electronic and ionic charge carriers according to equation (16) [43].

$$\sigma_{total} = \sigma_{ionic} + \sigma_{electronic} = \sigma_{total}(t_{el} + t_{ion}) \tag{16}$$

Where σ is the electrical conductivity, t_{el} is the transport number of electrons, and t_{ion} is the transport number of ions. Furthermore, the electronic conductivity is given by the sum of the conductivities due to electrons and holes, as shown in equation (17) [43].

$$\sigma_{electronic} = \sigma_{electrons} + \sigma_{electron\ holes} = e(nv_{electrons} + pv_{electron\ holes}) \tag{17}$$

Where n is the concentration of electrons, p is the concentration of electron holes, and $v_{electrons}$ and $v_{electron\ holes}$ are the mobility of electrons and electron holes, respectively. Both the concentration and the mobility terms are affected by the temperature. For electrical conductivity in oxides at elevated temperatures the concentration term is generally most important [43]. With increasing temperature the concentrations of electrons and electron holes increases. This results in a positive temperature dependency for oxides, which is in contrast to metallic conductors for which the conductivity decreases with increased temperature.

In this work the electrical resistance of thermally grown oxide scales formed on thin-film Co- and Ce/Co-coated Cr_2O_3-forming steels has been investigated. At high temperatures chromia is known to be an intrinsic semiconductor, whereas at temperatures below 1000 °C, which is the relevant temperature regime for this work, chromia is an extrinsic semiconductor [58]. In a thermally grown chromia scale an oxygen activity gradient throughout the oxide scale is assumed, and at the metal-oxide interface the oxygen activity is assumed to be the same as the equilibrium partial pressure for the metal oxide. In the case of a chromia scale the partial oxygen pressure at the metal-oxide interface should therefore be below 10^{-23} atm at 650-850 °C. Due

17

to the oxygen activity gradient in the chromia scale a thermally grown chromia scale can consist of both an inner n-type and an outer p-type chromia scale, which has been shown by Latu-Romain et al. [59]. Furthermore, it is not only the oxygen activity that has a strong influence on the electrical properties of the chromia scale. The doping of other cations can substantially influence the electrical conductivity of chromia [58, 60-62]. Apart from chromia the conductivity of Co-based spinel-type oxides is also relevant for this work. Spinel-type oxides are generally believed to conduct by hopping of charge between octahedral sites, and if the octahedral sites are occupied by cations of mixed valence the electrical conductivity may be further increased [16]. Spinel oxides based on cobalt, which is the type of spinel oxides formed on the Co- and Ce/Co-coated materials, possess significantly higher electrical conductivity at 650-850 °C than chromia [16, 58, 60]. Due to the complexity of the oxide scales only the total resistance of the oxide scale is normally measured, which commonly is expressed as Area Specific Resistance (ASR). In equation (18) it can be seen that the ASR is the resistance multiplied by the area.

$$ASR = R * A \tag{18}$$

Where ASR is the Area Specific Resistance, R is the resistance, and A is the area.

If the thickness of the oxide scale is known, the ASR value can be transferred into the electrical conductivity according to equation (19):

$$\sigma = \frac{L}{ASR} \tag{19}$$

Where σ is the electrical conductivity, L is the thickness of the oxide scale, and ASR is the measured Area Specific Resistance. For a more detailed description regarding the ASR measurements see Section 4.4.

3. Corrosion in association to ferritic stainless steels as interconnect material in SOFCs

The main function of the interconnect is to electrically connect the cells within a stack. Since the current will pass through the interconnect-electrode interface, the growth of an oxide scale is by far the largest contribution of the interconnect to the electrical resistance, if steels are used as the interconnect material (the resistance of the steel can be neglected). Steels that form a protective layer of electrically insulating Al_2O_3 or SiO_2 have therefore been excluded as possible candidates for the interconnect material in SOFCs, despite their excellent high temperature corrosion resistance. Instead, Cr_2O_3-forming alloys (Cr_2O_3 is a semiconductor) have become the most popular choice of interconnect material for planar SOFCs operating at 600-850 °C. Moreover, steels that form a protective Cr_2O_3 scale are generally considered to possess good high-temperature corrosion resistance in air. The problem remains that SOFC systems must guarantee a lifetime of at least five years without major degradation rates. During such long operating periods thick Cr_2O_3-scales are formed at the surface of the interconnect. The growth of a thick Cr_2O_3 scale leads to an increased electrical resistance, which results in decreased performance of the fuel cell. For this reason, improving the high temperature corrosion resistance of Cr_2O_3-forming steels is crucial to enable stable long-term performance, and also to prevent breakaway corrosion, which would lead to very rapid degradation of the SOFC. Furthermore, when Cr_2O_3-forming steels are used as the interconnect material in SOFCs a second degradation mechanism causing rapid degradation of the fuel cell is observed. On the cathode side, which contains both oxygen and water vapour, volatile Cr(VI) species, such as $CrO_2(OH)_2$, vaporize from the Cr-rich surface oxide scale (see section 2.4) [11, 54-56]. The volatile Cr(VI) species are then transported to the cathode where they may either be reduced back to Cr(III) at the Three Phase Boundary (TPB), forming deposits that block the electrochemical oxygen reaction process, or directly react with other stack components [10, 13, 63, 64]. Both cases lead to fast stack degradation [63, 65], and for this reason it is of great importance to minimize Cr vaporization.

3.1 Steels specially developed as interconnect material in SOFCs

Chemical composition, steel microstructure and surface pre-treatment are some of the most important factors that determine if a steel will demonstrate protective behaviour (slow growing oxide scale) or not in a certain environment. Crofer 22 APU, Crofer 22 H, Sanergy HT and ZMG232 G10 are four of the most common commercially available ferritic stainless steels that are custom-made as interconnect material for SOFCs. These steels have four things in common: (i) To ensure the formation and growth of a protective Cr_2O_3-layer during long-term operation of the SOFC these steels contain approximately 22%wt. Cr. A higher amount of Cr may further improve long-term corrosion resistance; however, brittle sigma phase may form during operation, which is undesirable. (ii) Due to the requirement for low electrical resistance, the formation of a continuous layer of SiO_2 must be avoided. For this reason the Si content in the two steels, Crofer 22 APU and ZMG232 G10, is very low. However, due to the lack of Si, these steels are produced using a special vacuum melting procedure. This process is expensive and therefore Nb and Mo or W is added to the two steels Sanergy HT and Crofer 22 H. These alloy

elements form Laves-phase (e.g. $(Fe,Cr)_2(Nb,W,Mo)$) precipitates that bind the Si. The formation of Laves-phase precipitates also increases the high temperature creep strength of the steel. (iii) Small amounts of Mn (0.3 - 0.5%wt) are added for the formation of a continuous $(Cr,Mn)_3O_4$ top-layer, which reduces the vaporization of Cr species [66]. (iv) All four steels contain small amounts of Reactive Elements (RE). The addition of reactive elements, such as Ce, La, Y, Hf and Zr, is known to significantly improve the high temperature corrosion resistance of Al_2O_3- and Cr_2O_3-forming steels [30, 67-69]. This will be discussed in more detail in section 3.3.

Alloys other than the four mentioned steels are frequently used as interconnect material in SOFCs. One of these is the Cr-based ODS alloy developed by Plansee, Austria (CFY interconnect). This material is based on chromium and contains approximately 5%wt. Fe, as well as a small amount of oxide dispersions such as Y_2O_3. This alloy is manufactured through a powder metallurgical process. Although this material shows very high corrosion resistance, in combination with excellent mechanical properties, the price for this material is very high. To be able to guarantee a lifetime of more than five years, with a very low degradation rate, several fuel cell manufacturers are willing to pay this price today. However, in order to reduce costs, other SOFC developers are searching for significantly cheaper interconnect materials. In fact, the four ferritic stainless steels specially developed as interconnect material for SOFCs (Crofer 22 APU, Crofer 22 H, Sanergy HT and ZMG232 G10) are often considered as too expensive, since these steels are only produced for SOFC applications (small quantities). A strong driving force therefore exists to replace these custom-made interconnect steels with significantly cheaper steels that are already available in large volumes on the market. Some of the steels that have been considered as alternative interconnect materials in order to reduce cost are the two alloys AISI 441 and AISI 430, which are ferritic stainless steels containing approximately 16-18% Cr and small amounts of Mn. These steels are primarily intended for SOFCs operating at lower temperatures, whereas the Cr-based ODS alloy is mainly used in SOFCs that are operating at higher temperatures.

3.2   Coatings to mitigate Cr vaporization

As mentioned in the previous section, ferritic stainless steels developed as interconnect material for SOFCs have been alloyed with small amounts of Mn to promote the formation of a continuous $(Cr,Mn)_3O_4$ top layer. This has been shown to reduce Cr vaporization by a factor of 2-3 compared to alloys that form a top layer consisting almost entirely of Cr_2O_3 [66, 70]. However, significant amounts of Cr are still vaporized from the $(Cr,Mn)_3O_4$ top layer, which poisons the cathode [63, 65]. Therefore, the Cr vaporization rate must be decreased further to enable stable long-term performance. Today the majority of all interconnect steels are coated with either a ceramic or a metallic coating. Metallic coatings are oxidized at elevated temperatures in air, and thus are turned into ceramic coatings (conversion coatings) [27, 28]. Due to the requirement for low electrical resistance the ceramic coating must be a good electrical conductor at the desired operating temperature. It is also important for the coating not to have a negative effect on the oxidation-resistance of the steel, since a thicker Cr_2O_3 scale would lead to a higher electrical resistance of the interconnect, even though the coating material possesses high electrical conductivity.

Within the last decade hundreds of peer reviewed papers have been published investigating different coating materials as well as different deposition techniques. However, from all these studies very few actually contain any Cr vaporization measurements proving that the suggested coating actually mitigates Cr vaporization. One of the very first (from 2006) peer reviewed papers presenting Cr vaporization measurements from both uncoated and coated SOFC interconnect materials was published by C. Collins et al. [71]. In that study it was shown that a Co-Mn spinel coating, deposited using physical vapour deposition, was able to lower the rate of Cr vaporization by a factor of 2-3 compared to the uncoated Crofer 22 APU material at 800 °C in humid air. Shortly after, Stanislowski et al. [28] and Kurokawa et al. [14] published Cr vaporization measurements showing that both perovskite and spinel coatings, as well as metallic conversion coatings, can mitigate Cr vaporization.

In the study by Stanislowski et al. [28] metallic Co- and Ni-conversion coatings (forming Co_3O_4 or NiO during the exposure) were able to lower the Cr vaporization rate by two orders of magnitude, compared to the uncoated material, during an exposure time of 1200 h at 800 °C. However, from the four perovskite coatings, only the $La_{0.99}(Cr_{0.77}Mg_{0.05}Al_{0.18})O_3$ coating was able to reduce Cr vaporization by a factor of 4 without spalling off the substrate. In the study by Kurokawa et al. [14], however, it was shown that both perovskite coatings (LSM and LSCF) and Co-Mn spinel coatings are able to reduce the Cr vaporization rate by more than one order of magnitude. In fact, the density of the coatings was the main criteria determining the effectiveness of the coating with respect to Cr vaporization, not whether it was a spinel or a perovskite coating. Nevertheless, the exposure duration in the study by Kurokawa et al. [14] was less than 24 h, which is too short to be able to draw any conclusions about the long-term effectiveness of these materials. Although perovskite coatings have been, and still are, studied intensively, Co- and Mn-based spinel coatings are probably the absolute most common coating material for interconnects in SOFCs today. This type of material can supress Cr vaporization during long-term exposures [26-28, 32, 57, 72]. Moreover, the electrical conductivity at elevated temperatures is high [16], and some authors have also seen that these coatings have the potential to improve the oxidation resistance of the steel [25, 29, 73].

Co- and Mn-based spinel coatings can be applied by a great number of techniques, such as spray drying, dip-coating, screen printing, aerosol spray deposition, plasma spraying or Physical Vapour Deposition (PVD) [15, 18-24]. However, as has been shown in several studies [27, 28, 74, 75], the steel can be coated with metallic Co, which upon oxidation is converted into a Co_3O_4 top-layer. Due to the high temperature, and the presence of Mn in the steel (most interconnect steels contain Mn), this Co_3O_4 top-layer is, with prolonged exposure time, enriched in Mn and as a consequence transformed into $(Co,Mn)_3O_4$ [25, 27, 72, 76].

3.3   Reactive elements as a way to improve oxidation resistance

Limiting the Cr_2O_3 scale thickness is absolutely crucial, due to the low electrical conductivity of Cr_2O_3 [58]. Additions of reactive elements, such as Ce, La, Y, Hf, and Zr, are known to significantly improve oxidation resistance in Al_2O_3- and Cr_2O_3-forming alloys [30, 68, 69]. Several mechanisms have been proposed in an attempt to explain the reactive element effect [30, 31]. The most widespread theory suggests that undoped Cr_2O_3 grows by a combination of metal outward and oxygen inward diffusion, with the former being the dominant mechanism.

Doping with reactive elements causes a segregation of the reactive elements at the Cr_2O_3 grain boundaries [77, 78]. This impedes metal outward diffusion and, as a consequence, the smaller flux of oxygen ions becomes the dominant mechanism for scale growth [67, 77]. Not only is a slower oxide scale growth rate commonly observed as reactive elements are added to the material, the addition of reactive elements often improves scale adhesion as well [32, 69]. Improved scale adherence, due to the addition of reactive elements, may be associated with improved interfacial chemical bonding and the possibility of gettering sulphur, as well as other impurities known to worsen scale adhesion [30]. Furthermore, since reactive elements are often added to the alloy, e.g. as oxide dispersions, they may also change the mechanical properties, as well as the grain size, of the bulk alloy. A change in mechanical properties of the bulk material may influence the scale adhesion. A smaller alloy grain size could also lead to more a more rapid supply of chromium to the metal-oxide interface during the transient oxidation phase. Moreover, studies have also shown that treating the surface with the reactive elements [77, 79] or by coating the alloy with a thin layer of a reactive element [32, 33] can significantly improve the oxidation resistance of the material and improve the scale adherence [32]. Although oxidation resistance may be improved by the addition of a reactive element coating, Cr vaporization is not reduced [32]. Adding reactive elements in the form of a coating for SOFC interconnects must therefore be combined with a second coating, such as Co-Mn spinel or metallic Co, which mitigates Cr vaporization, as discussed in the previous section. In our group at Chalmers University of Technology several studies have been carried out where ferritic stainless steels have been coated (by PVD) with dual layered coatings, consisting of either a thin layer of Ce or La, followed by a top-layer of Co [26, 32, 80-82]. These dual layered coatings have shown to both reduce Cr vaporization and improve oxidation resistance at 850 °C. In the results and discussion part of this work (Section 5), it will be shown that these dual layered Ce/Co-coatings also show excellent properties at lower temperatures (650 and 750 °C). Combined reactive element and Co-coatings can also be applied by other coating techniques. Harthoj et al. [25] showed that the oxidation resistance can be improved, causing a lower electrical resistance, by co-depositing CeO_2 particles in the electrodeposited Co-coating, and Qu et al. [83, 84] showed that oxidation resistance can be improved by combining Ce or Y with Co, using sol-gel dip-coating to deposit the Co-, Ce/Co-, and Y/Co-coatings on a ferritic stainless steel.

4. Materials and methods

4.1 Investigated materials

Table 1 shows the composition of the five ferritic stainless steels and the Fe-Cr model alloy studied within this thesis.

TABLE 1: Composition of the studied alloys in weight%, as specified by the manufacturer for the batches used.

Material	Manufacturer	Fe	Cr	C	Mn	Si	Mo	W	Nb	Ti	Add
Sanergy HT Batch: 531816 **Papers I, II, and III**	AB Sandvik Materials Technology	Bal.	22.4	0.01	0.25	0.07	0.93	<0.01	0.41	0.06	Zr
Sanergy HT Batch: 518053 **Paper IV**	AB Sandvik Materials Technology	Bal.	21.2	0.04	0.3	0.12	0.96		0.71	0.09	Zr
Crofer 22 H Batch: 161061 **Paper I**	ThyssenKrupp VDM	Bal.	22.9	0.007	0.4	0.2		1.9	0.5	0.07	La
Crofer 22 APU Batch: 1732288 **Papers IV and V**	ThyssenKrupp VDM	Bal.	22.9	0.004	0.38	0.01				0.06	La
AISI 441 Batch: 064313 **Paper VI**		Bal.	17.7	0.015	0.30	0.55			0.37	0.15	
Model alloy **Paper VII**	MaTeck	80	20								

All samples, were cut into 15 x 15 mm^2 coupons. Crofer 22 H and the two batches of Sanergy HT (531816 and 518053) had a steel thickness of 0.2 mm, whereas the thickness of Crofer 22 APU and AISI 441 was 0.3 mm. The thickness of the Fe20Cr model alloy, before grinding and polishing, was 1 mm. Except for the model alloy, all other samples were exposed in an as-received state after being cleaned in acetone and ethanol using an ultrasonic bath. The same cleaning process was also used for the model alloy, after this material had been ground and polished.

In all papers, with the exception of paper I, coated materials (Ce-, Co-, and Ce/Co-coatings) were investigated. All coatings were prepared at AB Sandvik Materials Technology using a Physical Vapour Deposition (PVD) process. The Ce-coatings can be considered as a layer of Ce-oxide, since Ce requires extremely low pO$_2$ pressures in order not to oxidize. In Papers V and VI some of the materials had been mechanically deformed prior to exposure, with the aim of investigating the effect of mechanical deformation upon Cr vaporization and oxidation. For a more detailed description of the mechanical deformation procedure for the different materials see papers V and VI.

4.2 Furnace exposures

Two different furnace setups have been used within the work of this thesis. All exposures in papers I-VI were carried out in a horizontal tubular quartz reactor (Figure 10), whereas the ^{18}O-tracer exposures in Paper VII were carried out in a different setup, where the samples were hanging in a vertical quartz reactor (Figure 12).
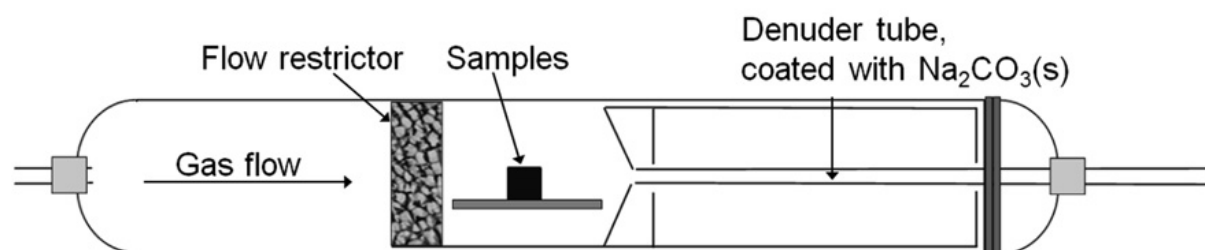
Figure 10: Schematic drawing of the experimental setup (except for Section 5.4 and paper VII). The Figure is reproduced by permission of The Electrochemical Society and is taken from [57].

Since the focus of this thesis was corrosion at the cathode side of the interconnect, all exposures were carried out under oxidizing (high pO$_2$) conditions. In section 5.4, and in paper VII, all exposures were carried out in an atmosphere containing Ar with 20% O$_2$ and ~1% H$_2$O. The samples were exposed in a closed system without any flow, except natural convection, in order to eliminate ^{16}O contamination during the ^{18}O-exposure. In paper IV all samples were also exposed in a stagnant atmosphere, however, in contrast to paper VII, the exposure atmosphere in paper VI was laboratory air.

In all the other papers (I, II, III, V and VI), the samples were exposed in an air-3% H$_2$O atmosphere. 3% H$_2$O was achieved by bubbling dried and cleaned air through a warm water bath connected to a condenser, which was set at 24.4 °C. The flow rate was set to 6000 sml min^{-1} to ensure a flow-independent regime in the reactor (see Figure 8, Section 2.4). In order to

minimize natural convection, and to ensure a more uniform flow pattern, a porous silicon carbide flow restrictor was placed in front of the samples.

4.3 Cr vaporization measurements (the denuder technique)

In Papers I, III, V, and VI the denuder technique was used to collect volatile chromium (VI) species. This technique is based on the reaction between sodium carbonate and volatile chromium species. Figure 10 shows that a denuder tube (made out of quartz) is placed behind the samples to act as the reactor outlet. The inside of the denuder tube is coated with $Na_2CO_3(s)$, and, as volatile Cr(VI) species, formed at the sample surface, are transported with the gas stream through the coated denuder tube, sodium chromate is formed according to reaction (20).

$$CrO_2(OH)_2(g) + Na_2CO_3(s) \rightarrow Na_2CrO_4(s) + H_2O(g) + CO_2(g) \tag{20}$$

This is a simple, but also a very efficient, method to collect volatile chromium species. By using the denuder technique a collection efficiency of $95 \pm 5\%$ can be achieved [57]. A second advantage of this technique is that the denuder tube can be replaced regularly and rinsed with water, without affecting the samples. The amount of vaporized Cr is then quantified using spectrophotometry (Evolution 60S, Thermo Scientific). A more detailed description of the denuder technique can be found elsewhere [57].

Cr vaporization measurements from pure Cr_2O_3:
Cr vaporization was measured from a 15 x 15 mm^2 sample of pure Cr_2O_3 (supplied by MaTeck, Germany). The exposure was carried out in a non-isothermal manner (the same manner as for the uncoated Sanergy HT and Crofer 22 H materials in Figure 22).

4.4 Area Specific Resistance (ASR) measurements

Area Specific Resistance (ASR) measurements were conducted in papers II-IV, with the aim of measuring the electrical resistance associated with the thermally grown oxide scales formed on the materials investigated, at temperatures between 650-850 °C. Today there are no standards for how to measure electrical scale resistance; instead each research group has their own way of measuring the ASR. In this work Platinum (Pt) was used as the electrode material, and all ASR measurements were conducted ex-situ (on exposed samples) in order to avoid any effect of the platinum electrode material, which has previously been observed by Grolig et al. [81]. The ASR measurements in paper II were carried out at SMN/FERMiO, University of Oslo in Oslo, Norway, whereas the ASR measurements in papers III and IV were carried out in our lab at Chalmers University of Technology, Sweden (see Figure 11). In both setups, the exposed samples were mounted in a ProboStat™ (NorECs, Norway) measurement cell using Pt wire and grid to contact the sample electrodes. The resistance was measured by the 2-point 4-wire method at 650-850 °C in air. To check for semiconductive behaviour the ASR was monitored as the samples cooled down. The electrical resistance is characterized by the ASR, which is the measured resistance (R) multiplied by the contact area (A). For a more detailed description of the method, see the corresponding papers.
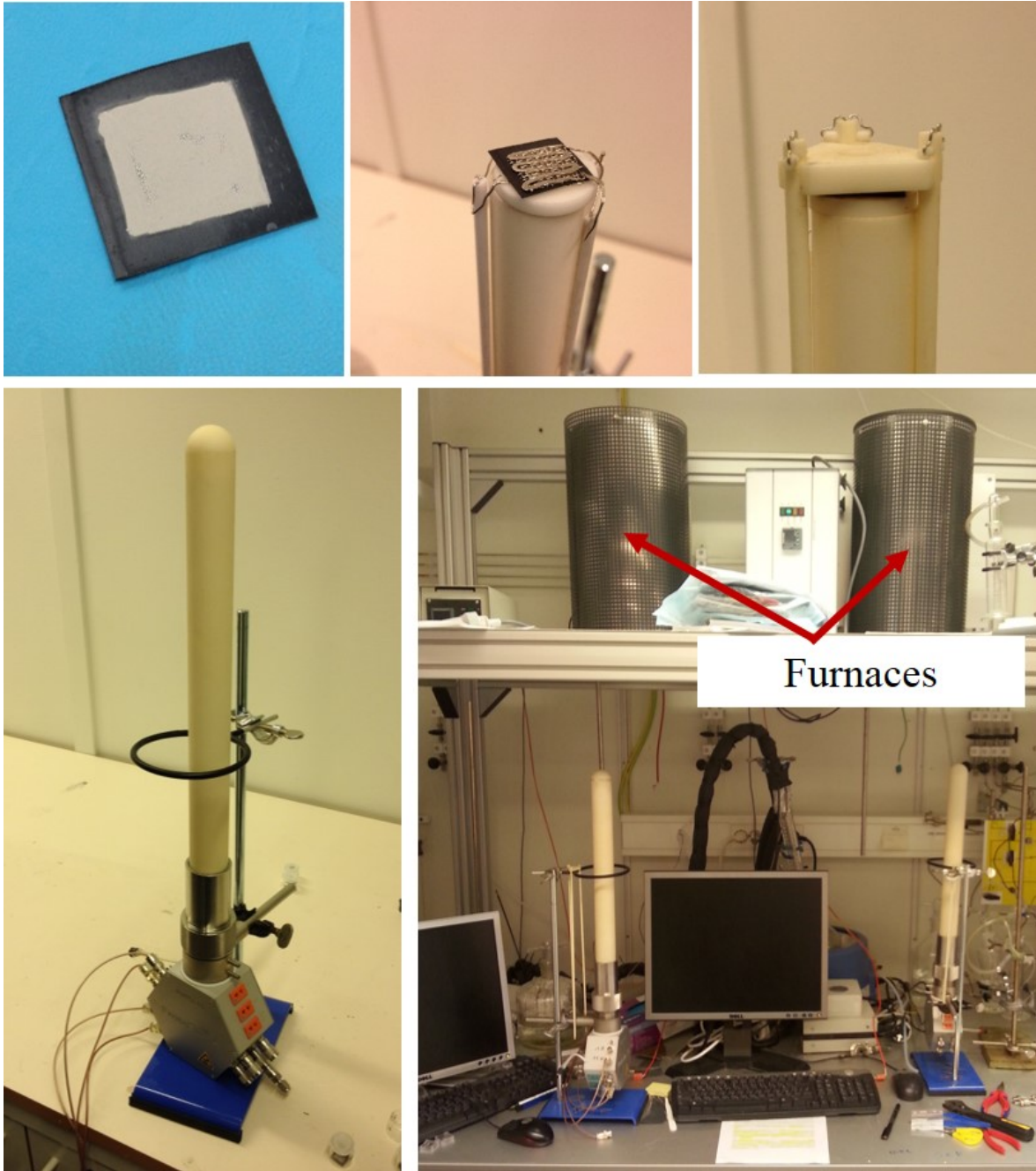
Figure 11: Images showing the ASR setup and how the sample is mounted.

4.5 Two-stage exposures/ ^{18}O tracer experiments

In order to study the growth mechanism of thermally grown oxide scales, a two-stage $^{18}O_2$ and $^{16}O_2$ experimental setup was used in Section 5.4 and in Paper VII. This special exposure setup was constructed at Chalmers University of Technology during the work of this thesis, and is shown in Figure 12 (a schematic drawing over the experimental setup can be seen in Paper VII (Figure 1)). By starting the exposure (stage 1) in an $^{18}O_2$-rich atmosphere, the thermally grown oxide scale formed during the first stage is marked by the oxygen isotope ^{18}O. Immediately before the second exposure stage, the atmosphere is switched (without cooling down the furnace) to a ^{16}O-rich atmosphere. The switch takes only a few minutes. After the samples have been exposed to both ^{18}O and ^{16}O, the thermally grown oxide scale is analysed using Secondary Ion Mass Spectroscopy (SIMS, see Section 4.6.6). By separating the two oxygen isotopes it is possible to see whether the ^{16}O-rich oxide, grown during the 2nd stage, is primarily formed by inward oxygen diffusion (metal-oxide interface is rich in ^{16}O), or by means of metal outward diffusion (gas-oxide interface is rich in ^{16}O). SIMS depth profiling has traditionally been used for this. The interpretation of such depth profiles are, however, often non-trivial due to the limited lateral resolution, which frequently is in the μm-range or in best cases a few hundred nanometers. Rough surface topography and thickness variation of the oxide scale over the analysed volume adds to the ambiguity of the results. For this reason a new method to analyse the two-stage exposures was developed in this thesis. Instead of traditional SIMS sputter depth profiling, high-resolution nanoSIMS was used to map (^{16}O and ^{18}O maps) the surface of a cross section prepared by FIB milling and lift-out technique. For more details regarding the exposure conditions and the SIMS analyses, see Paper VII.
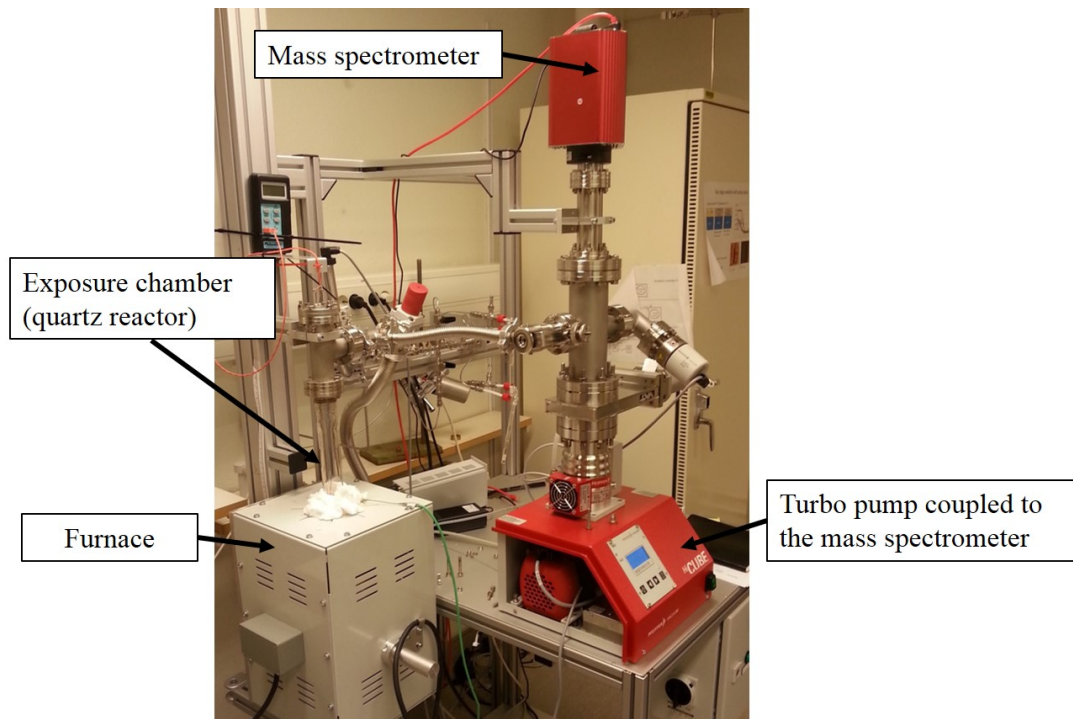

Figure 12: Photograph of the two-stage exposure setup (a schematic drawing of the experimental setup can be found in Paper VII, Figure 1).

4.6 Analytical techniques

In order to characterize the thermally grown oxide scales a combination of analytical methods has been utilized. Gravimetric measurements were made to follow the oxidation kinetics of the thermally grown oxide scales. Microstructure and chemical composition of the oxide scales were analysed by Scanning Electron Microscopy (SEM) and Energy Dispersive X-Ray analysis (EDX). In Papers III, V, and VII Focused Ion Beam (FIB) milling and lift-out technique was used to prepare thin lamellas for SEM/EDX and TEM analyses, and in papers III and IV Broad Ion Beam (BIB) milling was used to generate cross sections for SEM/EDX analyses. X-Ray Diffraction (XRD) was used to identify the crystalline phases present in the oxide scales. To measure the electrical resistance of the oxide scales, ASR measurements (see Section 4.4) were conducted at 650-850 °C (Papers II, III, and IV), and in paper VII Secondary Ion Mass Spectroscopy (SIMS) was utilized to analyse the oxide scale after the ^{16}O-, ^{18}O-isotope experiments. Furthermore, to quantify the amount of volatile chromium species, collected using the denuder technique, spectrophotometry was utilized (Papers I, III, V, and VI).

4.6.1 Scanning Electron Microscopy (SEM)

Scanning Electron Microscopy (SEM) is a frequently used tool for microstructural surface characterization. In contrast to optical light microscopy, SEM is not limited by the wavelength of optical light and can therefore reach much higher resolutions than optical microscopy [85]. A focused beam of electrons, called the primary beam, is created in the electron gun. When the electrons of the primary beam penetrate the sample surface, interaction between the electron beam and the solid specimen generates secondary electrons (SE), backscattered electrons (BSE) and characteristic X-rays (EDX) [85]. By scanning the sample surface, a virtual SEM image of the sample surface can be constructed.

Secondary Electrons (SE):
The electrons ejected from the sample surface as the primary beam penetrates the surface of the sample are called secondary electrons (see Figure 13). Secondary electrons tend to have very low energy and can therefore only escape from the outermost part of the sample (< 2 nm below the surface). For this reason, secondary electrons offer the best imaging resolution [85].
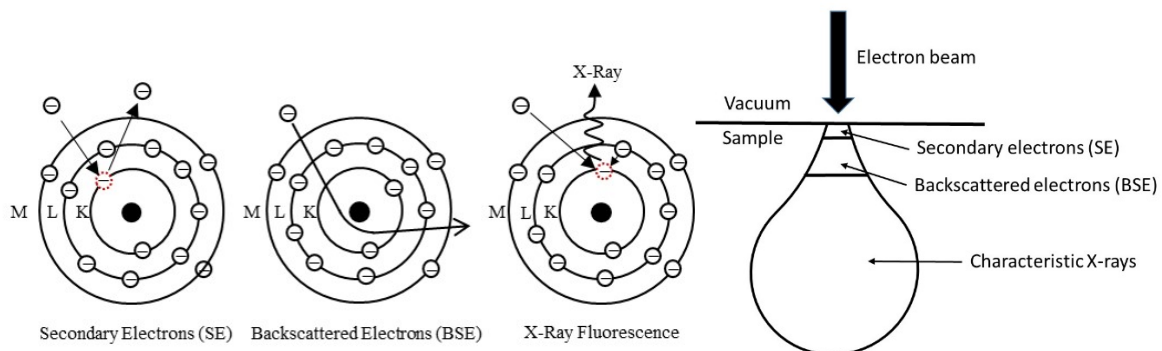

Figure 13 Schematic drawing of how secondary electrons, backscattered electrons and characteristic X-rays are formed in an SEM, as well as the interaction volume between the incoming electron beam and the specimen, adapted from [85, 86].

Backscattered Electrons (BSE):
As the primary beam penetrates the surface of the sample some of the electrons are scattered back from the sample surface by means of elastic collision with the nuclei of the atoms in the sample. Backscattered electrons possess much higher energy than secondary electrons, which results in a much larger interaction volume (Figure 13), and as a consequence the resolution in a BSE image is not as good as in a SE image [85]. However, more electrons are backscattered in materials with heavy elements, which has the effect that heavier elements are brighter in a BSE image. Thus a BSE image can give information about variations in the chemical composition of the sample surface [85].

Energy Dispersive X-Ray analysis (EDX):
X-Rays are generated when an electron with high energy (from the primary beam) ejects an inner shell (e.g. K-shell) electron from a sample atom. As a result, another electron with higher energy in an outer electron shell will fill the vacancy, and as a consequence energy in the form of an X-ray photon is released (Figure 13). The energy of this characteristic X-ray photon, depends on the atomic number Z of the atom, and on the quantum numbers of the energy levels involved in the electron transition. Each element has therefore defined energy differences between their electron shells. These X-rays, emitted from the sample material, can be measured with an X-ray spectrometer and a spectrum can thus be constructed by plotting the number of X-ray photons as a function of photon energy [85]. X-rays can escape from a much larger depth in the sample material than secondary and backscattered electrons (Figure 13). For this reason EDX resolution is substantially poorer than the resolution of both SE and BSE images, and as consequence, great care needs to be taken when interpreting the EDX data.

4.6.2 Transmission Electron Microscopy (TEM)
Transmission Electron Microscopy (TEM) is a valuable technique in order to acquire information about microstructure, chemical composition and crystal structure with very high spatial resolution. In contrast to SEM, electrons from the primary beam pass through the sample in TEM. The sample therefore needs to be electron transparent (usually 20-200 nm), and the accelerating voltage very high (typically 200-300 kV). If the investigated material is crystalline, the incoming electrons are diffracted by planes of atoms inside the material. It is therefore possible to form a transmission electron diffraction pattern from the electrons that have passed through the TEM lamella, and thus the crystalline structure of e.g. an oxide layer can be identified [85]. Another valuable method is Electron Energy-Loss Spectrometry (EELS). EELS is the analysis of the energy distribution of electrons that have been transmitted through the specimen (the TEM lamella). Some of the transmitted electrons have not lost any energy at all, however others may have suffered inelastic (usually electron-electron) collisions, and thus lost energy. The lost energy can be correlated to the valence state, the nearest-neighbour atomic structure, and the band gab etc. [87]. Furthermore, due to the extremely high spatial resolution in EELS, this technique can be used to detect elements within the grain boundaries of oxide scales, as has been shown by M. Sattari et al. [88].

Prior to the TEM analysis, an electron transparent specimen must be prepared, which is usually done by FIB milling and lift-out technique (Section 4.6.3).

4.6.3   Cross section preparation

In order to characterize a thermally grown oxide scale, a cross section of the sample is usually prepared, which is subsequently analysed in the SEM. In Papers I, II, and V cross sections were manually prepared (grinding and polishing), whereas in Papers III and IV cross sections were prepared by Broad Ion Beam (BIB) milling, which is similar to Focused Ion Beam (FIB) milling. In Papers III, V, and VII FIB milling was used to prepare thin lamellas for SEM/EDX and TEM analysis.

Broad Ion Beam (BIB) milling:
Preparation of cross sections by ion milling has several advantages compared to traditional methods like mechanical polishing, such as less mechanical damage on the cross section surface, cracks and voids are not filled with polished material, and ion milling does not leave abrasive artefacts on the surface. For BIB milling, argon ions are utilized to mill deep into the sample and thus create a smooth surface that can later be analysed in the SEM. In this work a Leica EM TIC 3X was used, which is equipped with three argon ion guns and can therefore, within only a few hours, create a cross section as broad as one millimetre. Before the milling process a low speed saw with a diamond blade was used to cut the sample in half to enable BIB cross sections from the centre of the sample and not from the edges.

Focused Ion Beam (FIB) milling:
In both Focused Ion Beam (FIB) and Broad Ion Beam (BIB) milling, ions are utilized to prepare smooth cross section surfaces. In FIB this is done by focusing a high current ion beam, most commonly gallium (Ga) ions, at the surface. The high energy of the ions will sputter away the sample material, and by moving the beam a cross section can be created in a selected area [85]. In contrast to BIB milling only a very small cross section (10-20 μm) is created by FIB. Nevertheless, when a certain area on the sample is of interest, FIB milling may be more advantageous than BIB milling. Furthermore, to prepare a thin lamella for TEM analysis, FIB milling and lift-out technique is frequently used. FIB milling and lift-out technique was used in Papers III, and V to prepare a thin specimen for EDX analysis. Due to the much thinner specimen, the interaction volume decreases significantly (see Figure 13) and much higher EDX resolution can be achieved. In order to acquire high resolution TEM images, and to prepare a cross section for nanoSIMS analysis, preparation of a thin lamella by FIB milling and lift-out technique was also carried out in Paper VII.

4.6.4   X-Ray Diffraction (XRD)

X-Ray Diffraction (XRD) is an analytical method frequently utilized to determine the phases present in a crystalline material. When a beam of monochromatic X-rays strikes a crystalline surface at angle θ, some of the X-rays are scattered by the atoms at the surface, whereas the rest of the beam penetrates through the first layer of atoms to the second layer of atoms. From these X-rays a portion will be scattered at the second layer, whereas the rest of the X-rays will penetrate deeper into the material. For the scattered X-rays to emerge as a single beam of reasonable intensity they must be in phase (constructive interference). For constructive interference to take place the path lengths of the interfering beams must differ by an integral number of wavelengths [89]. The Bragg equation (Equation 21) is a mathematical relation

between the angles at which constructive interference occurs and the distance between the lattice planes in a crystal.

$$n\lambda = 2d_{hkl} \sin\theta \qquad (21)$$

Where d_{hkl} is the interplanar spacing between the lattice planes, θ is the angle between the incident beam and the lattice planes, n is an integer and λ is the wavelength of the incident X-ray beam. By measuring the intensity of the scattered X-rays as a function of the diffraction angle 2θ (°), a diffraction pattern is observed. The angles at which diffraction occurs can be used to determinate the spacing of the various lattice planes, and therefore the crystal structure of the phase or phases within the analysed material [48].

XRD is mainly used for phase analyses of bulk materials. For this purpose the Bragg-Brentano setup is the most common setup in which both the X-ray source and the detector move around the sample, allowing the angle of incidence and the angle of reflection to be the same. However, for XRD characterization of thin films, the X-ray source should preferably be fixed at a low angle, otherwise the signal from the thin film will be too weak. Another setup, called the Grazing-Incidence setup, is therefore commonly used for thin film characterization. With this setup the X-ray source is fixed at a specific angle (commonly < 5 ° depending on the thickness of the film), and only the detector moves around the sample. Both of these two setups have been used in this work. In Paper I very thin oxide scales were formed on some of the investigated samples, therefore the Grazing-Incidence setup was used in Paper I, whereas the Bragg-Brentano setup was used for XRD analysis in Paper IV, since some of the samples investigated in Paper IV had formed several μm thick oxide scales.

4.6.5 Spectrophotometry

Spectrophotometry can be utilized to determine the concentration of light-absorbing ions or molecules in a solution. The basic principles of spectrophotometry are to allow monochromatic light to pass through a cuvette containing a solution of light-absorbing ions or molecules, and measure the intensity of transmitted light with a photometer. The absorbance can then be calculated using the Beer-Lambert Law (22):

$$A = log_{10}\frac{I_0}{I} \qquad (22)$$

Where A is the absorbance, I_0 is the intensity of the transmitted light for a given wavelength using the pure solvent, and I is the intensity of transmitted light through the solution [90]. For Cr vaporization measurements (Papers I, III, V, and VI), the denuder technique was used, in which volatile chromium (VI) species react with the Na_2CO_3-coated denuder tube, forming Na_2CrO_4 (see Section 4.3). Water solutions containing CrO_4^{2-} ions show a strong absorption peak at 370 nm, and for this reason monochromatic light at this wavelength was used for concentration measurements of the CrO_4^{2-} solutions. By measuring the absorbance of several well-known CrO_4^{2-} standard solutions, an absorption factor could be calculated and used for the concentration analyses.

4.6.6   Secondary Ion Mass Spectroscopy (SIMS)

Secondary Ion Mass Spectroscopy (SIMS) is a technique used to analyse the chemical composition of solid surfaces by sputtering the surface of the sample, and subsequently analysing the ejected ions with a mass spectrometer. The basic principle of SIMS is to focus an ion beam, onto the specimen surface, thus creating secondary ions in a sputtering process [91]. Most of these sputtered particles are neutral and cannot be analysed. However, a fraction of the sputtered particles, typically between 10^{-5} and 10^{-2} (this is strongly depending on the species and the composition of the target (matrix)), are ionised in the process of ejection. These ions are referred to as "secondary ions". It is these ions that are physically separated and counted in the mass spectrometer [92]. SIMS is a technique frequently used for analysing very small amounts of an element such as impurity elements (ppm to ppb concentrations) [92]. In this work (Section 5.4 and Paper VII), SIMS was utilized to separate the two oxygen isotopes, ^{16}O and ^{18}O, within the oxide scales formed after two-stage exposures (see section 4.5). A TOF-SIMS V (ION-TOF, GmbH, Münster, Germany) was used for depth profiling, whereas a Carmeca Nano-SIMS 50L, with high spatial resolution (down to 50 nm [92]) was used to map ^{16}O and ^{18}O of a TEM-lamella.

For the sputter depth profiles (TOF-SIMS) a dual beam setup was used. First Cesium ions (Cs^+) were used to remove, step by step, the oxide scale (create a sputter crater, and thus also a sputter depth profile). The secondary ions that were ejected from the specimen surface in this step were not analysed in the mass spectrometer. Instead, after each Cs^+ sputtering step, Bismuth ions (Bi^+ or Bi_3^+) were used to analyse the surface in the sputter crater. The secondary ions created in this second step were the ions subsequently analysed in the time-of-flight (TOF) mass spectrometer. The sputtering procedure in the nanoSIMS (for the ^{16}O and ^{18}O maps) is slightly different from that of the TOF-SIMS. In the nanoSIMS a continuous beam of Cs^+ is used for sputtering, and the ionized surface atoms (secondary ions) from this step are analysed in the mass spectrometer.

5. Results and discussion

5.1 Uncoated steel: Cr vaporization and oxide scale growth at 650-850 °C

Increased temperature is commonly used to accelerate high temperature corrosion mechanisms that are thermally activated, such as oxide scale growth and Cr vaporization. Cr vaporization and oxide scale growth are however two separate mechanisms, and may therefore be influenced differently by an increase in temperature. The purpose of this study was therefore to separately investigate the influence of temperature on both mechanisms. Two commercially available ferritic stainless steels, Sanergy HT and Crofer 22 H, were selected and isothermally exposed for 24, 168 and 500 h at three temperatures (650, 750 and 850 °C).

5.1.1 Net mass gain

At 850 °C both steels show parabolic mass gain behaviour (Figure 14). However, as the temperature is decreased, to 750 and 650 °C, negative mass gains are observed for both materials after 500 h.
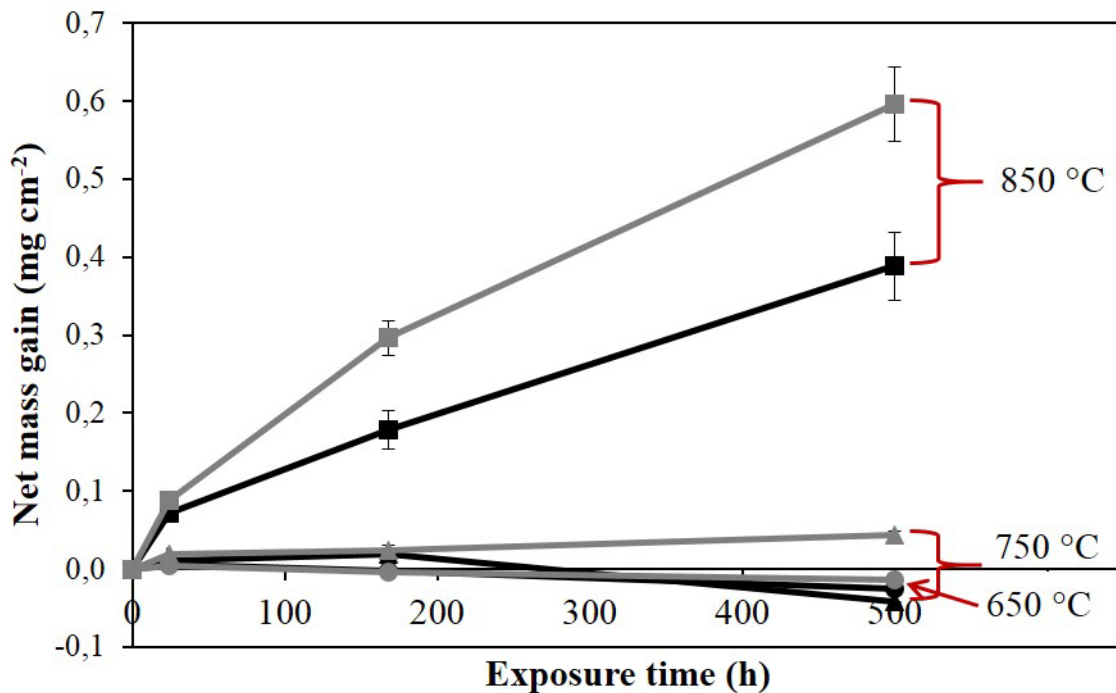
Figure 14: Net mass gain for Sanergy HT (black) and Crofer 22 H (grey) isothermally exposed for 24, 168 and 500 h at 650 (dots), 750 (triangles) and 850 °C (squares) in air containing 3% H_2O (6000 sml min^{-1}).

An increase in mass is commonly attributed to oxide scale growth. However, changes in net mass gain values may be misleading owing to factors such as vaporization or spallation of the oxide scale. Since no signs of oxide scale spallation were observed, the negative mass gain values seen at the lower exposure temperatures are believed to be an effect of Cr vaporization. This type of mass gain behaviour, seen at both 650 and 750 °C, is commonly associated with paralinear oxidation, where the mass gain value is a function of parabolic oxide scale growth with simultaneous vaporization of the oxide scale [53, 93].

5.1.2 Accumulated Cr vaporization

From the Cr vaporization measurements presented in Figure 15, it can be concluded that both steels exhibits similar vaporization behaviour. However, the amount of vaporized Cr at all three temperatures is on average 20-30% lower after 500 h of exposure for Crofer 22 H. Furthermore, the Cr vaporization measurements show that a substantial amount of Cr is vaporized even at lower temperatures (only a factor ~5 lower at 650 °C compared to at 850 °C after 500 h).
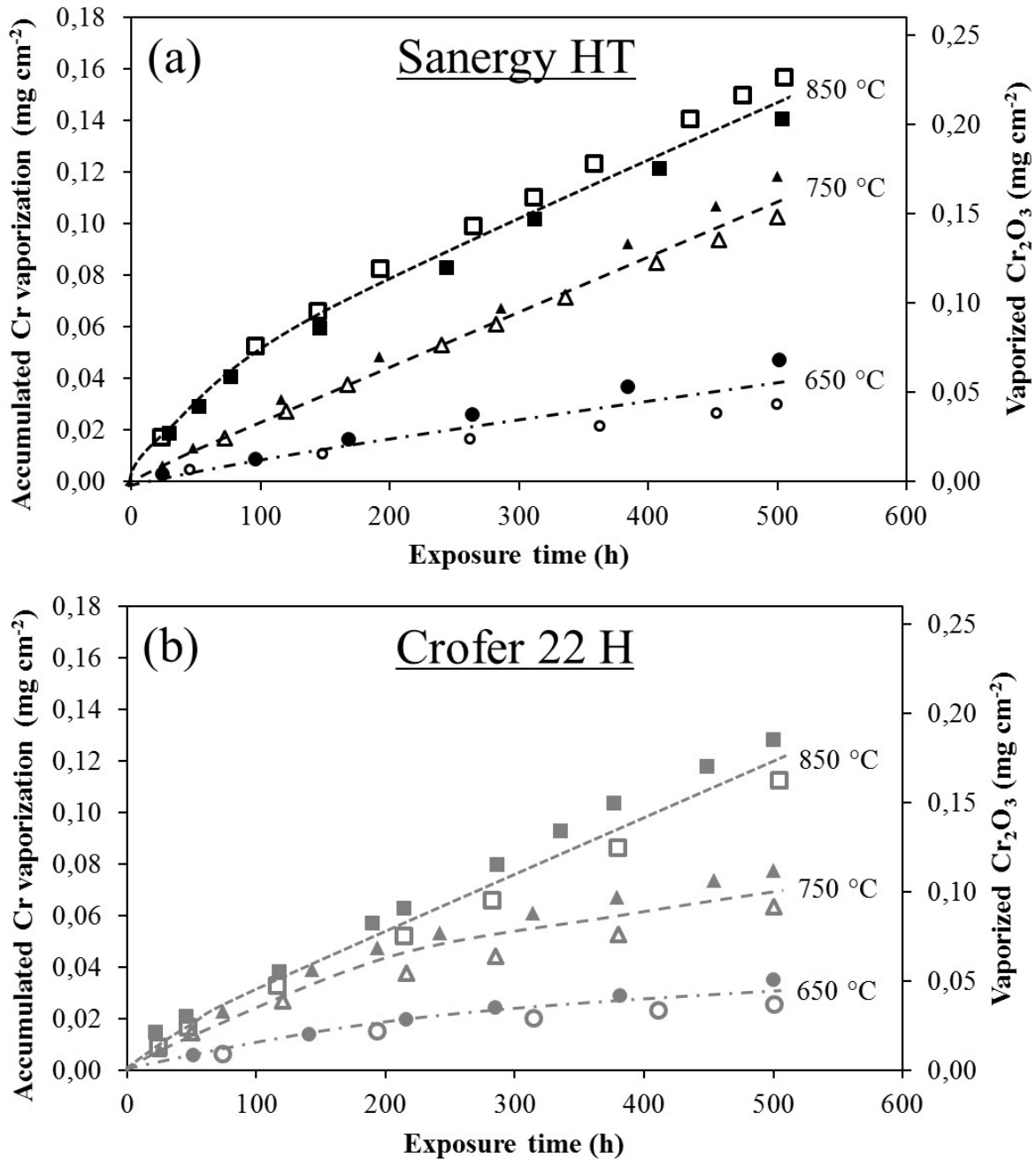

Figure 15: Accumulated Cr vaporization as a function of time for (a) Sanergy HT and (b) Crofer 22 H at 650 (dots), 750 (triangles) and 850 °C (squares) in air containing 3% H_2O (6000 sml min^{-1}). Filled and empty symbols represent the two individual isothermal exposures. The dashed lines are provided for illustrative purposes.

5.1.3 Gross mass gain

By adding the amount of vaporized Cr (as Cr_2O_3) to the net mass gain values in Figure 14, the gross mass gain (compensated for Cr vaporization) can be calculated. By compensating for the mass loss caused by Cr volatilization, it can be concluded that both steels show positive gross mass gain values at all three temperatures, as would be expected (Figure 16). Furthermore, both steels show parabolic gross mass gain behaviour at all three temperatures, which indicates that solid state ion diffusion is the rate-determining mechanism for oxide scale growth. It is also interesting to note that both steels show very similar gross mass gain behaviour at 750 ºC. This indicates that the lower net mass gain values for the steel Sanergy HT at 750 ºC (Figure 14) are an effect of the higher amount of vaporized Cr at this temperature. The lower mass gain values for Sanergy HT at 850 ºC cannot however entirely be explained by a higher amount of volatilized Cr. Instead, the main reason for the lower mass gain for Sanergy HT at 850 ºC is the thinner oxide scale (Figure 18). The thicker oxide scale for the Crofer 22 H material may be an effect of the higher Mn content compared to Sanergy HT. Hua et al. [94] and Stott et al. [95] have studied the effect of Mn in Fe-Cr steels, and in both studies it was seen that the oxide scale thickness increased as an effect of higher Mn content. Also Sachitanand et al. [66] observed an increase in mass gain as a function of Mn content in the steel, as he investigated five different ferritic stainless steels aimed to be used as interconnect material in SOFC. Nevertheless, there are other differences between Crofer 22 H and Sanergy HT, such as minor alloying elements, microstructure and surface treatment etc., which may very well have a larger effect on the oxidation kinetics than the Mn content.
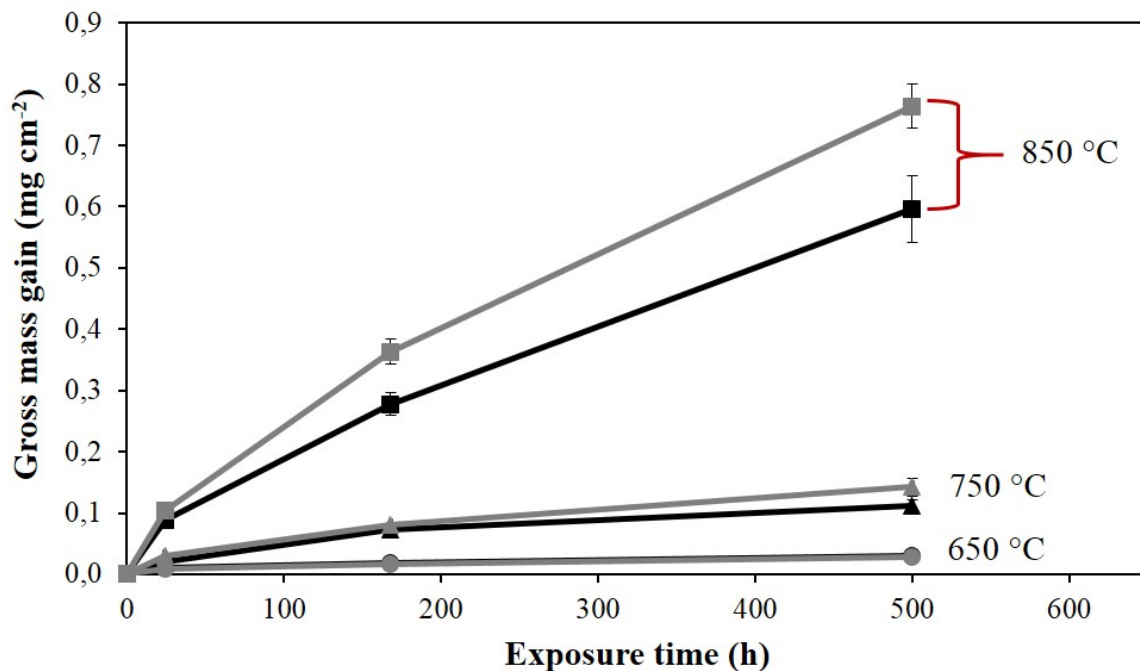

Figure 16: Gross (corrected for Cr vaporization) mass gain for Sanergy HT (black) and Crofer 22 H (grey) isothermally exposed for 24, 168 and 500 h at 650 (dots), 750 (triangles) and 850 °C (squares) in air containing 3% H_2O (6000 sml min^{-1}).

5.1.4 Cr vaporization rate

One of the main advantages with the denuder technique (see Section 4.3) when measuring Cr vaporization is that denuder tubes can be replaced during isothermal exposure without affecting the samples. The amount of Cr collected in each denuder interval can therefore be used to calculate the rate of Cr vaporization as a function of exposure time. In Figure 17 it can be seen that the Cr vaporization rate decreases initially for both materials at all three exposure temperatures, although at 650 °C, and for Sanergy HT at 750 °C, the initial decrease is not very pronounced. At 850 °C a faster decrease in Cr vaporization rate is seen for Crofer 22 H compared to Sanergy HT. Furthermore, at 750 °C a clear decrease in Cr vaporization rate is seen within the first 200 hours of exposure for Crofer 22 H, whereas for Sanergy HT only a very small initial decrease is observed. In fact, Cr vaporization measurements from uncoated Sanergy HT after more than 3000 h at 750 °C show that the rate of Cr vaporization is not decreasing any further than after 500 h at 750 °C (Figure 29 in Section 5.2.2). The faster and more pronounced decrease in Cr vaporization rate for Crofer 22 H compared to Sanergy HT could be correlated to the higher Mn content in Crofer 22 H compared to Sanergy HT (the Sanergy HT batch 531816 was used in this study). This element is critical in forming a $(Cr,Mn)_3O_4$ top-layer, which is known to reduce Cr vaporization [66, 70].
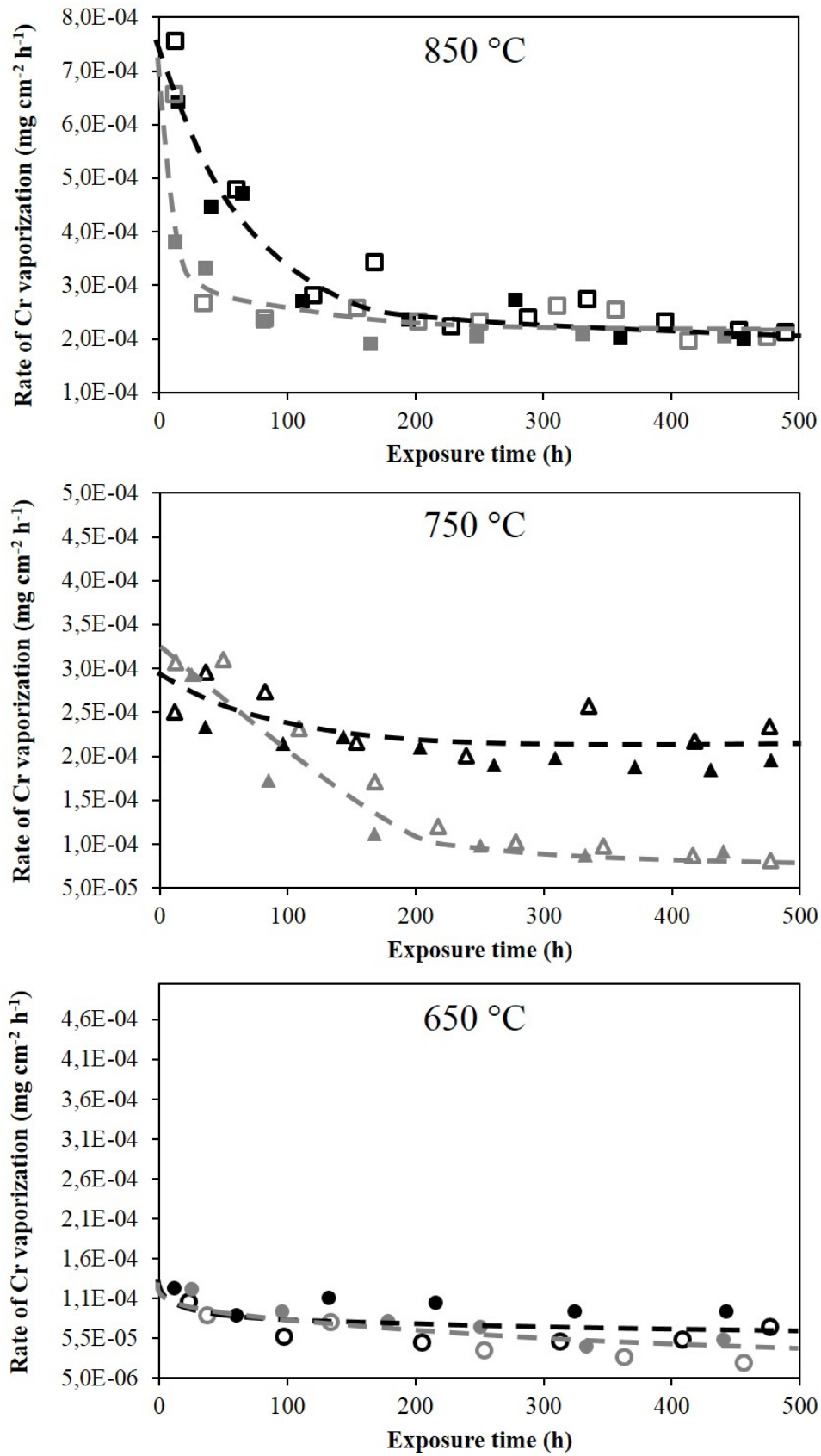
Figure 17: Rate of Cr vaporization as a function of time for Sanergy HT (Black) and Crofer 22 H (Grey) at 850, 750 and 650 °C in air containing 3% H_2O (6000 sml min^{-1}). Filled and open symbols represent the two individual isothermal exposures. The dashed lines are provided for illustrative purposes.

At 850 °C Mn outward diffusion is fast, which is assumed to be the reason for the strong reduction in Cr vaporization rate at this temperature compared to 750 and 650 °C. Already after 168 h at 850 °C a 1-1.5 μm thick $(Cr,Mn)_3O_4$ top-layer has been formed on Sanergy HT according to Froitzheim et al. [27]. The formation of a micrometre thick $(Cr,Mn)_3O_4$ top-layer could explain the rapid decrease in Cr vaporization rate observed during this time interval for Sanergy HT. The thickness of the $(Cr,Mn)_3O_4$ top-layer after 500 h in this study was also ~1 μm (see Figures 18 and 20), which would explain why the decrease in Cr vaporization rate levels off after 100-200 h for the Sanergy HT material. In Figure 15 it was shown that less Cr vaporized from Crofer 22 H compared to Sanergy HT after 500 h at 850 °C. However, the Cr vaporization rate measurements show that the difference in the total amount of volatilized Cr after 500 h at 850 °C is correlated to the faster reduction in Cr vaporization rate for the Crofer 22 H material (Figure 17). After 200 h of exposure at 850 ºC no measurable difference in Cr vaporization rate between the two materials can be observed. This is in good agreement with the SEM cross section images in Figure 18 that show that both materials have formed similar $(Cr,Mn)_3O_4$ top-layers after 500 h at 850 °C. Since Sanergy HT contains less Mn than Crofer 22 H it is assumed that the $(Cr,Mn)_3O_4$ top-layer is growing slower on Sanergy HT compared to Crofer 22 H, and thus a less steep decrease in Cr vaporization rate is observed for the Sanergy HT steel. Nevertheless, as was mentioned earlier, it is important to point out that other factors, such as steel microstructure and surface treatment, are also important factors that influence the outward flux of Mn ions, and thus the growth of a $(Cr,Mn)_3O_4$ top-layer.
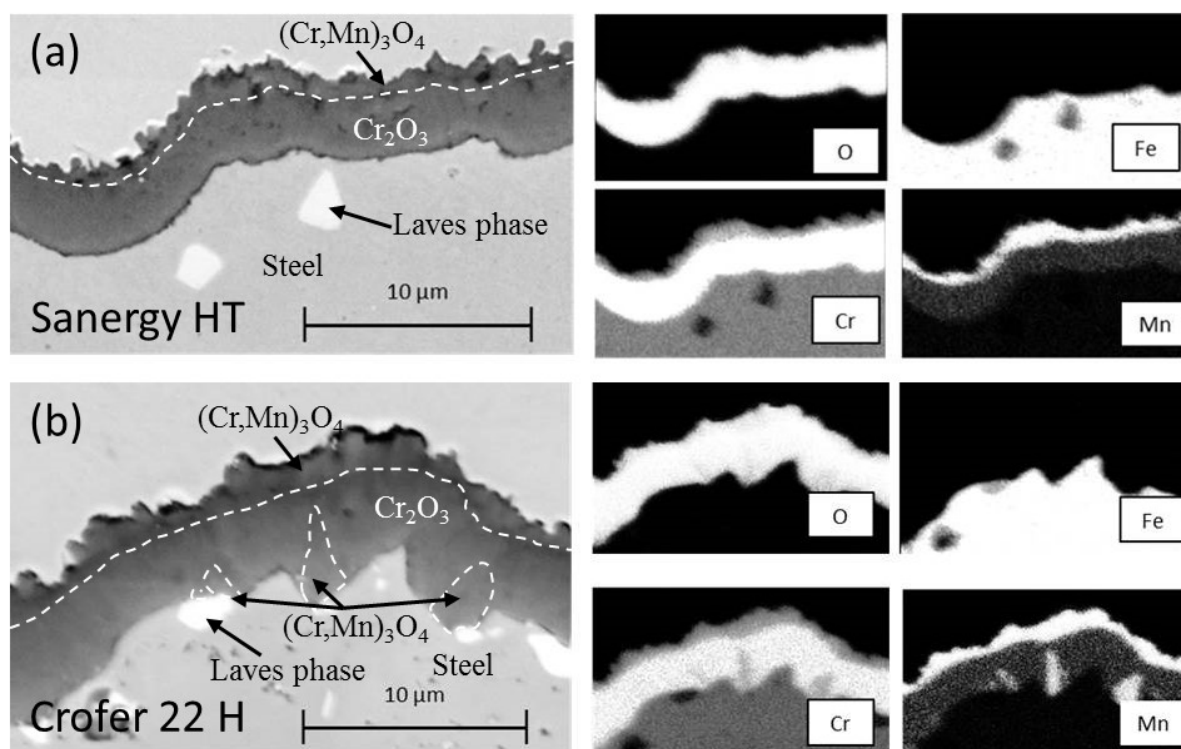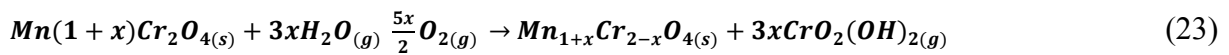

Figure 18: SEM cross section images and EDX elemental maps of (a) Sanergy HT and (b) Crofer 22 H exposed for 500 h at 850 °C in air 3% H_2O (6000 sml min⁻¹).

Moreover, in the previously discussed study by Froitzheim et al. [27], a thin top-layer oxide, rich in both Mn and Cr, was observed already after 1 h at 850 °C for Sanergy HT. This sample

was exposed under the same exposure conditions as the 850 °C samples in this work. If a continuous, or almost continuous, layer of $(Cr,Mn)_3O_4$ is already formed after 1 h of exposure, the strong decrease in Cr vaporization rate between 1-200 h of exposure seen in this work cannot completely be explained by the formation of a $(Cr,Mn)_3O_4$ layer. It is assumed that vaporization of Cr species takes place at the gas-oxide interface, and should therefore not be thickness-dependent if the chemical composition of the oxide scale is homogenous. However, since a growing oxide scale under the present conditions is not expected to be in equilibrium, a concentration gradient may be present within the oxide scale. Due to rapid Mn outward diffusion from the steel, and the loss of Cr as an effect of Cr vaporization (reaction 23), a chemical gradient may be present within the $(Cr,Mn)_3O_4$ top-layer.

$$Mn(1+x)Cr_2O_{4(s)} + 3xH_2O_{(g)} \frac{5x}{2}O_{2(g)} \rightarrow Mn_{1+x}Cr_{2-x}O_{4(s)} + 3xCrO_2(OH)_{2(g)} \qquad (23)$$

According to Jung [96], there is a miscibility in $(Cr,Mn)_3O_4$ at elevated temperatures at which the Cr:Mn ratio can vary from 2:1 $(MnCr_2O_4)$ to 1:2 (Mn_2CrO_4). In order to investigate whether a chemical gradient can be seen within the $(Cr,Mn)_3O_4$ top-layer, two TEM lamellas were prepared from the samples exposed for 24 and 500 h at 850 ˚C, and EDX line scans were carried out (Figures 19 and 20).

Figure 19: STEM/EDX line scans along the $(Cr,Mn)_3O_4$ top-layer formed on Sanergy HT after 24 h at 850 ˚C in air containing 3% H_2O with a flow rate set to 6000 sml min^{-1}.

In the 24 h sample the observed Cr:Mn ratio was 2:1 throughout the entire $(Cr,Mn)_3O_4$ top-layer. For the sample exposed for 500 h (Figure 20) a 2:1 Cr:Mn ratio was observed at the

metal-oxide interface (as was the case for the 24 h sample). However, in contrast to the 24 h sample, the Cr concentration decreased towards the surface, resulting in a Cr:Mn ratio of 1:1 at the gas-oxide interface. It should however be pointed out that the EDX line scan in Figure 20 doesn't represent the entire $(Cr,Mn)_3O_4$ top-layer formed after 500 h at 850 ˚C. In the areas next to the large crystal, where the $(Cr,Mn)_3O_4$ top-layer is thinner, the Cr:Mn ratio was 2:1 throughout the entire spinel top-layer. Nevertheless, due to the greater diffusion distance out to the outermost part of the surface in the larger crystals, in combination with a larger surface area where Cr volatilization can take place, the Cr:Mn ratio is shifted towards a lower Cr concentration at the surface of the larger spinel crystals. From these results it is not possible to conclude whether the observed chemical gradient in the larger surface crystals actually could be the main cause for the rapid decrease in Cr vaporization rate seen in Figure 17. Furthermore, during exposure, not only is the chemical composition at the surface changing, the actual surface area and the amount of grain boundaries (rapid diffusion paths for Cr and Mn) are also changing with time, due to coarsening of the spinel top-layer crystals. It should also be pointed out that, although the resolution of EDX line scans on thin lamellas are very good, the exact Cr:Mn ratio at the outermost monolayers is not known, which is the area where the formation of volatile chromium (VI) species are assumed to take place. Nevertheless, what the results did show is that as large spinel crystals are growing at the surface, Cr supply to the outermost part of the surface is reduced, and as a consequence, the Cr concentration is decreasing, thus reducing the Cr concentration at the surface.
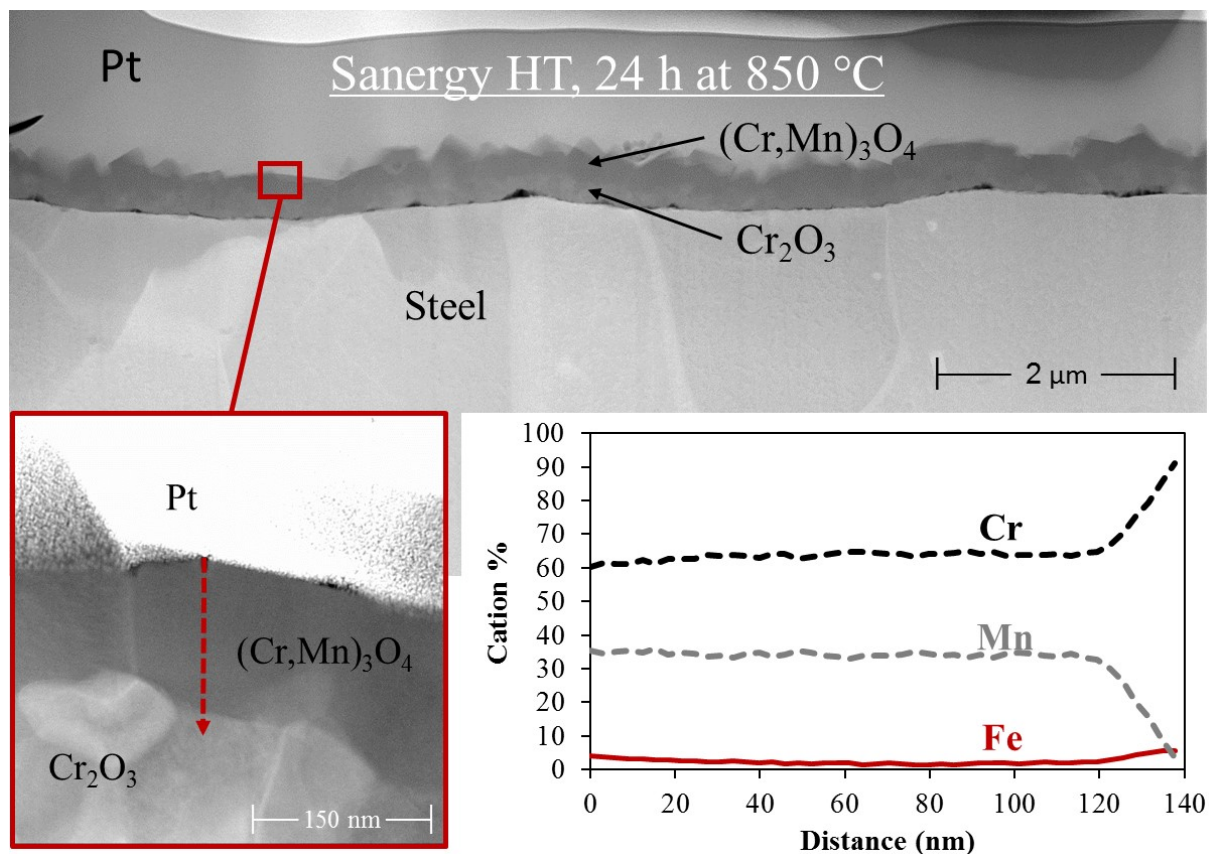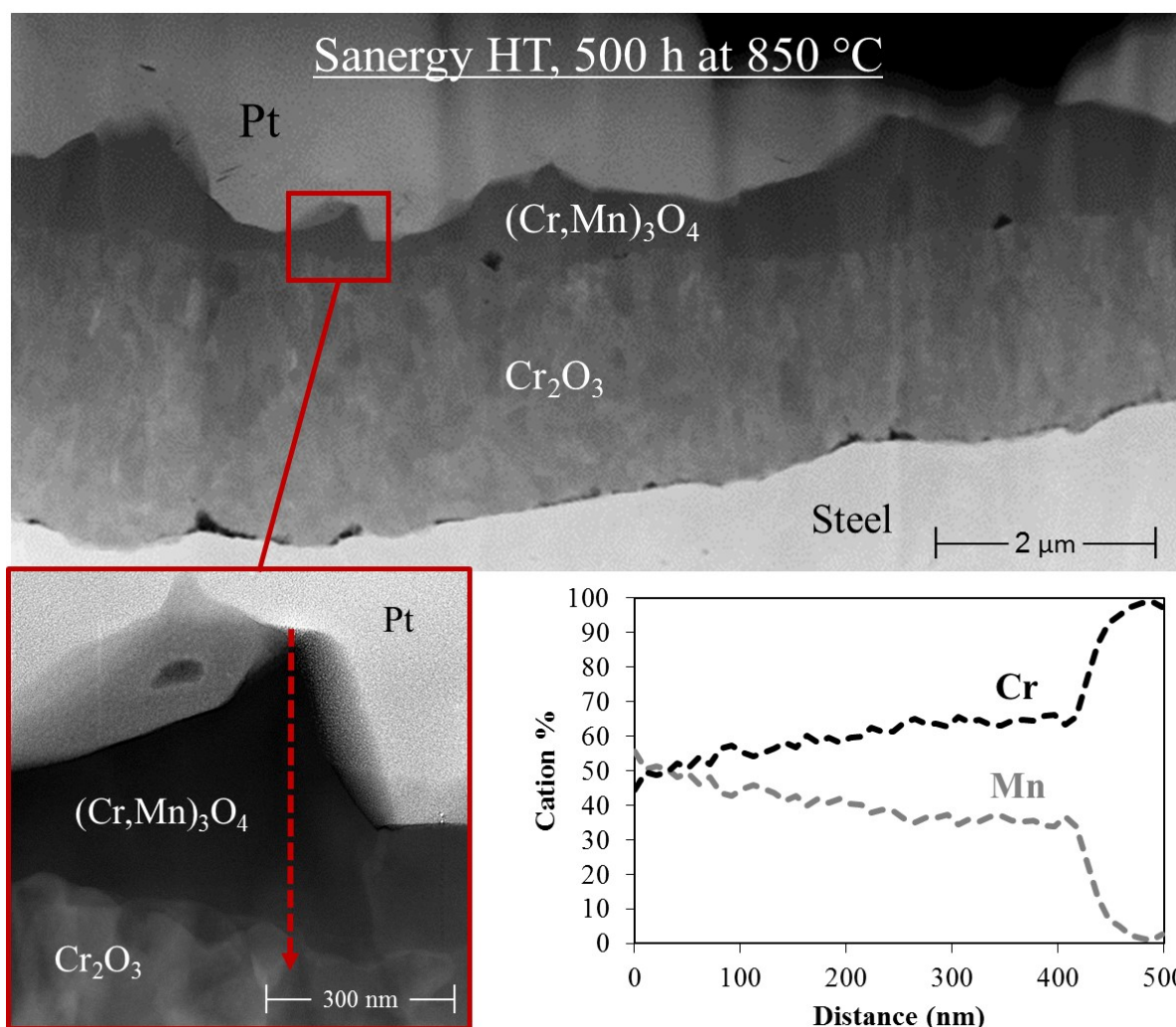
Figure 20: STEM/EDX line scans along the $(Cr,Mn)_3O_4$ top-layer formed on Sanergy HT after 500 h at 850 °C in air containing 3% H_2O with a flow rate set to 6000 sml min^{-1}.

When the temperature is reduced from 850 °C to 750 °C the reduction in Cr vaporization rate is slower and less pronounced. This is assumed to be correlated to slower outward diffusion of Mn ions at the lower temperature. Moreover, at 750 °C a notable difference was observed between the two steels (Figure 17). Crofer 22 H showed a reduction in Cr vaporization rate during the first 200-300 hours of exposure, whereas Sanergy HT only showed a small reduction initially. In fact, after 200-300 h the Cr vaporisation rate at 750 °C for Crofer 22 H was only half of the rate for Sanergy HT. According to the XRD analysis, Cr_2O_3 and spinel-type oxide were formed on both steels at 750 °C (see Paper I). From the top-view images in Figure 21 it can be seen that the surface crystallites are larger at the surface of Crofer 22 H compared to Sanergy HT. Based on the observations in Figures 19 and 20, it can be speculated that the concentration of Cr at the surface of the Crofer 22 H steel is lower than the Cr concentration at the surface of the Sanergy HT steel, resulting in a lower Cr vaporization rate for the Crofer 22 H steel.

41
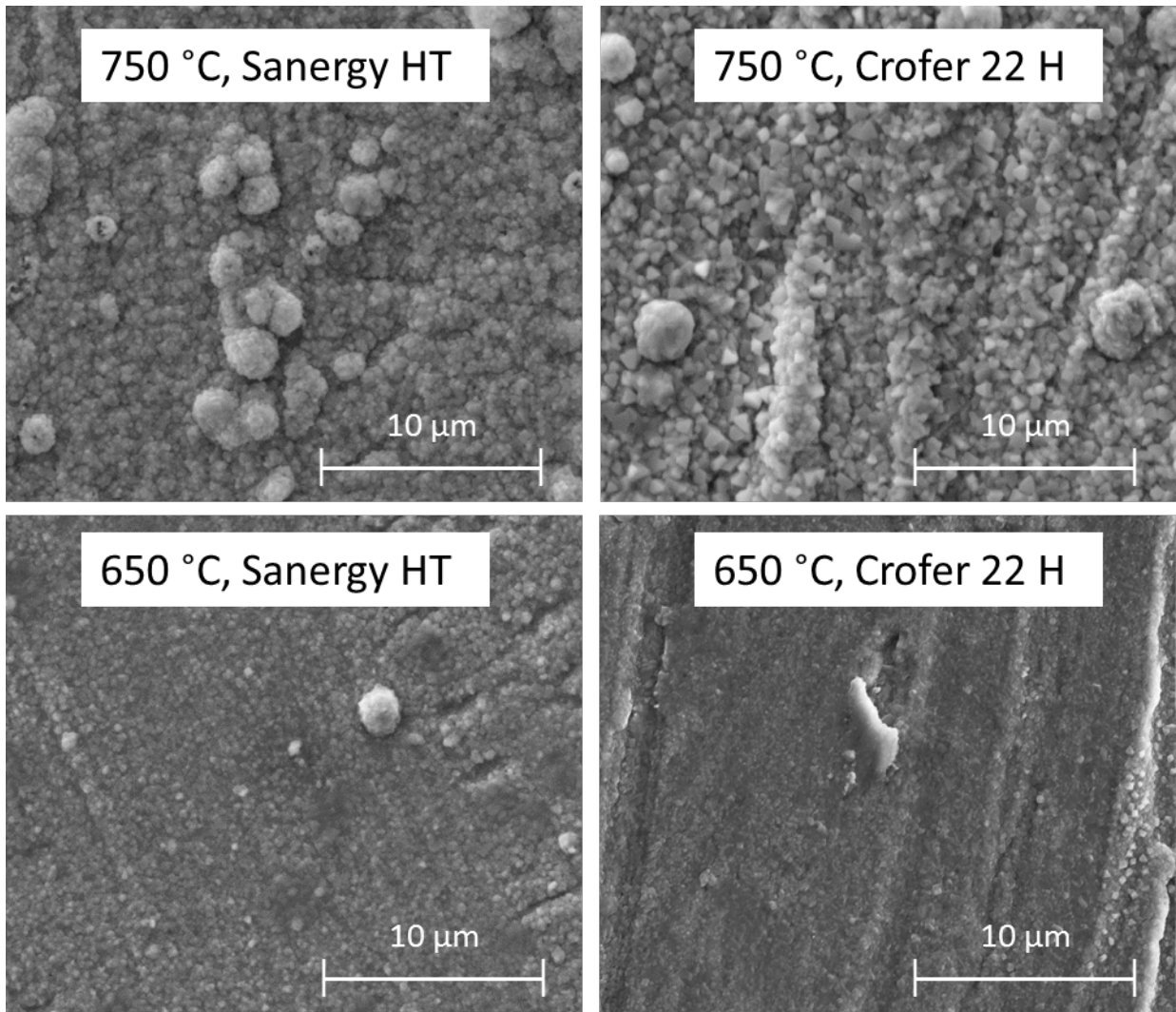
Figure 21: SEM top view images of Sanergy HT and Crofer 22 H exposed for 500 h at 750 and 650 °C in air containing 3% H_2O with a flow rate set to 6000 sml min^{-1}.

When the exposure temperature is decreased even further, down to 650 °C, both steels shows similar vaporization rates (Figure 17), and only a very limited reduction in Cr vaporization rate with time can be noticed. This agrees well with the top-view images in Figure 21, where no clear difference in crystallite size between the two steels can be seen. According to the XRD analysis (see Paper I) the two phases, Cr_2O_3 and spinel-type oxide, were also formed on both steels at 650 °C.

5.1.5 The effect of temperature on oxide scale growth and Cr vaporization

To be able to compare the effect of temperature on the two degradation mechanisms, oxide scale growth and Cr vaporization, the activation energy for both reactions was calculated using Equation 24.

$$\ln(k) = \frac{-E_a}{RT} + \ln(A) \qquad (24)$$

Where k is the rate constant of a chemical reaction (oxide scale growth respectively Cr vaporization), E_a is the activation energy, R is the universal gas constant, T is the absolute temperature and A is the pre-exponential factor.

To calculate the activation energy for oxide scale growth, parabolic rate constants were calculated from the gross mass gain data (Figure 16). The relationship between mass gain and oxidation kinetics can be described using the parabolic rate law (25).

$$\Delta m^2 = k_p t + A \qquad (25)$$

Where Δm is the mass gain, t is the exposure time, A is the integration constant and k_p is the parabolic rate constant. Both steels showed parabolic type behaviour, which indicates that scale growth is controlled by solid state diffusion. The calculated rate constant values at 650, 750 and 850 °C (see paper I) are within the typical order of Cr_2O_3-forming materials [97-99]. From these values, activation energies of 261 and 283 kJ mol^{-1} for Sanergy HT and Crofer 22 H, respectively, were obtained.

These values agree well with other published activation energy values for the high temperature oxidation of Fe-Cr alloys in air [97, 100-102]. Activation energy values obtained from such parabolic rate constants are probably a combination of several mechanisms and specific for the alloys and exposure conditions. Nevertheless, the values are close to the 255 kJ mol^{-1} reported by Hagel and Seybolt [103] for cation diffusion in Cr_2O_3, which might therefore suggest that the oxide scale predominantly grows by means of the outward diffusion of Cr ions.

To calculate the activation energy for Cr vaporization, non-isothermal exposures were carried out (Figure 22), since the isothermal exposures did not show Arrhenius-type temperature dependence. The non-Arrhenius-type temperature dependence for the isothermal exposures is assumed to be due to differences in morphology and/or chemical composition of the spinel top-layer at various temperatures.
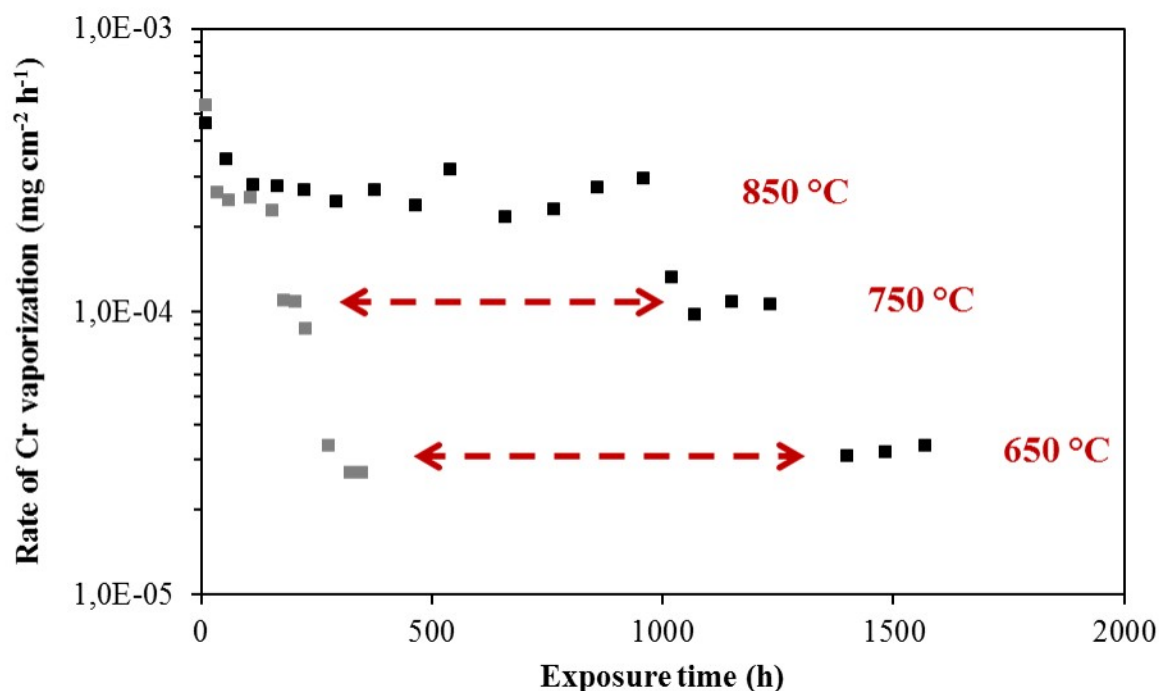
Figure 22: Rate of Cr vaporization for Sanergy HT (Black) and Crofer 22 H (Grey) at different temperatures in air containing 3% H_2O (6000 sml min^{-1}). The samples were initially exposed at 850 °C until a steady-state rate was reached. Cr vaporization was then measured at 750 and 650 °C within the same exposure.

Using the rate of Cr vaporization obtained in these experiments, activation energies of 91 and 92 kJ mol^{-1} for Sanergy HT and Crofer 22 H, respectively, were obtained (see Arrhenius plot in Paper I, Figure 12). Since the activation energy for scale growth was approximately 3 times higher (~270 kJ mol^{-1}) than the activation energy for Cr vaporization (~90 kJ mol^{-1}), it can be concluded that Cr vaporization is less influenced by temperature than oxide scale growth. The lower activation energy value for Cr vaporization, compared to oxide scale growth, explains the negative net mass gain values for the uncoated materials at 750 and 650 °C (Figure 14).

5.1.6 Activation energy measurements for Cr vaporization from pure Cr$_2$O$_3$

Cr vaporization measurements from pure Cr$_2$O$_3$ were carried out in order to compare the activation energy value from pure Cr$_2$O$_3$ with the obtained activation energies for Cr vaporization from uncoated Sanergy HT and Crofer 22 H in the previous section, as well as the obtained values from Co- and Ce/Co-coated Sanergy HT in section 5.2.2. As is expected, the Cr vaporization rate is higher for pure Cr$_2$O$_3$ compared to uncoated Sanergy HT and Crofer 22 H (compare Figures 22 and 23). The lower Cr vaporization rate for the steels are associated with the formation of a (Cr,Mn)$_3$O$_4$ top-layer, lowering the activity of Cr at the surface. However, due to differences in microstructure and surface roughness between the thermally grown oxide scales and the dense Cr$_2$O$_3$ sample, a direct comparison between the rate values should be made with great care. Nevertheless, by calculating the activation energy value for Cr vaporization from the measurements on the pure Cr$_2$O$_3$ sample, a value of 85 kJ mol^{-1} was obtained. This value is very close (within the error of the measurement) to the value theoretically calculated by Panas et al. (83 kJ mol^{-1}) [104]. Furthermore, it is also close to the

values obtained from the two uncoated steels Sanergy HT and Crofer 22 H (~90 kJ mol^{-1}) in the previous section, and also from Co- and Ce/Co-coated Sanergy HT (~100 kJ mol^{-1}), shown in section 5.2.2. It might therefore be speculated that the vaporization mechanism is the same, irrespective if Cr is volatilized from pure Cr_2O_3, uncoated steels that are forming a $(Cr,Mn)_3O_4$ top-layer, or Co- and Ce/Co-coated steels forming a Co-spinel top-layer.

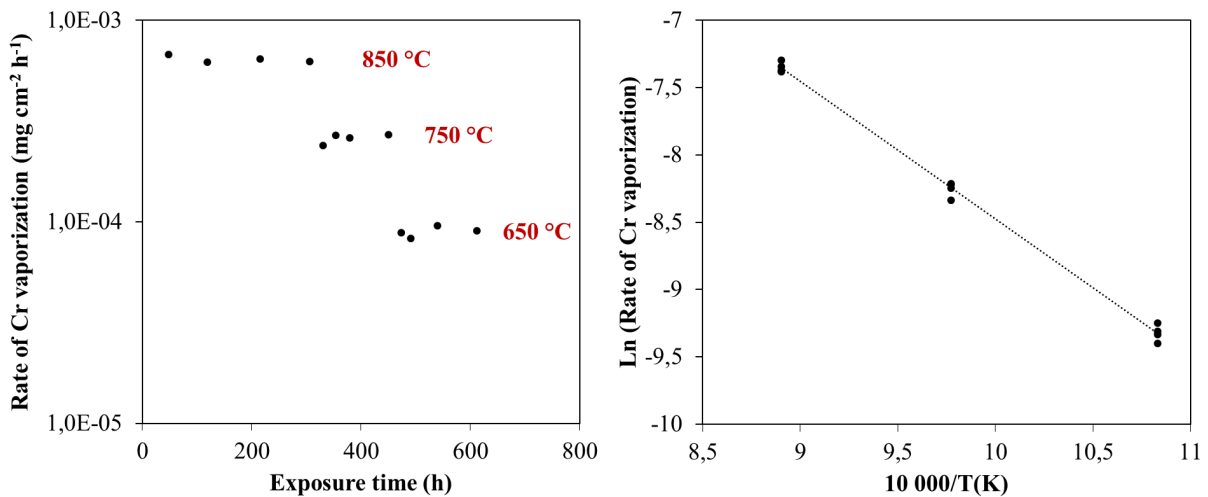**Figure 23:** Left graph: rate of Cr vaporization from the pure Cr_2O_3 sample at 850, 750, and 650 °C in air containing 3% H_2O (6000 sml min^{-1}). Right graph: The Cr vaporization rate values from the left graph displayed in an Arrhenius plot.

5.2   Thin-Film Co- and Ce/Co-coatings at 650-850 °C

In order to mitigate Cr vaporization, ferritic stainless steels can be coated with thin metallic Co-coatings (coatings to reduce Cr vaporization were discussed in Section 3.2). Thin metallic Co-coatings have been shown to mitigate Cr vaporization for more than 3000 h at 850 °C [27]. As the Co-coated steel is heated in air, Co is rapidly oxidized into a dual layered Co-oxide consisting of a Co_3O_4 top-layer and a layer of $(Co,Fe)_3O_4$ underneath [27]. With time these two layers are homogenised at 850 °C [26, 27]. Furthermore, due to outward diffusion of Mn from the steel, the Co-oxide will be enriched in Mn and thus converted into a layer of $(Co,Fe,Mn)_3O_4$ at 850 °C [26, 27]. If the steel is coated first with a 10 nm layer of Ce, and subsequently with Co, the formation of a $(Co,Fe)_3O_4$ layer is prevented [26, 32]. As a consequence, the Co-coating is only oxidized into a layer of Co_3O_4 initially. As for the exclusively Co-coated material, the Co-oxide on the Ce/Co-coated material is enriched with Mn with prolonged exposure time at 850 °C, and thus transformed into a $(Co,Mn)_3O_4$ top-layer [26, 32]. The reason for addition of the Ce-coating is not to prevent the formation of the $(Co,Fe)_3O_4$ layer. Ce is added in order to improve the oxidation resistance of the interconnect material. The possibility to improve the oxidation resistance by adding a 10 nm layer of the reactive element Ce between the steel and the Co-coating has been shown in earlier works at 850 °C [26, 105] (see section 3.3).

5.2.1 The effect of Co- and Ce/Co-coatings on the electrical resistance at 850 °C

The two main reasons to improve the oxidation resistance of the interconnect material are (1) to avoid breakaway corrosion, or spallation due to a thick oxide scale, and (2) decrease the electrical scale resistance caused by a growing Cr_2O_3 scale. To prove that the improved oxidation resistance due to the Ce-coating also reduces the electrical resistance of the growing

oxide scale, Area Specific Resistance (ASR) measurements were carried out on uncoated, 640 nm Co-coated, and 10 nm Ce + 640 nm Co coated Sanergy HT samples exposed for 1000, 2000, and 3000 h in air at 850 °C. The mass gain values (see Paper II) confirmed that the addition of a thin layer of Ce significantly improves the oxidation resistance. From the SEM cross section images in Figure 24, it can be seen that the improved oxidation resistance is correlated with the significantly thinner Cr_2O_3 scales formed on the Ce/Co-coated material compared to the exclusively Co-coated material. Moreover, by only coating the steel with Co no noticeable decrease in Cr_2O_3 scale thickness could be observed, since both uncoated and Co-coated Sanergy HT had formed comparable Cr_2O_3 scales after 1000, 2000, and 3000 h.

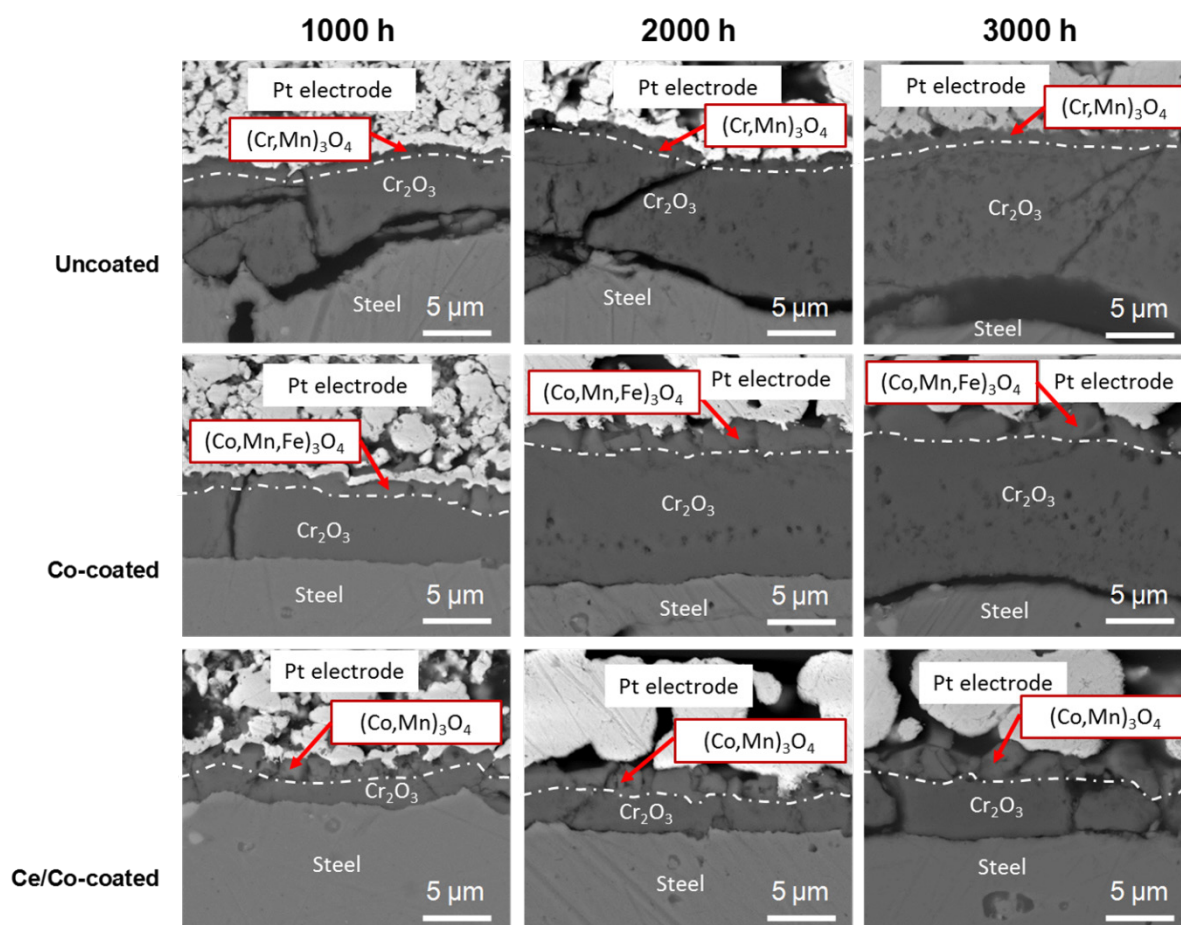**Figure 24:** SEM (Backscattered) cross section images of the Sanergy HT samples exposed for 1000, 2000, and 3000 h at 850 °C, used for ASR measurements in Figure 25.

The ASR measurements in Figure 25 prove that the additional layer of 10 nm Ce not only decreases the oxidation rate, but that this decrease in oxidation rate also leads to a lower ASR. Even after 3000 h at 850 °C the ASR for the Ce/Co-coated material is low.
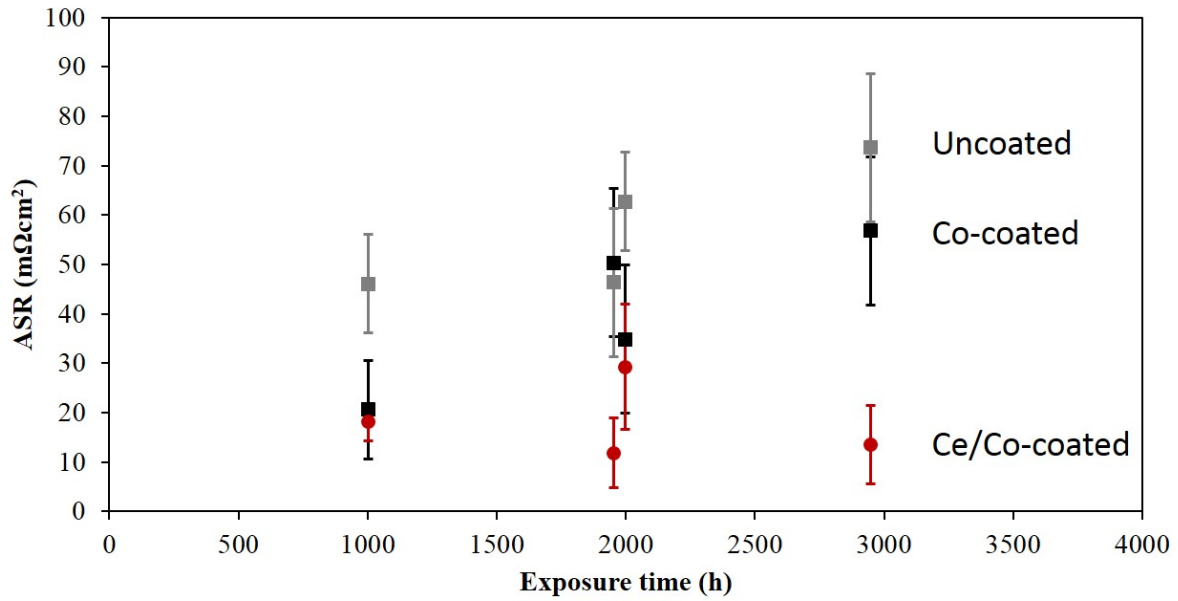
Figure 25: ASR values of pre-exposed samples at 850 °C in air. Uncoated (grey squares), Co-coated (black squares) and Ce/Co-coated (red dots). The error bars refer to the fluctuation of the ASR during the measurement.

What is interesting to note is that the ASR for the Ce/Co-coated material is 3.5 times lower than the ASR for the exclusively Co-coated material after 3000 h of exposure, whereas the difference in Cr_2O_3 scale thickness is only a factor of 2-2.5. Both materials form very conductive Co-spinel top-layers; $(Co,Mn,Fe)_3O_4$ and $(Co,Mn)_3O_4$ for the Co- and the Ce/Co-coated materials, respectively. These spinel layers are not contributing to the ASR according to the results in section 5.2.2. The main reason for the lower ASR for the Ce/Co-coated material is therefore assumed to be due to the thinner Cr_2O_3 scale. Furthermore, Grolig et al. [105] conducted a similar long-term ASR study at 850 °C on Co- and Ce/Co-coated Sanergy HT. In that study the ASR was measured in another, but similar, setup. Similar ASR values were measured and the same observation could be made; that the difference in ASR is larger than the difference in Cr_2O_3 scale thickness, when comparing the Ce/Co-coated with the exclusively Co-coated material. It can therefore be speculated that the Cr_2O_3 scale formed on the Ce/Co-coated material is more conductive than the Cr_2O_3 scale formed on the exclusively Co-coated material. In fact, Nagai et al. [60] showed that small amounts (up to 0.5% wt.) of the two reactive element oxides La_2O_3 and Y_2O_3 increased the electrical conductivity of Cr_2O_3, especially in the lower temperature regime (500-1000 °C). More detailed knowledge regarding the thermally grown Cr_2O_3 scales in combination with further ASR measurements would, however, be necessary in order to draw conclusions regarding possible differences in Cr_2O_3 scale conductivity.

Moreover, by comparing the ASR for the exclusively Co-coated material to the ASR for the uncoated material, it can be seen that the increase in ASR with exposure time is almost identical for both materials. Since both materials had formed equally thick Cr_2O_3 scales after 1000, 2000, and 3000 h, this observation agrees well with the assumption that the Cr_2O_3 scale thickness is the dominant factor for the ASR. Moreover, since the increase in ASR as a function of Cr_2O_3 scale thickness is similar for the uncoated and the Co-coated materials, it can be assumed that

these Cr_2O_3 scales have the same electrical conductivity, in contrast to the earlier speculations regarding the Ce/Co-coated and the exclusively Co-coated material. The only difference between the uncoated and the Co-coated material is that the ASR is approximately 20 mΩcm^2 higher for the uncoated material, at all three exposure durations. Since no clear difference in Cr_2O_3 scale thickness can be seen, it can be speculated that this extra 20 mΩcm^2 is correlated with the moderately conductive $(Cr,Mn)_3O_4$ top-layer [16, 106, 107], formed at the surface on the uncoated material. In fact, this layer is formed within the first 1000 h and is not expected to grow thicker with prolonged exposure time [27, 66]. This would explain why the ASR is constantly 20mΩ cm^2 higher at all three exposure durations. The results from this study show that comparing only Cr_2O_3 scale thicknesses can be misleading, and for this reason it is crucial to complement the oxidation studies with actual ASR measurements, especially when different materials are compared with each other.

5.2.2 Co- and Ce/Co-coatings for Intermediate Temperature SOFCs (650 and 750 °C)
Due to the weak temperature dependency for Cr vaporization, even a 200 °C decrease in operating temperature will only reduce Cr vaporization by a factor of ~5 for the uncoated steel (Figure 15). Coatings that mitigate Cr vaporization are therefore necessary to ensure stable, long-term performance in a SOFC stack, even if the operating temperature is decreased to temperatures as low as 650 °C. As was discussed in 5.2, earlier studies have shown that thin metallic Co-coatings are able to mitigate Cr vaporization at 850 °C for more than 3000 h [27], and if the additional Ce-layer is present (Ce/Co-coatings), reduced oxide scale growth and substantially lower ASR is observed (see section 5.2.1 and [26, 81, 105]). However, when thin metallic Co- and Ce/Co-conversion coatings are utilized it is assumed that these coatings transform into a highly conductive $(Co,Mn)_3O_4$-layer during exposure, due to outward diffusion of Mn from the steel, which was observed in all the previously cited studies. These studies were, however, carried out at 850 °C and as the temperature is reduced the kinetics are slower and, as a consequence, a change in microstructure and chemical composition is expected. In fact, the Cr vaporization rate for the uncoated material (section 5.1) did not show Arrhenius-type temperature dependence for the isothermally exposed samples. This was correlated to a change in surface microstructure and possibly also a change in chemical composition of the surface oxide as the temperature was reduced. The aim of this work was therefore to investigate metallic 640 nm Co and 10 nm Ce + 640 nm Co coated Sanergy HT at 650 and 750 °C with regard to Cr vaporization, oxide scale growth, microstructural and chemical evolution, and the effect these factors have on the electrical resistance of the oxide scale.

The effect of decreased temperature on the Co-spinel layer:

Co-coatings:
As the metallic Co-coating is heated in air to 650-850 °C the metallic Co-coating is rapidly converted into Co-spinel. For the steels coated exclusively with Co, the Co-coating is oxidized into a dual-layered Co-oxide consisting of an almost pure Co_3O_4 top-layer and a Fe-rich

(Co,Fe)$_3$O$_4$ layer underneath (Figures 26 and 27). The mechanism behind the formation of such a dual-layered Co-oxide for the exclusively Co-coated material is discussed in more detail in Paper IV. The formation of a dual-layered Co-spinel, consisting of the two layers Co$_3$O$_4$ and (Co,Fe)$_3$O$_4$, takes place during the initial oxidation phase i.e. as the metallic Co-coating is converted into Co-oxide, and is observed at 650, 750, and 850 °C. However, within 3300 h at 750 °C (Figure 27), and already within 168 h at 850 °C [27], Fe will be homogenously distributed throughout the Co-spinel. In contrast, at 650 °C the dual-layered structure, which is observed after 1 h at 850 °C [27], is still observed after 3300 h at 650 °C (Figures 26 and 27).
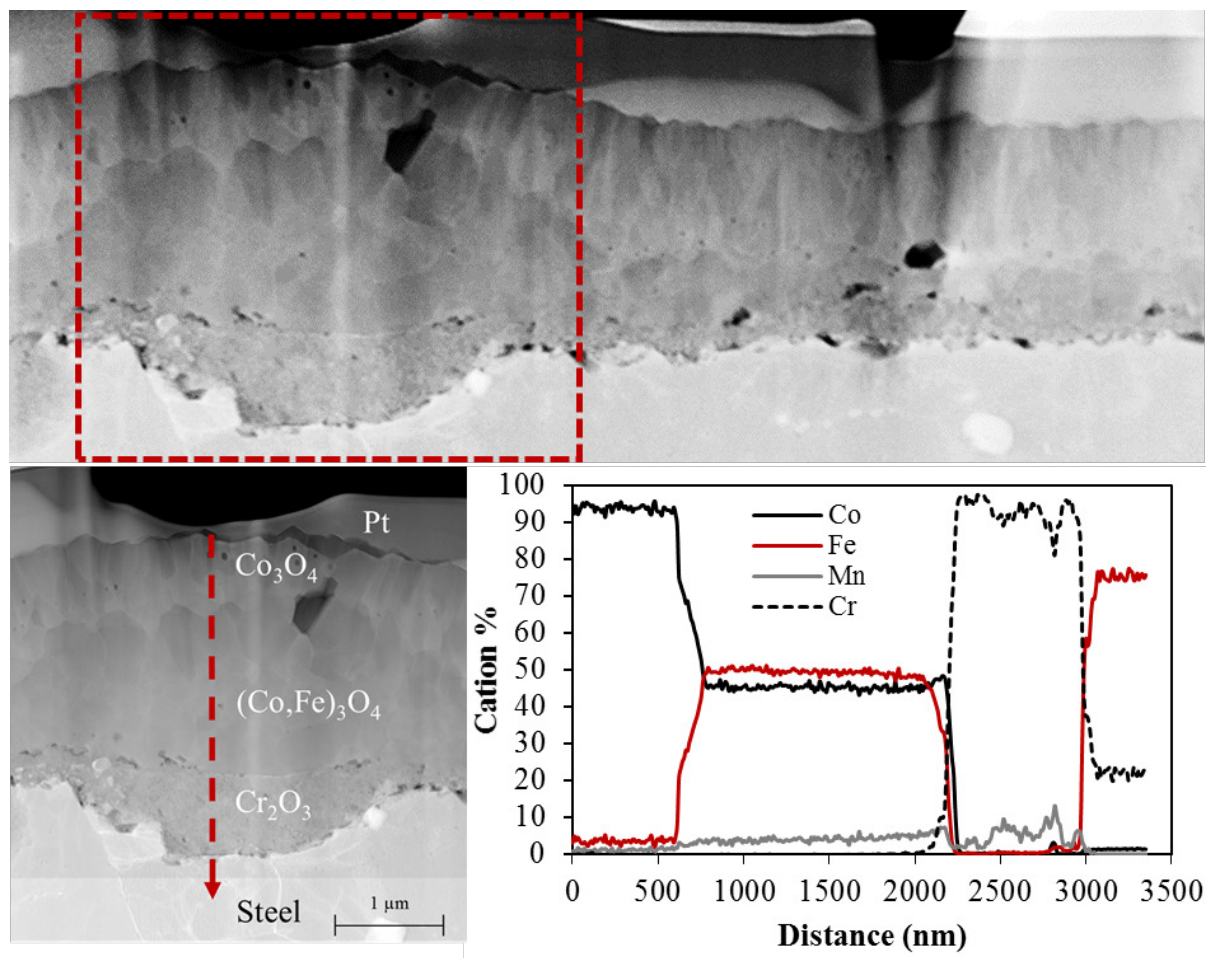
Figure 26: STEM/EDX line scan along the oxide layer of Co-coated Sanergy HT exposed for 3300 h at 650 °C in air containing 3% H$_2$O with a flow rate set to 6000 sml min^{-1}.

The other important factor, which is largely influenced by temperature, is outward diffusion of Mn from the steel into the oxidized Co-coating. At 650 °C only 2-3 cation % Mn could be detected in the Co-spinel after 3300 h (Figure 26) for the Co-coated material. Instead of diffusing out into the Co-spinel layer, Mn-enrichment was found at the metal-oxide interface, forming a layer of (Cr,Mn)$_3$O$_4$, that should be the stable phase at 650 °C in a low pO$_2$ environment, according to Jung [96]. This is most clearly visible in the STEM/EDX line scan from Figure 4b in Paper III. It can also be seen in the EDX maps (Figure 27), however, as the Kα value for Cr is close to that of Mn, a certain degree of overlap is expected in the EDX maps. This may be the reason for the Mn signal within the Cr$_2$O$_3$ scale. Nevertheless, since Mn is

indeed diffusing out to the Co-spinel, it must diffuse through the Cr_2O_3 scale. A certain amount of Mn is therefore expected to be found within the Cr_2O_3 scale, as can be seen in the STEM/EDX line scan above (Figure 26). Nevertheless, what can clearly be seen from the EDX maps is that as the temperature is increased by 100 °C, to 750 °C, much more Mn is incorporated into the Co-spinel compared to the amount incorporated at 650 °C (see EDX maps in Figure 27). These results can be compared to two TEM studies conducted at 850 °C for Sanergy HT coated with 640 nm Co [26, 27]. In these two studies the Mn concentration in the Co-spinel increased from ~15 to 26 cation % between 168 and 3000 h. A schematic drawing illustrating the effect the temperature has on the chemical composition of the Co-spinel layer(s), based on the results in this thesis and from [26, 27], is shown in Figure 28.
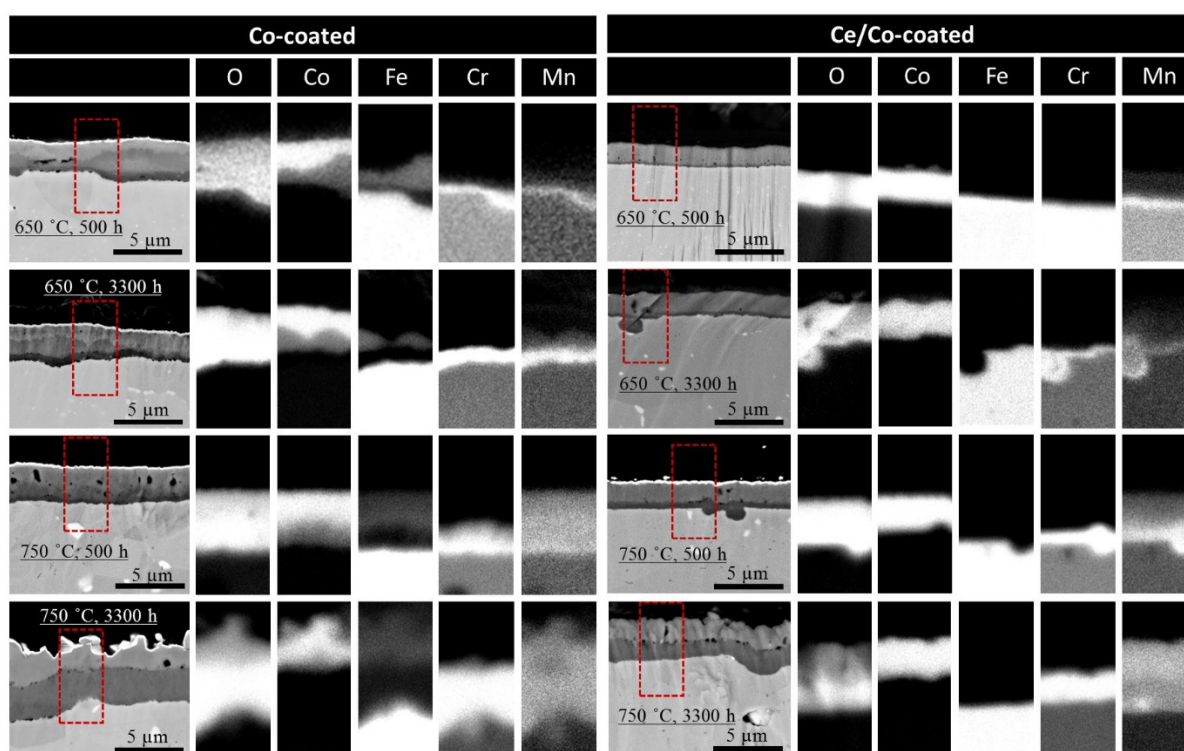
Figure 27: SEM images of Broad Ion Beam (BIB) milled cross-sections and their corresponding EDX maps for Co- and Ce/Co-coated Sanergy HT exposed for 500 and 3300 h at 650, and 750 °C in air containing 3% H_2O using a flow rate of 6000 sml min⁻¹. The Ce content was too low and the resolution of SEM/EDX analysis is inferior to the size of the Ce-rich particles/layer. Thus mapping Ce was not possible.

Ce/Co-coatings:

By adding an additional layer of 10 nm Ce between the steel and the Co-coating, the formation of a dual-layered Co-spinel, consisting of the two layers Co_3O_4 and $(Co,Fe)_3O_4$, is prevented. The metallic Co-coating is instead only converted into a single layer of Co_3O_4 (Figure 27). Due to the lack of Fe, the Co-spinel layer formed on the Ce/Co-material is somewhat thinner than the Co-spinel layer formed on the exclusively Co-coated material. At 750 °C (Figure 27) and at 850 °C [26], the Co_3O_4 layer is transformed into $(Co,Mn)_3O_4$ due to outward diffusion of Mn from the steel. At 650 °C, however, Mn is mainly present at the metal-oxide interface, as is the case for the exclusively Co-coated material (Figure 27). Both the effect of temperature and the

effect of an additional Ce-layer on the chemical composition of the Co-spinel layer is shown in Figure 28 as a simplified schematic drawing.
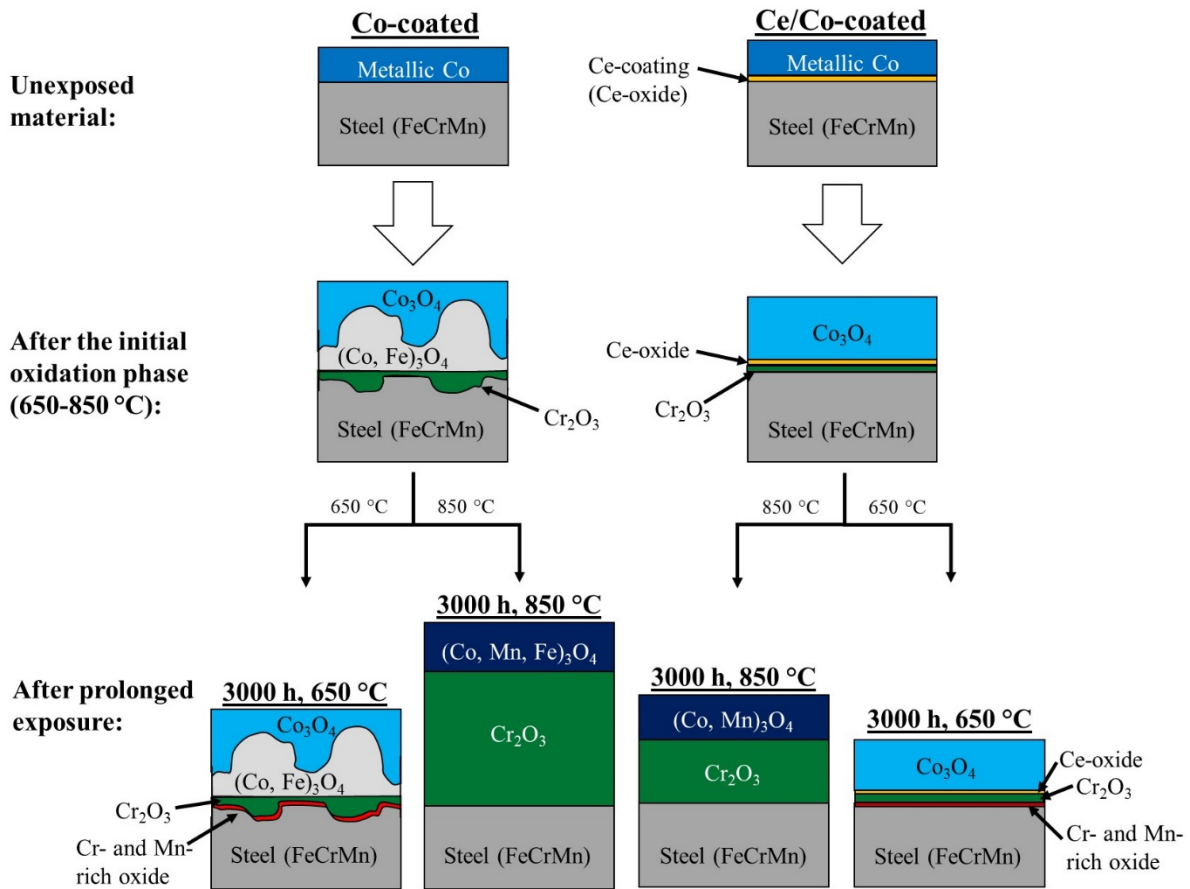
Figure 28: Schematic drawing illustrating the effect of temperature and the presence of a Ce-layer on the oxide scales formed on thin-film Co- and Ce/Co-coated materials at 650-850 °C. The drawing is based on the results in this thesis and from [26, 27].

Cr vaporization measurements:

As Figure 28 illustrates, the chemical composition of the Co-spinel top-layer is influenced by both temperature and the presence and absence, respectively, of a Ce-coating between the steel and the Co-coating. This variation in chemical composition of the Co-spinel did not have a noticeable effect on Cr vaporization (Figure 29). Both Co- and Ce/Co-coated Sanergy HT are able to effectively mitigate Cr vaporization at 650 and 750 °C, despite the difference in chemical composition of the Co-spinel top-layer. It can therefore be concluded that Cr vaporization is effectively mitigated from Co-coated steels, regardless of whether Mn and Fe are present in the Co-spinel top-layer or not.

Figure 29: Cr vaporization rate at (a) 650 °C and (b) 750 °C for uncoated (red dots), Co-coated (black triangles), and Ce/Co-coated (grey squares) Sanergy HT exposed for up to 3300 h in air containing 3% H_2O with a flow rate of 6000 sml min^{-1}.

Furthermore, isothermal Cr vaporization measurements from Co- and Ce/Co-coated Sanergy HT followed Arrhenius-type temperature dependence at 650-850 °C (see Paper III (Figure 3)). Activation energies of 92 and 107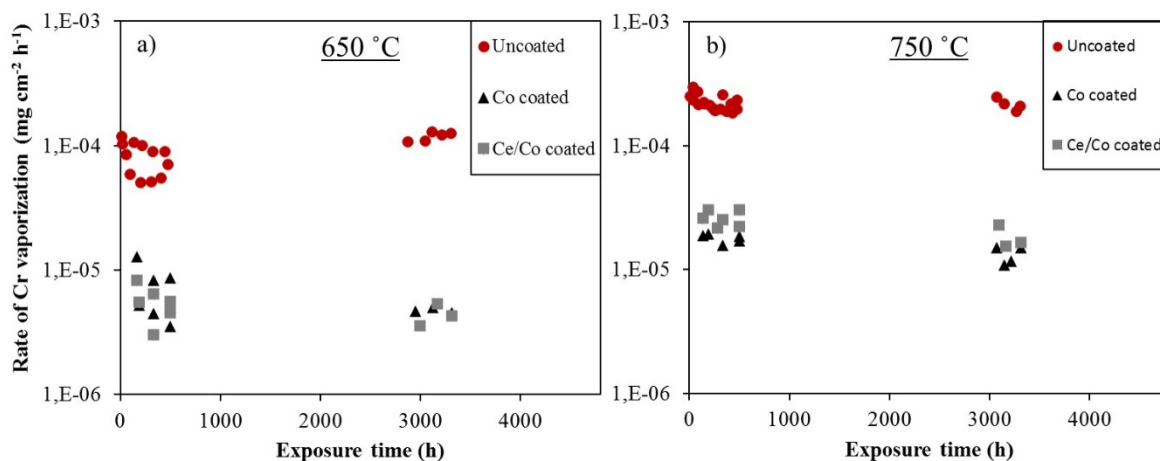 kJ mol^{-1} for Cr vaporization from Co- and Ce/Co-coated Sanergy HT were calculated. These values can be compared to the 91 kJ mol^{-1} that was the calculated activation energy value for the uncoated Sanergy HT material in section 5.1.5. All three values (uncoated, Co-coated, and Ce/Co-coated) are very close to the 85 kJ mol^{-1} measured from pure Cr_2O_3 (see section 5.1.6), as well as the 83 kJ mol^{-1} theoretically calculated by Panas et al. [104]. As was discussed already in section 5.1.6, it can be speculated that the Cr vaporization mechanism is the same, irrespective of whether chromium is vaporized from Cr_2O_3, uncoated Sanergy HT, or Co- respective Ce/Co-coated Sanergy HT.

Cr_2O_3 scale growth – the effect of temperature:
The main advantage of a decreased SOFC operating temperature, with respect to the interconnect, is most probably the substantially slower oxide scale growth rate of the moderately conductive chromia scale. As was shown in Section 5.1 the oxide scale growth is largely affected by the temperature. Substantially thinner Cr_2O_3 scales are formed by decreasing the operating temperature from 850 °C to 750 °C (compare Figures 24 and 27). However, both for the Co- and the Ce/Co-coated materials the Cr_2O_3 scales formed after 3300 h at 750 °C are still in the μm-range (Figure 27). By decreasing the temperature even further, down to 650 °C, the Cr_2O_3 scale growth rate is reduced to such an extent that the thermally grown Cr_2O_3 scales are less than one micrometre thick, even after 3300 h. In fact, after the initial oxidation phase, i.e. as the metallic Co-coating is converted into Co-spinel, almost no further gain in mass can be observed at 650 °C (Figure 30a), indicating that no substantial growth of the Cr_2O_3 scale took place after the first hours of exposure. Evidence for this can be seen in Figure 27, where no significant difference in thickness of the Cr-rich oxide scale can be seen between 500-3300 h.
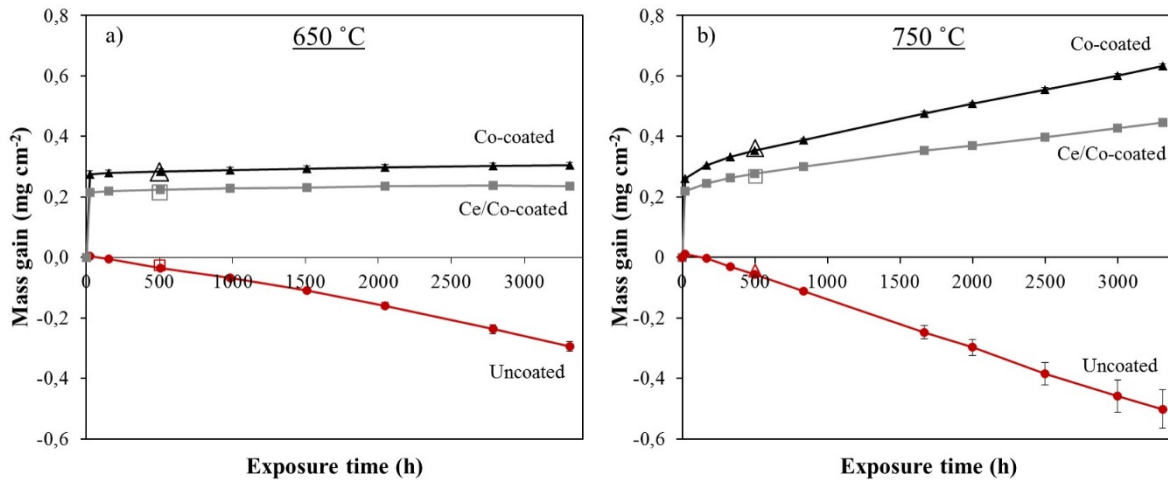
Figure 30: Mass gain values at (a) 650 °C and (b) 750 °C for uncoated (red dots), Co-coated (black triangles), and Ce/Co-coated (grey squares) Sanergy HT exposed for up to 3300 h in air containing 3% H_2O with a flow rate of 6000 sml min^{-1}. Both isothermal (500 h) and discontinuous (3300 h) exposures are shown.

Cr_2O_3 scale growth – the effect of Ce:

At 650 °C:

Although the average chromia scale thickness was even thinner for the Ce/Co-coated material compared to the exclusively Co-coated material at 650 °C, both materials had developed very thin chromia scales. Furthermore, since the chromia scales formed on both the Co- the Ce/Co-coated materials grow extremely slowly at 650 °C it can be questioned whether the additional Ce-layer has any beneficial effect if the SOFC stack is operating at 650 °C. Nevertheless, a thermal gradient of 50-100 °C is very common in a stack and an increase of 50-100 °C locally would have a rather significant effect on the thickness of the chromia scale, as can be seen from Figure 27. For this reason, adding the extra Ce-layer should still be of advantage for the long-term performance, even if the stack is designed to operate at temperatures as low as 650 °C.

At 750 °C:

At 750 °C a significant improvement in oxidation resistance is observed for the Ce/Co-coated material compared to the exclusively Co-coated material (Figures 27 and 30). Between 500-3300 h the Cr_2O_3 scale thickness increased by almost 2 μm for the Co-coated material, whereas for the Ce/Co-coated material the Cr_2O_3-scale thickness only increased by 1 μm (Figure 27). It is well-known that reactive elements such as Ce, La, Hf, Zr, and Y can improve the oxidation resistance at high temperatures, however, the exact mechanisms behind the observed reactive element effect are still under debate [31]. As was discussed in Section 3.3, the most widespread theory for chromia scale growth is based on the assumption that the dominating growth mechanism is chromium outward diffusion. In the case a reactive element has been added to the alloy, or as a coating, the reactive element may segregate at the Cr_2O_3 scale grain boundaries, blocking outward diffusion of chromium ions. This has been shown by Cotell et al. [77] using ^{18}O-tracer experiments and TEM analysis on yttrium (Y) ion-implanted pure chromium. In that study, the rate of chromium outward diffusion was reduced to such an extent that the smaller flux of oxygen inward diffusion became the dominant mechanism for scale

growth. This not only reduces oxide scale growth but also results in better scale adhesion, since a reduced outward flux of Cr ions corresponds to a reduced inward flux of metal vacancies. This in turn reduces the amount of voids at the metal-oxide interface. Figure 31 shows SEM cross-section images for both the Co- and the Ce/Co-coated material after 500 h and 3300 h at 750 °C.
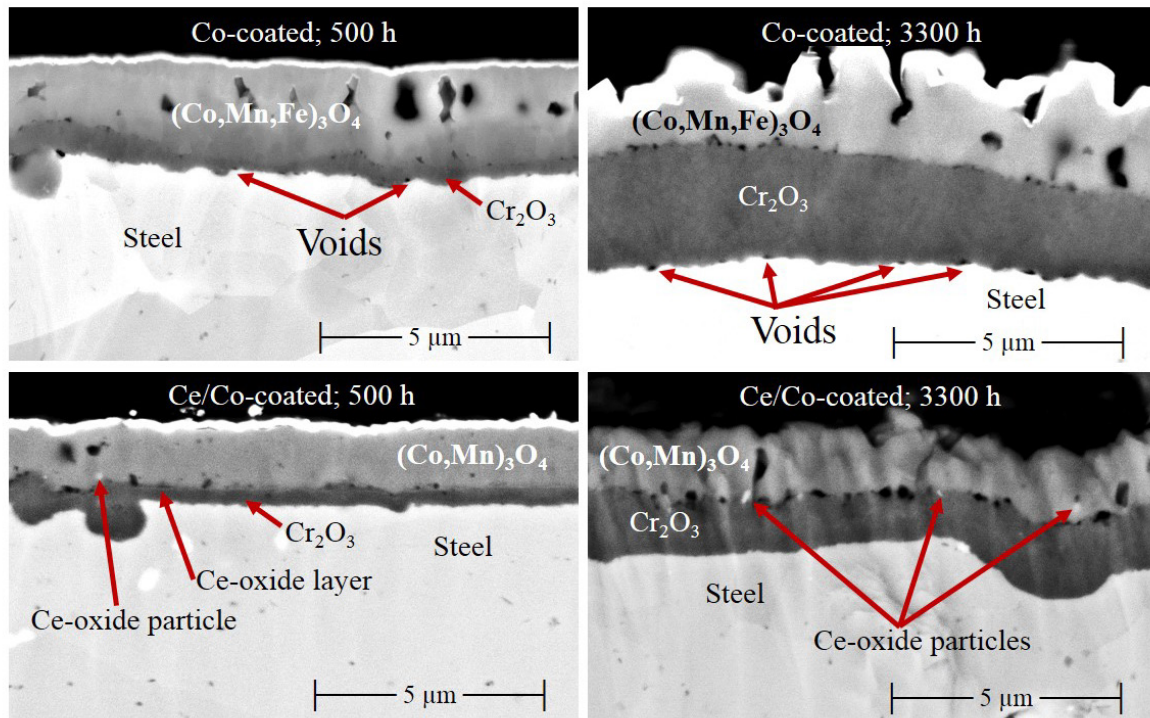

Figure 31: SEM images of Broad Ion Beam (BIB) milled cross-sections for Co- and Ce/Co-coated Sanergy HT exposed for 500 and 3300 h at 750 °C in air containing 3% H_2O using a flow rate of 6000 sml min^{-1}.

From these images it can be seen that almost no voids exist at the metal-oxide interface for the samples coated with Ce/Co, whereas for the samples only coated with Co some voids can be seen at the metal-oxide interface. Furthermore, by comparing the 500 h sample with the 3300 h sample, for the exclusively Co-coated material, it seems as if more, and larger, voids are created with prolonged exposure time. This would support the above mentioned theory, that outward diffusion of Cr is reduced as an effect of the Ce-layer. Furthermore, in Figure 31 (see also Figures 33 and 34) a bright layer at the $(Co,Mn)_3O_4$-Cr_2O_3 interface can be seen for the Ce/Co-coated material after 500 h. This layer is assumed to be a layer of Ce-oxide, and is therefore not seen for the exclusively Co-coated material. Such a layer was also seen for the Ce/Co-coated material at 650 °C (Figures 33 and 34). The fact that the Cr_2O_3 scale is located below this bright layer could be argued to be proof that the chromia scale mainly grows by inward oxygen diffusion. Nevertheless, with continued exposure time (after 3300 h) this layer disappears at 750 °C (not at 650 °C). Instead bright particles are seen at the $(Co,Mn)_3O_4$-Cr_2O_3 interface, and within the $(Co,Mn)_3O_4$ layer (Figure 31). Furthermore, in a TEM study by Canovic et al. [26] such bright particles were identified as Ce-oxide. In that study these particles were found in the middle of the $(Co,Mn)_3O_4$ layer after 168 h at 850 °C. It is therefore assumed that Ce migrates towards the surface, and can thus not be used as a marker in order to determine the oxide scale growth direction. In fact, it has previously been shown that reactive elements,

as oxygen active elements, diffuse outwards towards the gas-oxide interface during exposure [30]. Due to the low solubility of reactive elements in the oxide scale, these are assumed to diffuse along the grain boundaries. The location for the bright particles, which are assumed to be Ce-oxide particles, observed after 500 h and 3300 h in Figure 31, may initially have been voids, and as Ce is diffusing outwards, along the grain boundaries, Ce might accumulate within these voids forming Ce-oxide particles. Nevertheless, in order to prove that the beneficial effect of the Ce-coating is attributed to Ce in the Cr_2O_3 grain boundaries, and thereby impeding outward diffusion of chromium, Ce needs to be detected within the Cr_2O_3 grain boundaries. As Sattari et al. [88] studied 10 nm Ce-coated Sanergy HT that was exposed at 850 °C, utilizing TEM/EELS, Ce was found both as Ce-oxide particles at the surface of the oxide scale and segregated at the grain boundaries of the $(Cr,Mn)_3O_4$ top-layer in the vicinity of the oxide-gas interface. Despite the dedicated analysis, no Ce was detected within the Cr_2O_3 scale, which is hard to reconcile with the theory discussed above. Whether this is the case for the Ce/Co-coated samples in the present study is currently unknown. In order to gain deeper knowledge of what is causing the superior oxidation resistance of the Ce/Co-coated material compared to the exclusively Co-coated material at 750 °C, this needs to be investigated further in a future study.

Area Specific Resistance (ASR) measurements:

ASR at 650 ˚C:
The electrical resistance of a semiconductive oxide scale increases with decreasing temperature. Common activation energy values for electrical conductivity of pure Cr_2O_3 and thermally grown oxide scales formed on Cr_2O_3-forming alloys lies in the span 20-80 kJ mol^{-1} [81, 108-110]. In section 5.1.5 an activation energy of approximately 270 kJ mol^{-1} was calculated for oxide scale growth on Sanergy HT and Crofer 22 H in air. Other researchers have found similar activation energy values for oxide scale growth on Cr_2O_3-forming alloys in air [97, 100, 102]. Despite the semiconductive properties of the oxide scale, a decrease in operating temperature will therefore most probably lead to a lower electrical resistance of the thermally grown oxide scale, at least after longer exposure durations. This is, however, not the case for the oxidized Co-coating, since no substantial effect of the Co-oxide thickness can be expected with decreased temperature. The chromia scales formed on the Co- and Ce/Co-coated materials after 500 h at 650 °C in this work are only a hundred to a few hundred nanometres thick whereas the Co-oxide thickness is around 1.5-2 μm. It can therefore be speculated that the contribution of the Co-spinel coating to the total ASR is greater at lower temperatures compared to at 850 °C, where the Cr_2O_3 scale may be equally thick, or even thicker, than the Co-spinel top-layer (see Figure 34c and f). Furthermore, as was shown above, very little Mn was found in the Co-spinel at 650 °C, irrespective of whether the steel is coated exclusively with Co or with Ce/Co. Petric and Ling [16] have measured the electrical conductivity for $MnCo_2O_4$, Co_3O_4, and $CoFe_2O_4$ at 800 °C. According to their measurements, the electrical conductivity of Co_3O_4 (6.7 S/cm) is almost one order of magnitude lower than the electrical conductivity of $MnCo_2O_4$ (60 S/cm). Furthermore, for the exclusively Co-coated material, the metallic Co-coating is converted into a Co_3O_4 top-layer and a layer of Fe-rich $(Co,Fe)_3O_4$ underneath. Since the measured electrical conductivity of $CoFe_2O_4$ (0.93 S/cm) is almost seven times lower than the electrical

conductivity of Co_3O_4 according to the measurements by Petric and Ling [16], a substantial difference in ASR should be noticed between the Co- and Ce/Co-coated material if the Co-spinel is contributing to the total ASR of the coated material. ASR measurements in Figure 32, from Co- and Ce/Co-coated Sanergy HT after 500 h at 650 °C, do indeed show a somewhat lower ASR for the Ce/Co-coated material compared to the exclusively Co-coated material. However, the Ce/Co-coated material had also formed an even thinner chromia scale, which may very well be the main reason for the somewhat lower ASR measured on the Ce/Co-coated material. Since both the Co- and the Ce/Co-coated samples showed very low ASR values after 500 h at 650 °C (4-8 mΩcm², see Figure 32), it can be concluded that the electrical resistance caused by the Co-oxide is very low and that a low Mn- and high Fe-content in the Co-oxide not is an issue. As long as the Co-coating is thin, a growing chromia scale would be the main contributor to an increase in electrical resistance.
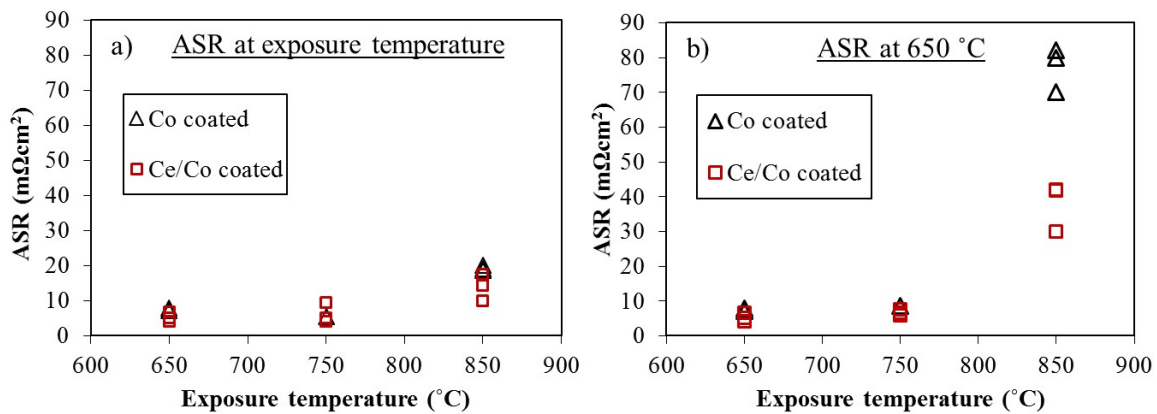

Figure 32: ASR measurements carried out on Co-coated (black triangles) and Ce/Co-coated (red squares) Sanergy HT exposed isothermally for 500 h in air containing 3% H_2O before Pt-electrodes were contacted and ASR was measured. In (a) ASR was measured at the corresponding exposure temperature (650, 750 or 850 °C), and in (b), the ASR was measured at 650 °C for the very same samples as in (a).

A comparison between Ce/Co-coated Sanergy HT and Ce/Co-coated AISI 441 at 650 °C:
At lower temperatures custom-made steels for SOFC, such as Sanergy HT, may not be necessary, and instead already existing steel grades can be used that cost significantly less. The steel grade AISI 441 has been considered as a possible candidate as an interconnect steel for SOFCs. AISI 441 coated with 20 nm Ce + 600 nm Co was exposed for 500 h at 650 °C in air containing 3%H_2O (6000 sml min^{-1}). Cr vaporization was measured during the isothermal exposure and ASR was measured on the 500 h exposed samples. The results compared to the results previously presented for the Ce/Co-coated Sanergy HT steel are shown in Figure 33. It can be concluded that both steels, when coated with a Ce/Co-coating, mitigate Cr species vaporization, form very thin chromia scales, and as a consequence show low ASR values at 650 °C (Figure 33). The steel AISI 441 could therefore be considered as a promising candidate for SOFCs intended to operate at lower temperatures.
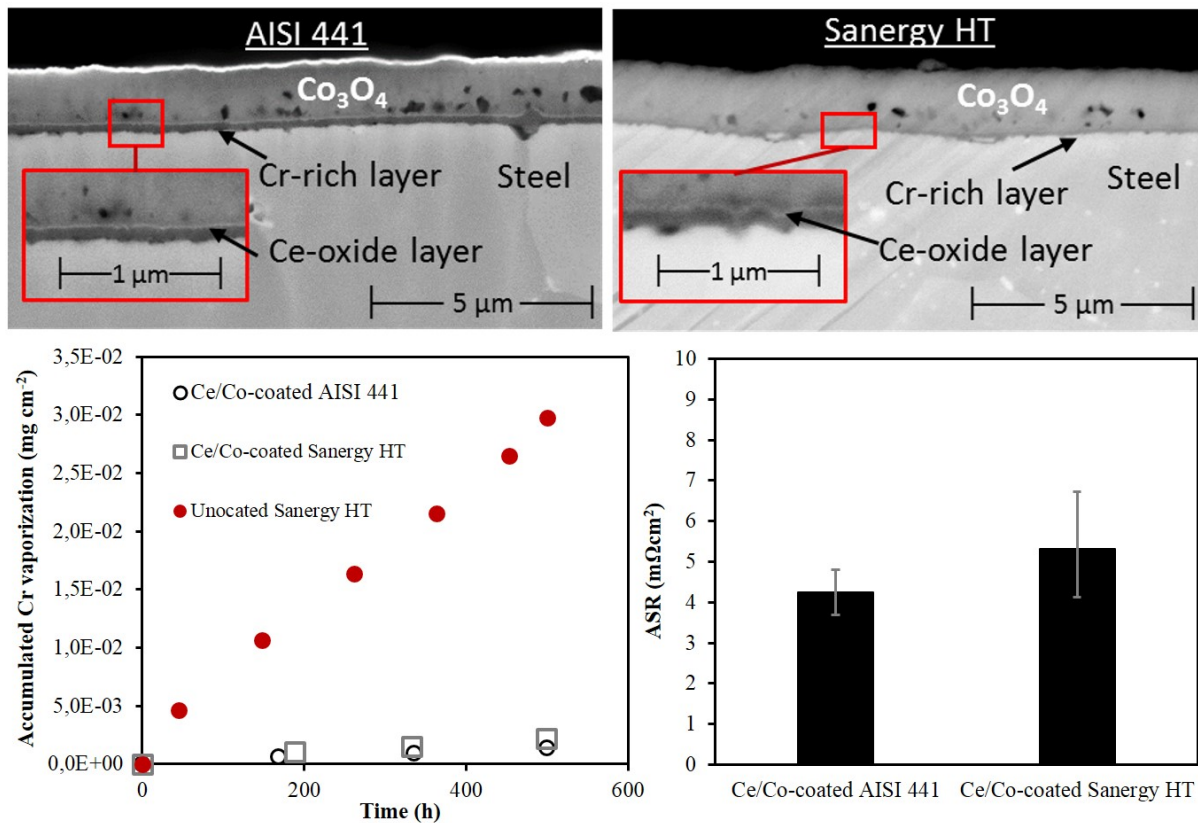
Figure 33: SEM images of Broad Ion Beam (BIB) milled cross-sections for Ce/Co-coated AISI 441, and Ce/Co-coated Sanergy HT exposed for 500 at 650 °C in air containing 3% H_2O using a flow rate of 6000 sml min^{-1}. The corresponding Cr vaporization measurements (left) and ASR measurements (right) are shown below the two SEM images. Cr vaporization was measured during the 500 h isothermal exposure, whereas the ASR was measured after the 500 h exposure.

ASR at 750 °C:

As the ASR measurements at 650 °C in Figure 32 proved, the electrical resistance of the Co-spinel top-layer (for a 640 nm Co-coatings) is not contributing to a high ASR and can more or less be neglected. What cannot be neglected is a growing Cr_2O_3 layer, which has a significant effect on the ASR as was seen in the previous section, as well as by other authors [105, 111]. In the present study ASR measurements were carried out after 500 h of exposure. Both the Co- and Ce/Co-coated samples showed rather thin Cr_2O_3 scales (< 1 μm) after 500 h at 750 °C, and, consequently, no clear difference in ASR was measured between the two materials. However, the long-term ASR measurements at 850 °C in section 5.2.1 clearly shows that the ASR is increasing with increasing Cr_2O_3 scale thickness and it can therefore be assumed that the observed slower Cr_2O_3 scale growth rate for the Ce/Co-coated material at 750 °C, over the long-term, will significantly reduce electrical scale resistance compared to the exclusively Co-coated material.

5.2.3 The importance of measuring ASR at the desired operating temperature

Solid Oxide Fuel Cells are expected to show stable performance for a minimum period of 40 000 h (~5 years), and therefore a somewhat increased temperature is a frequently used method to gain valuable long-term data within a practical timeframe. However, as corrosion studies are carried out in combination with ASR measurements, ASR measurements are commonly conducted at the same temperature as the exposure temperature. In Figure 32a it could be seen that the ASR (at 850 °C) is somewhat lower for the Ce/Co-coated material after 500 h at 850 °C, compared to the exclusively Co-coated material. However, since the difference is only a few $m\Omega cm^2$, it can be assumed that these two materials show comparable ASR after 500 h at 850 °C, although the Cr_2O_3 scale was almost 1 µm thinner for the Ce/Co-coated material (Figure 34). As the ASR was measured on the same samples at 650 °C (after cooling down from 850 °C), both materials showed substantially higher ASR values, as expected due to the semiconductive properties of the oxide scale (compare Figure 32a with 33b). However, what seemed to be a rather small difference at 850 °C (~5 $m\Omega cm^2$ difference), is actually a substantial difference at 650 °C (~40 $m\Omega cm^2$ difference). It is therefore crucial to actually measure the ASR at the intended SOFC operating temperature, even if the corrosion studies are carried out at a somewhat higher temperature. Moreover, these chromia scales formed on the Co- and Ce/Co-coated materials after 500 h at 850 °C were 2-4 µm thick (Figure 34), which is the reason for the high ASR values at 650 °C. Such thick chromia scales are not expected to form at temperatures as low as 650 °C (Figures 34 and 27). In the present study, however, coatings were applied by Physical Vapour Deposition (PVD). Application of $(Co,Mn)_3O_4$-coatings, in the form of a powder is another common method used to produce coated interconnects for SOFCs. In order to densify the $(Co,Mn)_3O_4$-powder, the coated interconnect is subjected to a heat treatment, and as a consequence µm thick Cr_2O_3 scales may be formed due to the heat treatment [18, 112, 113]. If the desired operating temperature is high e.g. 850 °C, the formation of a thick Cr_2O_3 scale during the heat treatment would not have a significant effect on the electrical scale resistance. However, if the stack is designed to operate at a temperature as low as 650 °C the heat treatment may have a significant effect on the electrical scale resistance. Therefore, metallic conversion coatings, as well as coatings deposited with other techniques that do not require a heat treatment, such as plasma spraying etc., seem to be the most suitable coating techniques for interconnects intended to be used in stacks designed to operate in the 600-700 °C temperature range.
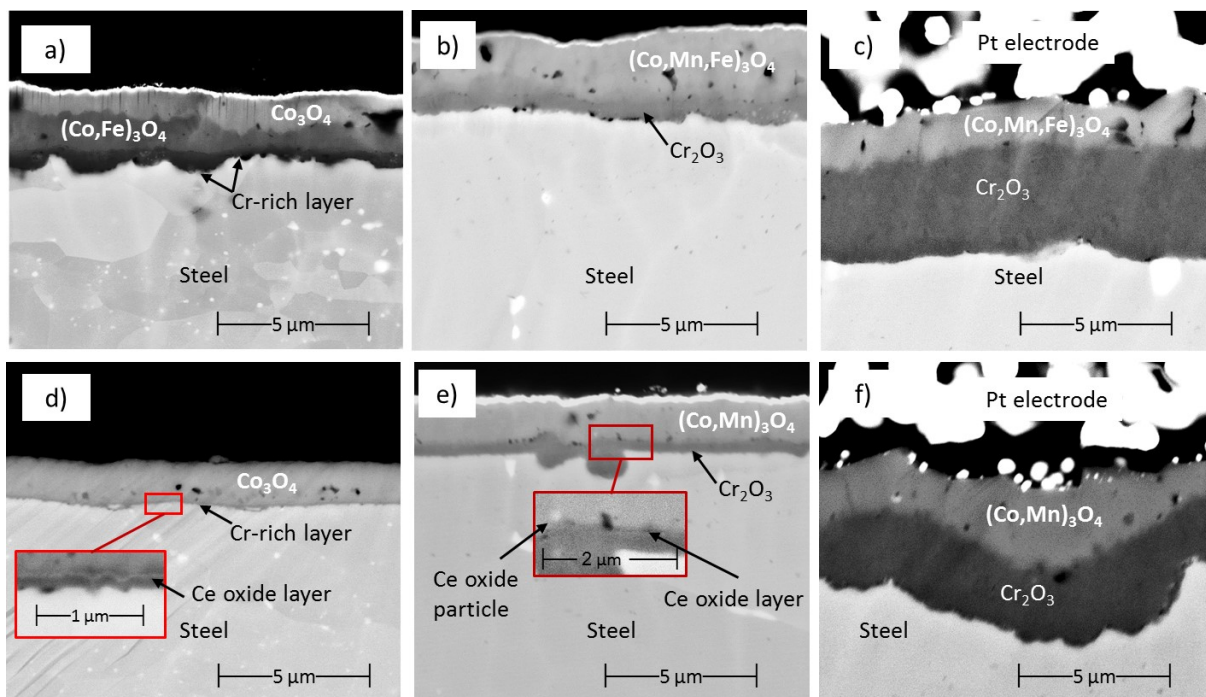
Figure 34: SEM images of Broad Ion Beam (BIB) milled cross-sections showing the oxide scales of the materials used for ASR measurements in Figure 32. Images a-c show the oxide scales for the Co-coated material after 500 h at 650, 750, and 850 °C, and d-f show the oxide scales for the Ce/Co-coated material after 500 h at 650, 750, and 850 °C.

5.2.4   The effect of Co-coating thickness at 650 °C

In this work thin-film Co- and Ce/Co-coatings that were applied by Physical Vapour Deposition (PVD) have been studied. However, other techniques such as electroplating [25, 75, 114] and sol-gel deposition [83, 115] etc. can also be utilized to deposit metallic Co (or Co-alloy) conversion coatings. The thickness of the electroplated Co-coating in the cited study by Harthøj et al. [25], was ~2 µm, and other researchers have studied metallic Co-coatings having a Co-coating thickness of up to 40 µm [28, 75]. A thick Co-spinel layer is not expected to contribute to the ASR to any noticeable extent at high temperatures (~800 °C), since the substantially less conductive chromia scale grows rapidly to become several µm thick. However, as the SOFC operating temperature decreases, and as a consequence the thickness of the Cr_2O_3 scale is reduced significantly (Figure 34), the contribution of the oxidized Co-coating to the total electrical resistance of the oxide scale may be more relevant. Especially when considering that virtually no Mn is incorporated into the Co-oxide at 650 °C (see Section 5.2.2), which clearly should have a negative effect on the electrical conductivity of the Co-spinel according to Petric and Ling [16].

ASR measurements on Sanergy HT uncoated and coated with 200, 600, 1000, and 1500 nm Co, measured after 168 and 500 h at 650 °C in air, shows that with increasing Co-coating thickness the ASR also increases (Figure 35).
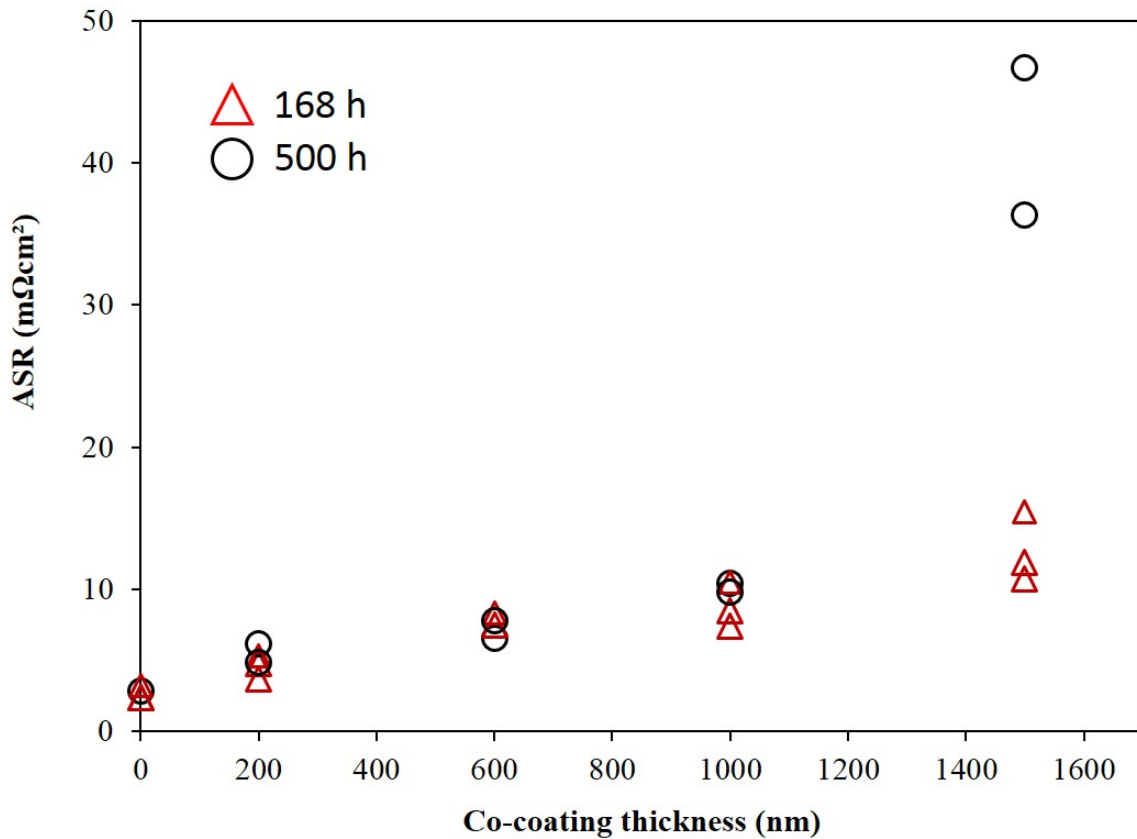
Figure 35: Area Specific Resistance (ASR), as a function of Co-coating thickness on Sanergy HT, measured in air at 650 °C, after isothermal exposures at 650 °C in air for 168 h (red triangles) and 500 h (black circles).

All Co-coated samples had formed a dual layered Co-oxide after 500 h at 650 °C, consisting of an outer Co_3O_4-layer and an inner Fe-rich $(Co,Fe)_3O_4$-layer (Figure 36). With increasing Co-coating thickness, a clear increase in the thickness of the $(Co,Fe)_3O_4$-layer can be seen, whereas the thickness of the Co_3O_4 top-layer is almost unaffected by the thickness of the Co-coating. Furthermore, for the 1500 nm Co-coated material a layer of almost pure Fe-oxide was also found between the $(Co,Fe)_3O_4$-layer and the thermally grown $(Cr,Fe)_2O_3$ scale. However, not only an increase in the Co-oxide thickness can be seen as an effect of increased Co-coating thickness. The thickness of the thermally grown $(Cr,Fe)_2O_3$ scales at the metal-oxide interface also substantially increased with increased Co-coating thickness. The increase in $(Cr,Fe)_2O_3$ scale thickness is thus assumed to be the real cause for the increase in ASR as a function of Co-coating thickness seen in Figure 35, and not the thicker layer of Co-oxide.
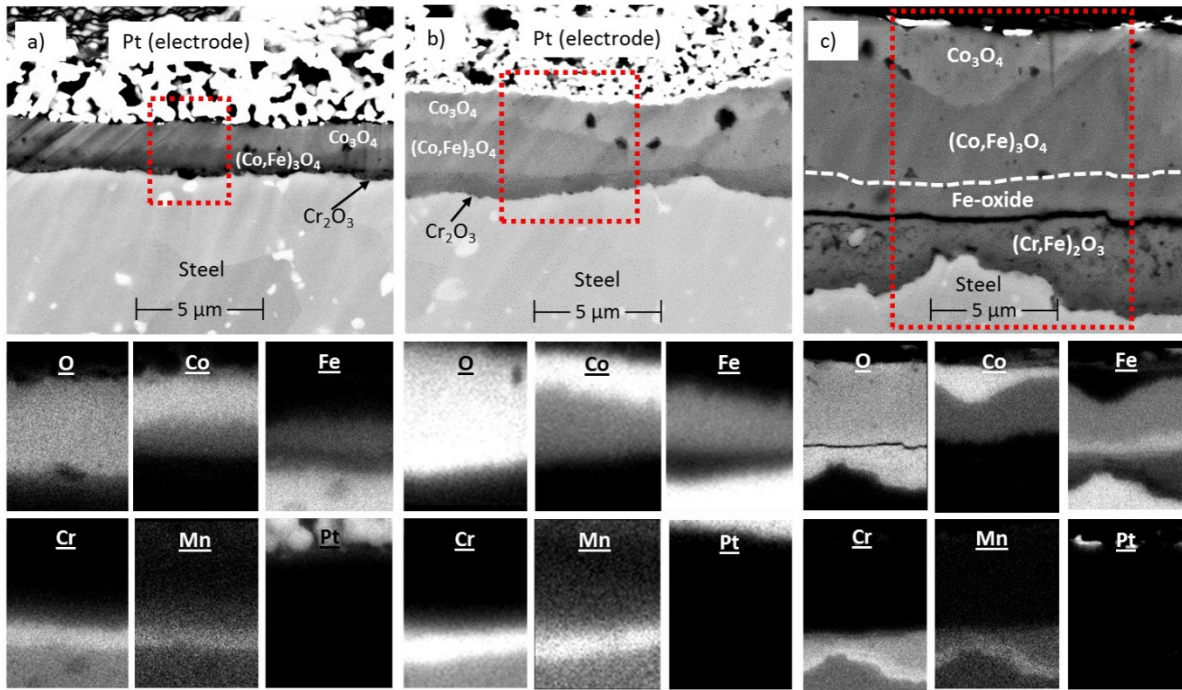
Figure 36: SEM images of Broad Ion Beam (BIB) milled cross-sections and their corresponding EDX maps of Sanergy HT coated with (a) 600 nm Co, (b) 1000 nm Co, and (c) 1500 nm Co after 500 h at 650 °C in air.

In Section 5.2.2 it was shown that at 650 °C only a very limited gain in mass, and thus also only a very limited growth of the chromia scale, is expected after the first hours of exposure for ~600 nm Co-coated Sanergy HT. Those results agree well with the mass gain data in this study, showing a very limited change in mass between 4-500 h for the 600 nm Co-coated Sanergy HT material at 650 °C (Figure 37). The assumption that the chromia scale was formed within the first hours of exposure, and from there onwards the thickness of the chromia scale remained more or less unchanged agrees very well with the ASR measurements, since no difference in ASR can be seen between the samples exposed for 168 and 500 h.

Figure 37: Mass gain values for uncoated (black circles), 200 (grey circles), 600 (black squares), 1000 (grey squares), and 1500 nm (black triangles) Co-coated Sanergy HT isothermally exposed for 0.1, 1, 4, 168 and 500 h in air at 650 °C. The error bars represent the maximum and minimum mass gain.

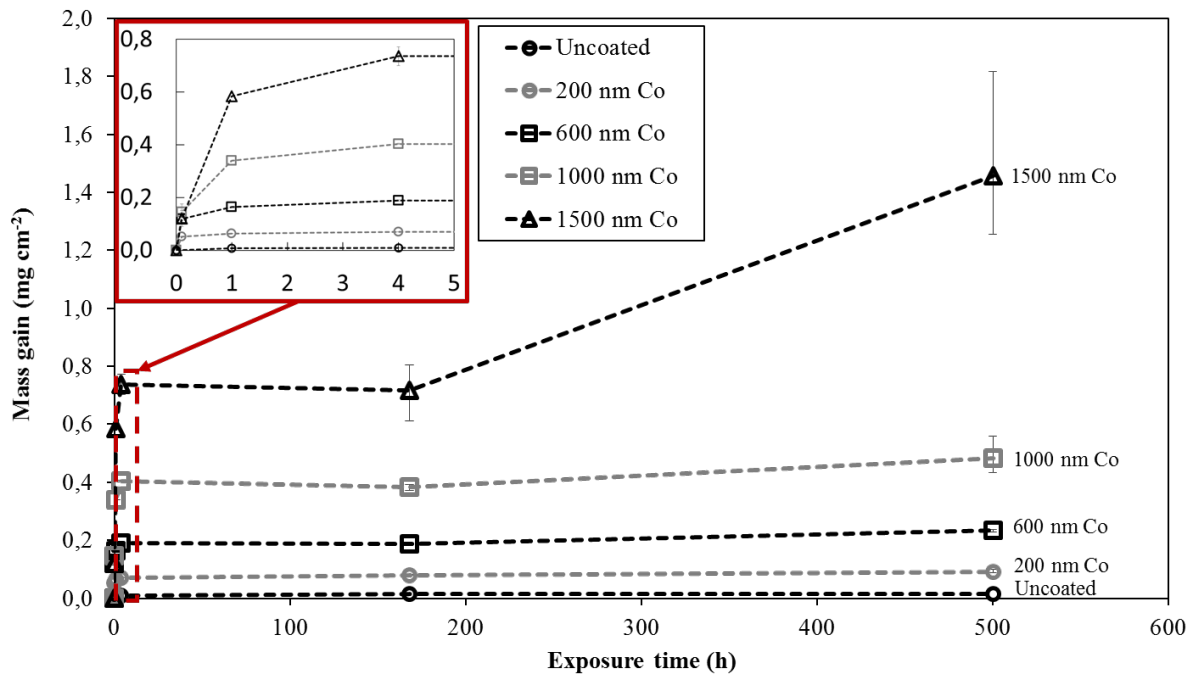This observation is not only true for the 600 nm Co-coated material, but for all materials coated with ≤ 1000 nm Co. After the first 4 hours of exposure the mass remained almost unchanged, and no increase in ASR could be seen from 168 to 500 h of exposure. Nevertheless, a clear increase in ASR as a function of Co-coating thickness is still observed for the samples coated with up to ≤ 1000 nm Co, both after 168 and after 500 h of exposure (Figure 35). Since no increase in either mass or ASR is observed with continued exposure time for these materials (≤ 1000 nm Co) at 650 °C it can be assumed that the oxide scale that is causing the ASR was formed during the initial oxidation phase (see paper IV for a more detailed investigation of the initial oxidation phase). The mechanism is assumed to be the same for all Co-coating thicknesses. The only difference for the thinner Co-coatings is that a protective chromia scale is established faster, and as a consequence thinner chromia scales are formed for these materials. It can therefore be speculated that the metallic Co-coating has a negative effect on the formation of a protective chromia scale. In the study by Harthoj et al. [25], no obvious negative effect of the 2 μm "thick" Co-coating was noticed, although the thickness of that coating was even thicker than the thickest Co-coating in the present study (1500 nm). The substrate steel investigated by Harthoj et al. [25] was not Sanergy HT. Instead the steel Crofer 22 APU was coated with ~2 μm Co in that study. However, an effect of the substrate material can be excluded since the Crofer 22 APU steel was also coated with 1500 nm Co, and no difference in ASR or oxide scale microstructure was seen between Sanergy HT and Crofer 22 APU, as these two steels were coated with 1500 nm Co and exposed for 168 h at 650 °C (see Paper IV). Furthermore, since the Co-oxide layer in the study by Harthoj et al. [25] contained Fe, it can be assumed that this material also initially formed a dual layered Co-oxide consisting of a Co_3O_4 top-layer and a layer of $(Co,Fe)_3O_4$ underneath, and thus the same mechanism initially took place also for the 2 μm Co-coated Crofer 22 APU material at 800 °C. The main difference

between the present study and the study by Harthoj et el. [25] is the substantially higher exposure temperature in [25]. At 800 °C the kinetics are faster, and as a consequence Cr is supplied faster to the metal-oxide interface, enabling the formation of a protective chromia scale. As Young et al. [116] exposed uncoated Crofer 22 APU in an Ar-4%H_2-20%H_2O environment at 500-900 °C, low mass gains and thin oxide scales were formed at 800 °C on the Crofer 22 APU steel. As the temperature was decreased to 700 °C even lower mass gains were recorded, as expected. However, as the temperature was reduced even further, to 550-650 °C, a significant increase in mass gain and oxide scale thickness was observed for the Crofer 22 APU steel in the Ar-4%H_2-20%H_2O environment. Due to the reduced temperature less Cr was supplied to the steel-oxide interface, and as a consequence a passivating chromia scale was not able to form at 550-650 °C on the Crofer 22 APU steel in the H_2/H_2O atmosphere. Due to the very low mass gains for the uncoated Sanergy HT steel at 650 °C in air (Figure 37), it can be concluded that this material has the potential to form a passivating chromia scale at 650 °C in air. However, as Figure 36 shows, the presence of a metallic Co-coating clearly supresses the formation of a protective chromia scale at 650 °C. Furthermore, since no noticeable difference in chromia scale thickness was observed between the uncoated and the 2 μm thick Co-coated Crofer 22 APU material after 3000 h at 800 °C in the study by Harthoj et al. [25] it can be assumed that the lower temperature, which leads to slower supply of Cr, is the main cause of the accelerated corrosion as an effect of the Co-coating thickness seen in the present study. From Section 5.2.2, and earlier published works [26, 32, 105], it has been shown that by adding a 10 nm Ce layer between the metallic Co-coating and the steel substrate, virtually no Fe is found in the Co-oxide after exposure at 650-850 °C. This suggests that a Cr- and Fe-rich oxide scale, which is formed initially for the exclusively Co-coated material (see Figure 5 in Paper IV), was not initially formed for the Ce/Co-coated samples. This might be correlated to the reactive element effect (see Section 3.3). However, it might also be correlated to the presence of a layer between the metallic Co-coating and the steel, separating them from each other. To prevent metal-metal contact between the steel and the metallic Co-coating, without the influence of a reactive element coating, uncoated Sanergy HT was pre-oxidized in air at 900 °C for 3 minutes and subsequently coated with metallic Co. Based on mass gain the oxide scale separating the coating from the steel was only ~40 nm thick. Figure 38 shows a comparison between the regular (metal-metal contact) 1500 nm Co-coated Sanergy HT material and the pre-oxidized 1500 nm Co-coated Sanergy HT material, after 168 h at 650 °C.
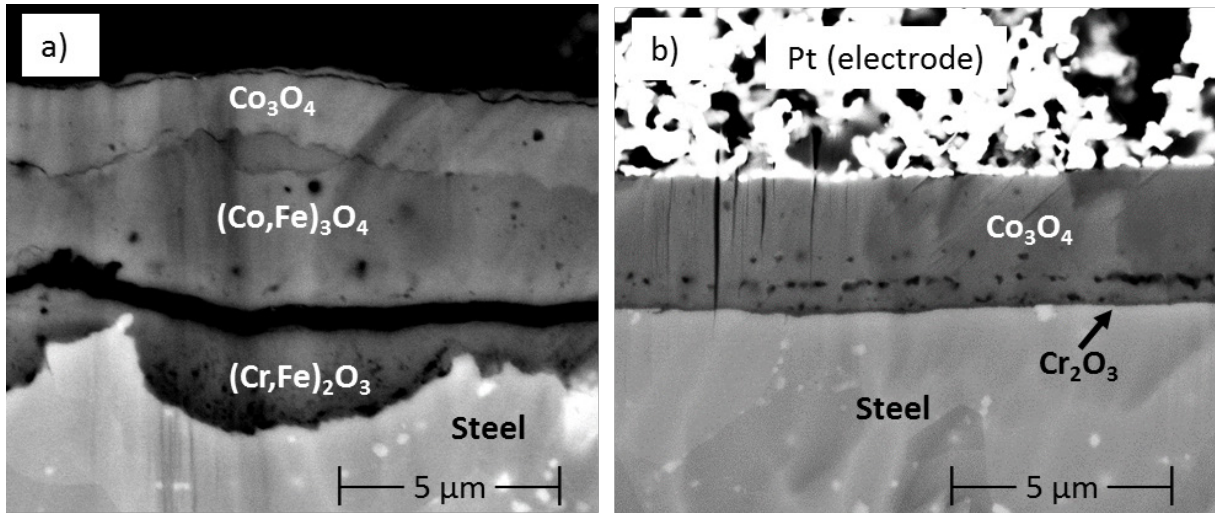
Figure 38: SEM images of Broad Ion Beam (BIB) milled cross-sections of (a) Sanergy HT coated with 1500 nm Co and (b) Sanergy HT pre-oxidized (3 min at 900 °C) and subsequently coated with 1500 nm Co after 168 h at 650 °C in air.

A significant effect of the pre-oxidation step can be seen. For the pre-oxidized material only a very thin (~100 nm) and homogenous layer, which is assumed to be Cr_2O_3, was formed at the metal-oxide interface, compared to a substantially thicker and less homogenous layer formed on the sample that was not pre-oxidized before the Co-coating was deposited on the steel surface. The microstructure observed for the pre-oxidized material is very similar to the microstructure seen for the Ce/Co-coated Sanergy HT steel at 650 °C in section 5.2.2. This indicates that the metal-metal contact between the steel and the Co-coating is supressing the formation of a protective chromia scale. The metal-metal contact between the steel and Co-coating might lead to dissolution of Co into the steel at the steel-coating interface. This would locally lower the Cr activity of the steel. Moreover, solution of Co into the steel might also affect diffusion of Cr in the steel, or/and the nucleation process for Cr_2O_3, and thus delay the formation of a continuous protective chromia scale. More analyses are needed, however, in order to draw any further conclusion regarding the mechanism behind the detrimental effect of the metallic Co-coating at 650 °C. Nevertheless, the significantly thinner chromia scales formed on the pre-oxidized samples had a substantial effect on the ASR (Figure 39). Both the 200 and 1500 nm pre-oxidized and subsequently Co-coated materials showed ASR values around 5 $m\Omega cm^2$ after 168 h at 650 °C, which is almost a factor three lower than for the regular 1500 nm Co-coated Sanergy HT material after the same exposure duration. Furthermore, since no difference in ASR can be seen between the two pre-oxidized materials coated with 200 and 1500 nm Co, it can be concluded that the thickness of the Co_3O_4 layer can in principle be neglected, and thus the chromia scale thickness is the parameter responsible for the ASR, even at 650 °C.
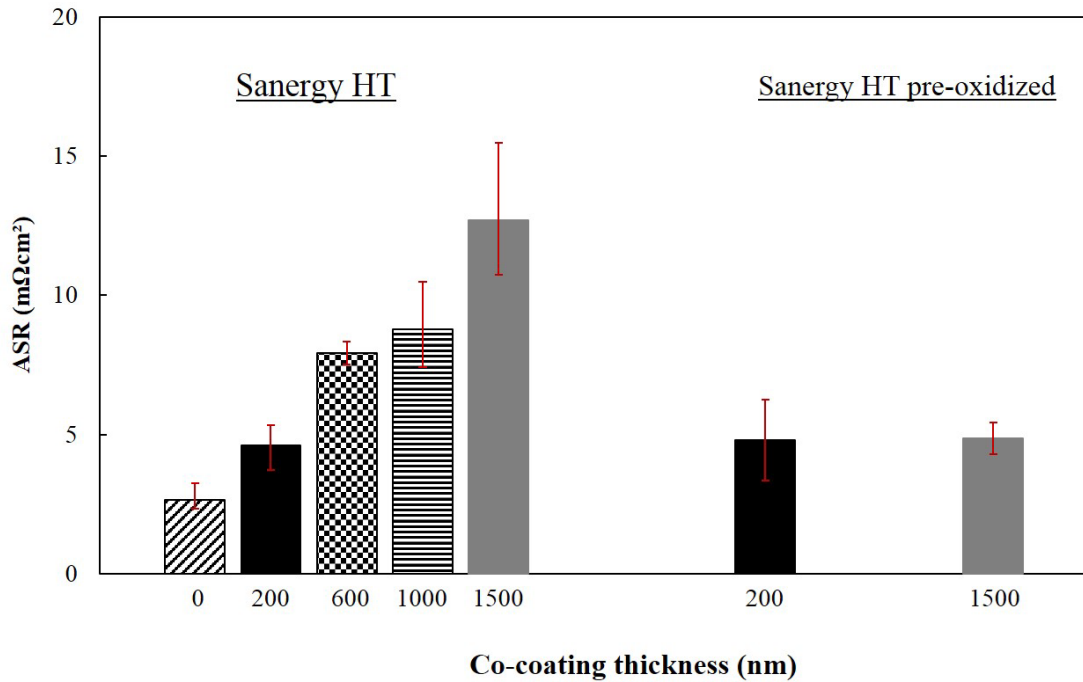
Figure 39: Area Specific Resistance (ASR) measured in air at 650 °C, as a function of Co-coating thickness after 168 h at 650 °C for Sanergy HT and pre-oxidized Sanergy HT.

Nevertheless, for all materials not being pre-oxidized before the coating was deposited on the steel, a layer of $(Co,Fe)_3O_4$ was formed. According to Petric and Ling [16] the electrical conductivity of $CoFe_2O_4$ is seven times lower than the electrical conductivity of Co_3O_4 in air at 800 °C. Whether a thicker $(Co,Fe)_3O_4$-layer may have a noticeable effect on the ASR or not could not be determined in this study, since a thicker $(Co,Fe)_3O_4$ layer is correlated with a thicker $(Cr,Fe)_2O_3$ scale. Nevertheless, for the 1500 nm Co-coated material the $(Co,Fe)_3O_4$ thickness is almost 3 μm after 168 h, but the ASR is only 10-15 $m\Omega cm^2$. It can therefore be assumed that this layer won't have a significant effect on the ASR. In fact, it is rather unexpected that the ASR for the 1500 nm Co-coated material is as low as 10-15 $m\Omega cm^2$ after 168 h at 650 ˚C, since the $(Cr,Fe)_2O_3$ scale on average is 1-2 μm thick (Figure 40). This is assumed to be correlated to the large variation in $(Cr,Fe)_2O_3$ scale thickness along the metal-oxide interface. Repeatedly along the metal-oxide interface, areas where the $(Cr,Fe)_2O_3$ scale is thinner than 1 μm can be observed after 168 h for the 1500 nm Co-coated material (Figure 40). These thinner areas may be the reason for the still relatively low electrical resistance. Linder et al. [111] have studied the increase in ASR caused by a growing chromia scale on metallic interconnects. They showed that typical morphologies favour nonhomogeneous electrical current distributions, where the main current flows over rather few "bridges", i.e. local spots with relatively thin oxide scales. With prolonged exposure time, however, the $(Cr,Fe)_2O_3$ layer on the 1500 nm Co-coated material in this work continued to grow thicker, and consequently the thickness of these "bridges" increased. This is assumed to be the main reason for the significant increase in ASR between 168 to 500 h (from ≤ 15 $m\Omega cm^2$ to ~40 $m\Omega cm^2$) for the 1500 nm Co-coated material.
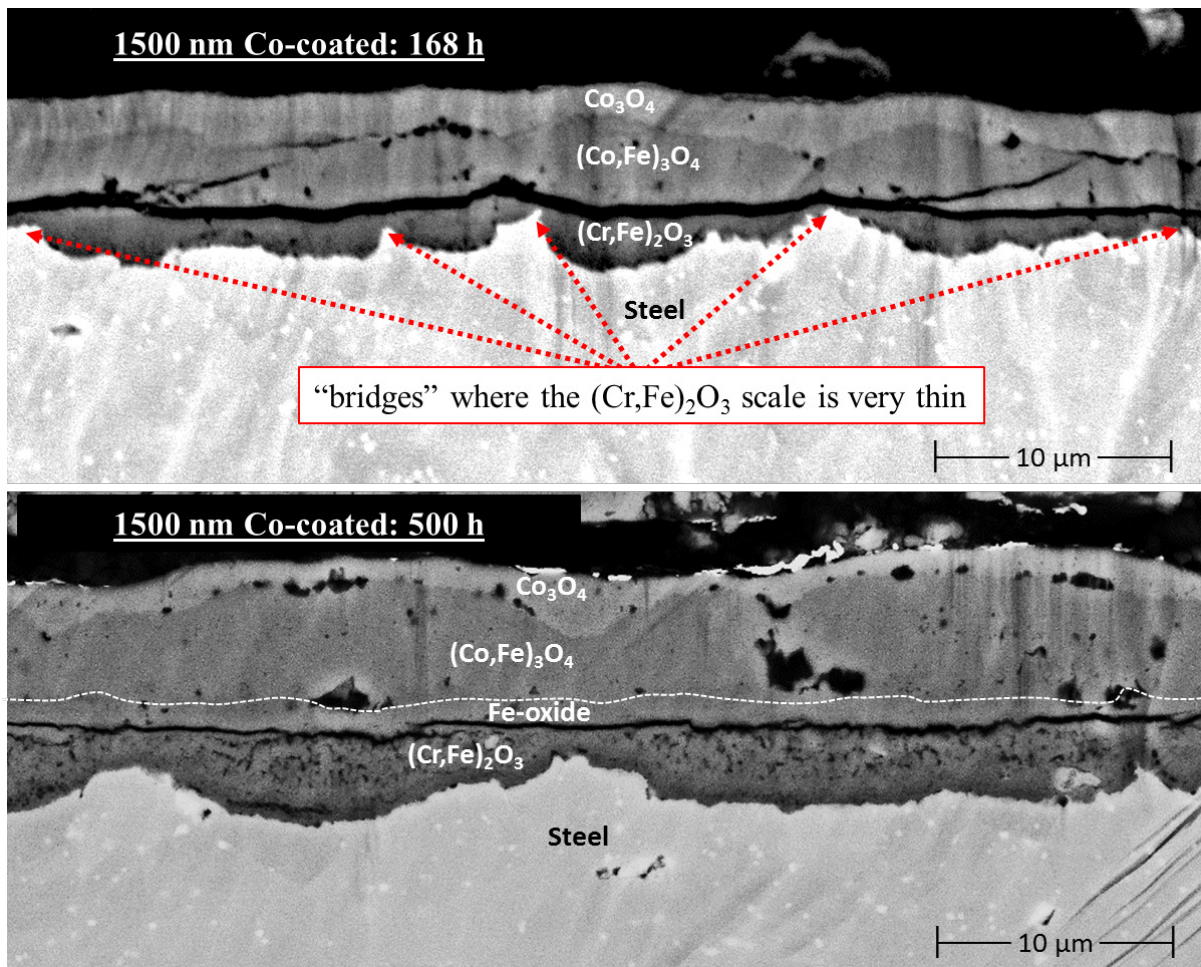
Figure 40: SEM images of Broad Ion Beam (BIB) milled cross-sections of Sanergy HT coated with 1500 nm Co after 168 h (upper image) and 500 h (lower image) at 650 ˚C in air.

5.3 Mechanical deformation of pre-coated interconnects

5.3.1 Self-healing mechanism of pre-coated and mechanically deformed steels

Development of coatings that mitigate Cr vaporization in order to eliminate cathode poisoning is crucial to prolonging the lifetime, and to increase the efficiency, of the SOFC. However, at the same time production costs have to be lowered in order to make the SOFC technology economically attractive. Coated interconnects are a component in the SOFC stack with the potential for significant cost reduction [117]. Today most coated interconnect materials are manufactured in two separate steps: (1) pressing the uncoated steel into an interconnect shape (to allow for gas distribution) and (2) coating the deformed steel plate (post-coating). Pre-coating large volumes of steel, which in a later stage are pressed into interconnects, would allow for much more efficient large scale production, and lower overall costs as a consequence. However, as the pre-coated steel is mechanically deformed, cracks within the coating may be formed.

Co-coated Crofer 22 APU:
Figure 41 shows the ferritic stainless steel Crofer 22 APU, pre-coated with 600 nm Co and then pressed into a real interconnect (Topsoe Fuel Cell design).
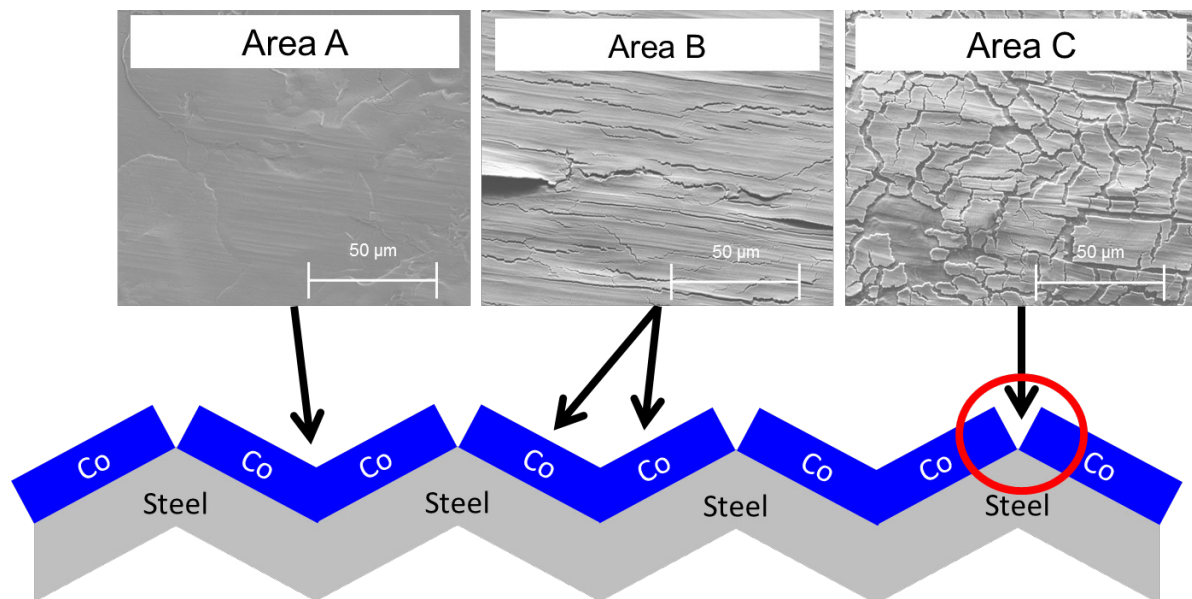
Figure 41. SEM images from different areas along the surface of the pre-coated material after being pressed into a real interconnect.

As the 600 nm Co-coated steel is pressed into a interconnect shape, cracks are formed. However, as Figure 41 shows, the extent of deformation largely varies over the interconnect surface. For instance, in Area C, where tensile straining took place, the surface if full of cracks, whereas on the opposite side of the interconnect (Area A), where the coating has been subjected to compressive stress, no cracks were formed. Since Area C is the area most affected by the mechanical deformation process, all images shown hereinafter will be from Area C. To investigate the effect of crack formation on high temperature oxidation and Cr vaporization the following four materials were studied: (1) uncoated and undeformed, (2) Co-coated and

undeformed, (3) deformed and subsequently Co-coated (post-coated) and (4) pre-coated with Co and then subsequently deformed. All Co-coated materials show similar mass gain behaviour (Figure 42). This indicates that there is no major effect on the oxidation resistance of the coated steel due to the mechanical deformation process (at least not during the first 336 h of exposure).
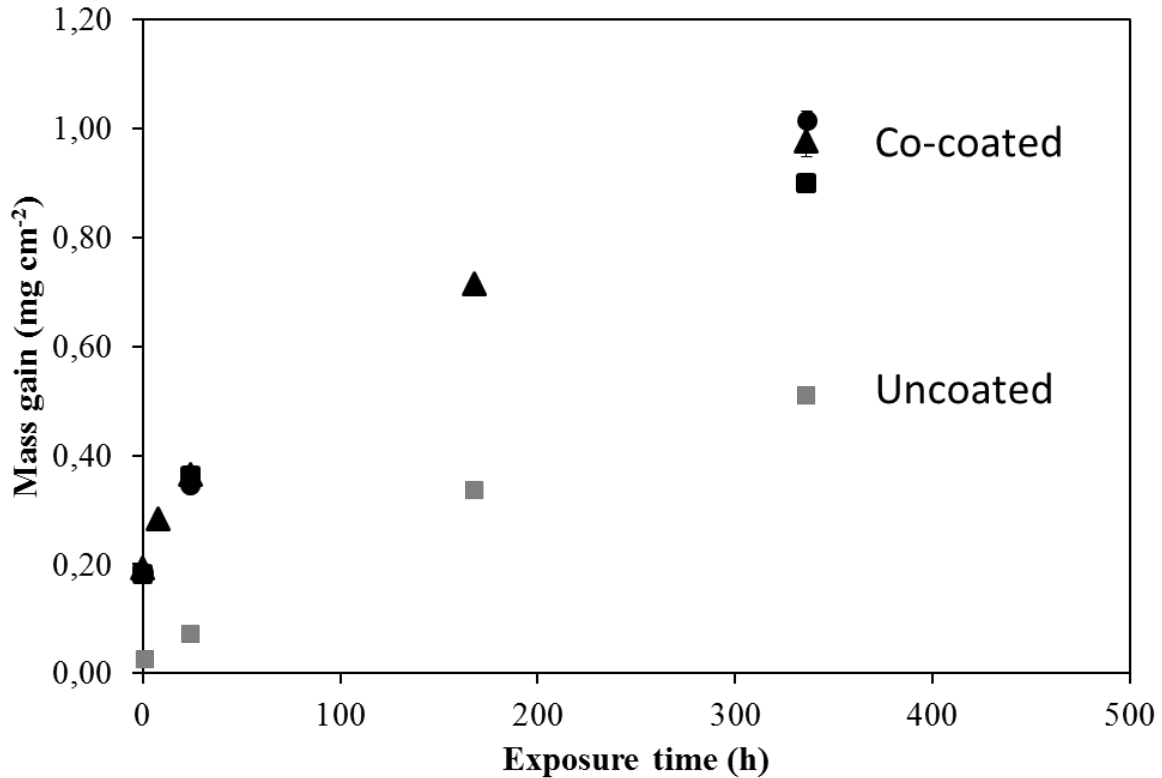
Figure 42: Mass gain as a function of time at 850 °C in air-3% H_2O (6000 sml min^{-1}). Uncoated undeformed (grey squares), coated undeformed (black squares), post-coated (black dots), and pre-coated (black triangles).

Cr vaporization is significantly reduced by coating the Crofer 22 APU steel with 600 nm Co (Figure 43). This is in agreement with earlier published data on Cr vaporization for ~600 nm Co-coated Sanergy HT and AISI 441 [27, 32]. The results also clearly show that pre-coating the steel and subsequently pressing it into the interconnect shape does not cause a noticeable increase in Cr vaporization, despite all the cracks formed within the Co-coating (Figure 43).
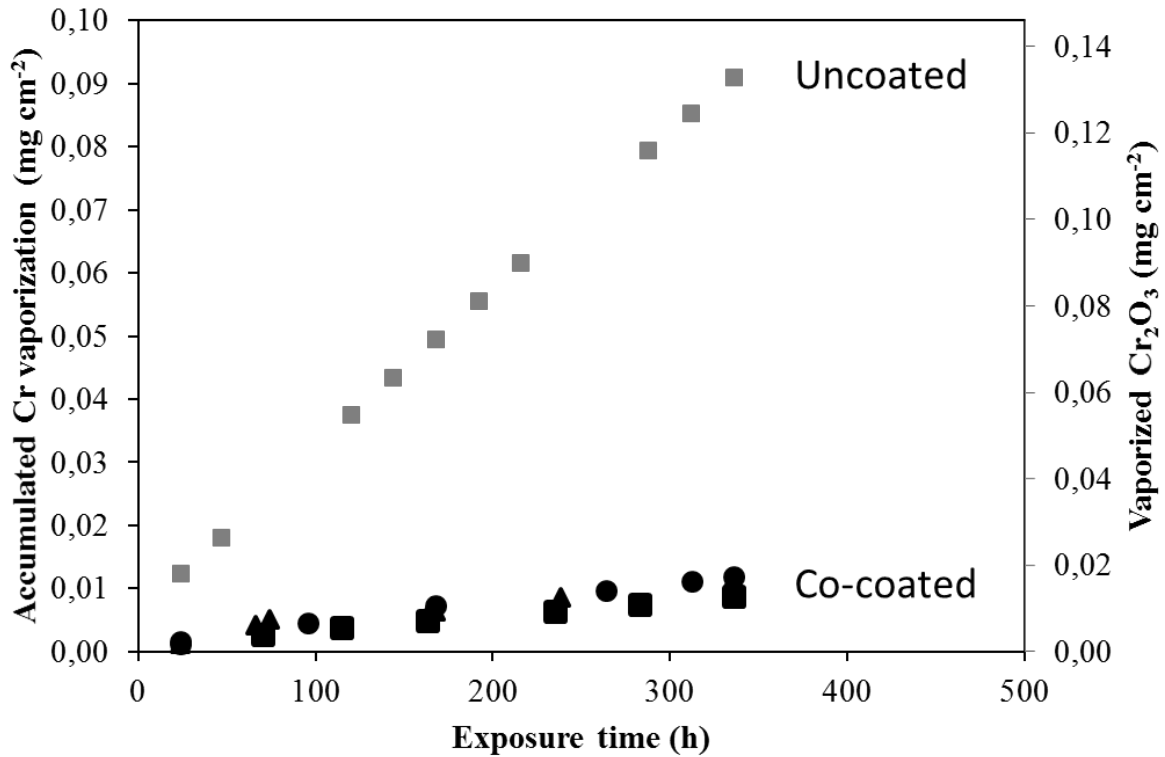
Figure 43: Accumulated Cr vaporization as a function of time at 850 °C in air-3% H_2O (6000 sml min^{-1}). Uncoated undeformed (grey squares), Coated undeformed (black squares), Post-coated (black dots), and Pre-coated (black triangles).

The reason there was no noticeable difference in Cr vaporization between the post and the pre-coated materials is that the cracks self-heal during exposure (Figure 44). During the initial oxidation phase Co is rapidly oxidized into Co-spinel. This takes less than 6 min at 850 °C [27] and is associated with a volume expansion (approximately twice the volume). This volume expansion may have closed some of the smaller cracks, however, most of the cracks remain after the Co-coating has been oxidized (see Figure 44 after 6 minutes).
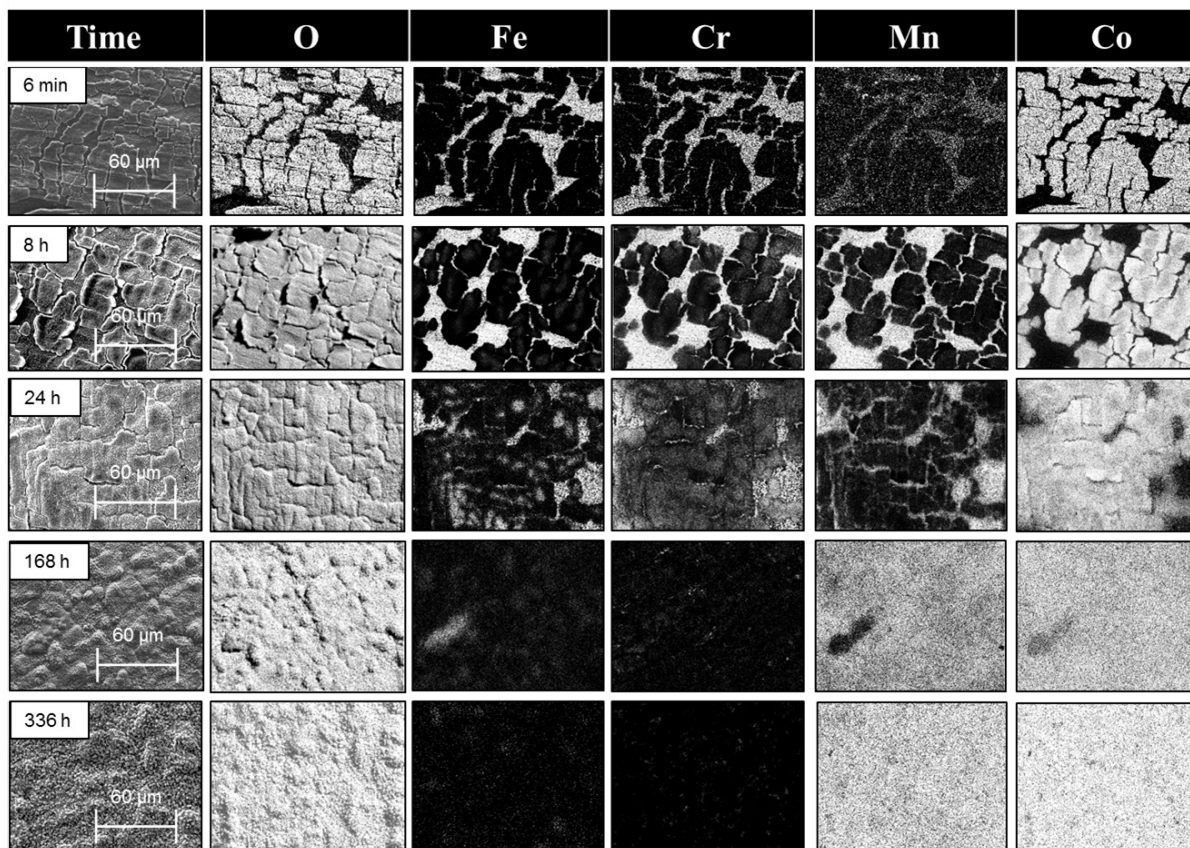
Figure 44: SEM top-view images and EDX elemental maps for the mechanically deformed Crofer 22 APU + 600 nm Co (pre-coated) after 0.1-336 h of exposure at 850 °C in air containing 3% H_2O (6000 sml min^{-1}).

After 8 h of exposure (Figure 44) the cracked areas are enriched in Mn, which suggests the formation of a $(Cr,Mn)_3O_4$ top-layer, as was observed by Sachitanand et al. [66] for uncoated Crofer APU exposed in the same environment. With prolonged exposure time (24 h) a more homogenously distributed Cr, Mn and Co EDX signal is observed. The cracked areas remain rich in Mn after 24 h, however, Co can partly be found within the cracked areas after 24 h. EDX mapping of a thin TEM-lamella from the sample exposed for 24 h (Figure 45) shows that the whole surface, including the cracked area, is covered with Co-oxide after only 24 h.

Figure 45: SEM image and EDX elemental maps of a thin lamella cut out by FIB milling from the mechanically deformed Crofer 22 APU + 600 nm Co (pre-coated) sample after 24 h of exposure at 850 °C in air containing 3% H_2O (6000 sml min^{-1}).

The fact that a large fraction of the surface within the cracked area is covered with a thin Co-rich oxide already after 24 h explains why no increase in Cr vaporization is observed. Taking a closer look into the cracked area, a clear difference in morphology between the Co-oxide within the cracked area and the rest of the Co-oxide can be observed. The Co-oxide in the non-cracked area is approximately 1-2 μm thick and contains large pores. The formation of rather large pores in thin metallic Co-coatings after oxidation of the Co-coating has also been observed earlier on non-deformed Co-coated materials [27]. In contrast, the Co-oxide within the cracked area did not contain pores and is enriched in Mn. The Co- and Mn-rich oxide within the cracked area consists of a very thin continuous layer and a few large cubic crystals. It is suggested that the thin continuous layer of Co-oxide in the cracked area was originally a thin $(Cr,Mn)_3O_4$ top-layer formed in the absence of a Co-coating. This thin $(Cr,Mn)_3O_4$-layer is then transformed into a $(Cr,Mn,Co)_3O_4$ top-layer with low Cr content by the interdiffusion and/or surface diffusion of Co from the oxidised Co-coating in the non-cracked area. The large cubic $(Co,Mn)_3O_4$-crystals, on the other hand, probably grew on the surface (within the cracked area) due to the diffusion of Co along the surface (by means of surface and/or solid state interdiffusion) and the outward diffusion of Mn from the steel. After prolonged exposure no signs of cracks can be seen. Instead the surface oxide is homogenously rich in both Co and Mn (Figures 44 and 46). It can therefore be concluded that the reason no noticeable increase in Cr vaporization is observed for the pre-coated material, despite the large amounts of cracks within the Co-coating, is due to the rapid diffusion of Co from the Co-oxide into the cracked area during exposure. A simplified schematic drawing describing the proposed self-healing mechanisms based on the findings from this study is shown in Figure 47.
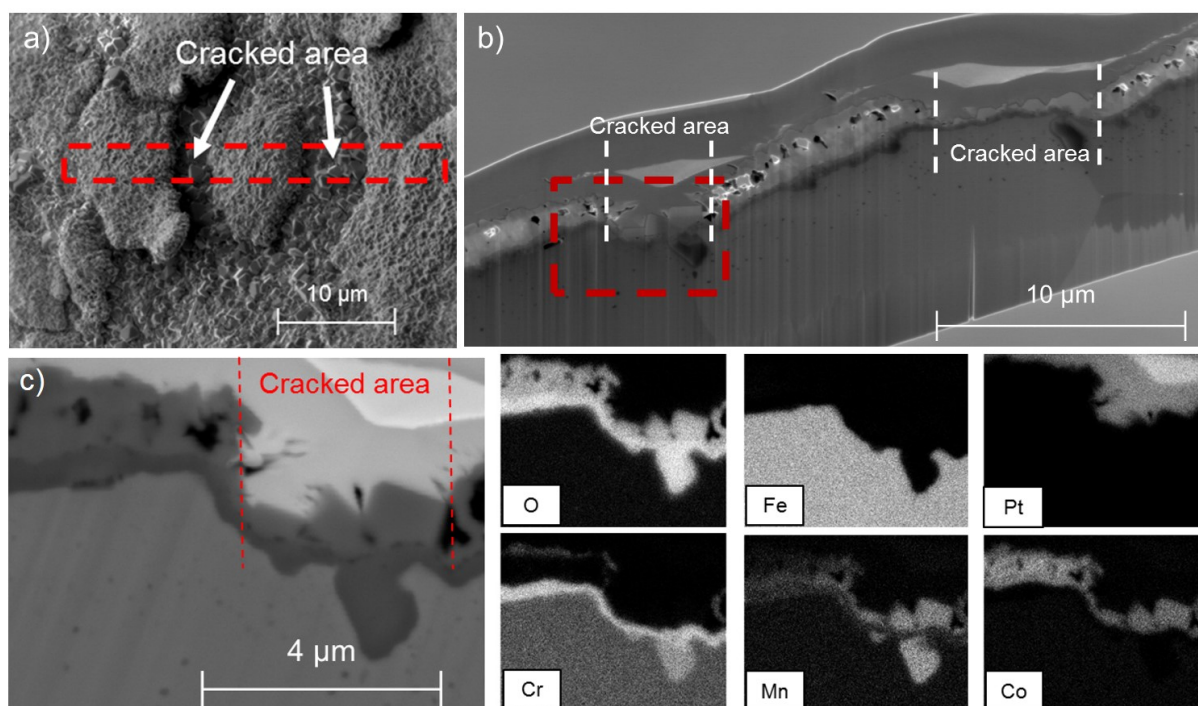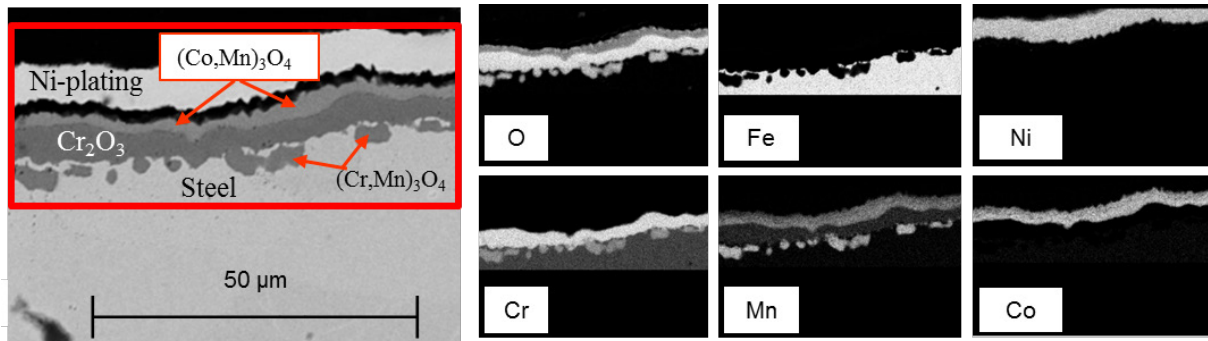
Figure 46: SEM image and EDX elemental maps of a cross section of the mechanically deformed Crofer 22 APU + 600 nm Co (pre-coated) sample after 336 h of exposure at 850 °C in air containing 3% H_2O (6000 sml min^{-1}).
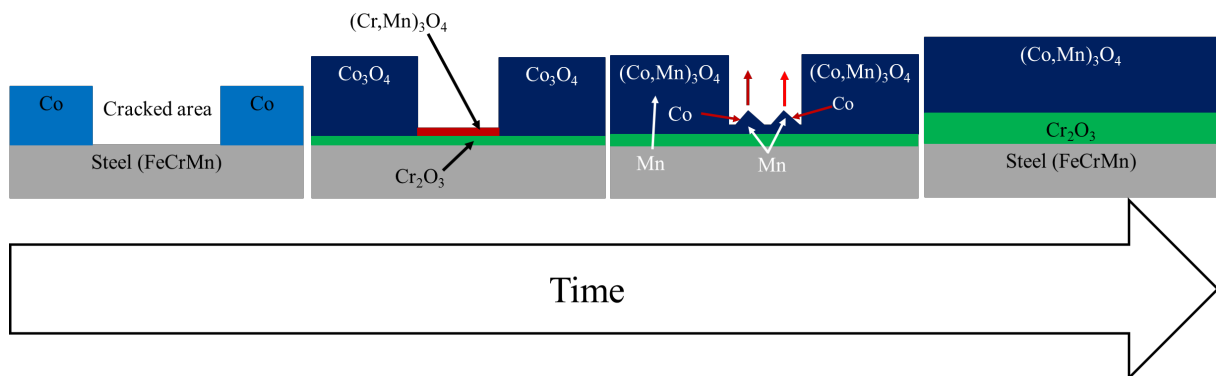
Figure 47: Simplified schematic drawing of the self-healing mechanism, based to the results from this section.

Ce/Co-coated Crofer 22 APU:

The beneficial effect of a 10 nm Ce-coating has already been discussed in Sections 3.3 and 5.2. A similar improvement in oxidation resistance is observed as a 10 nm Ce-layer is added to the 600 nm Co-coated Crofer 22 APU material (Figure 48a), as to Co-coated Sanergy HT and AISI 441 [26, 32, 81, 105]. Furthermore, the addition of a thin Ce-layer between the steel and the Co-coating does not affecting the self-healing ability of the Co-coating (Figure 48b).
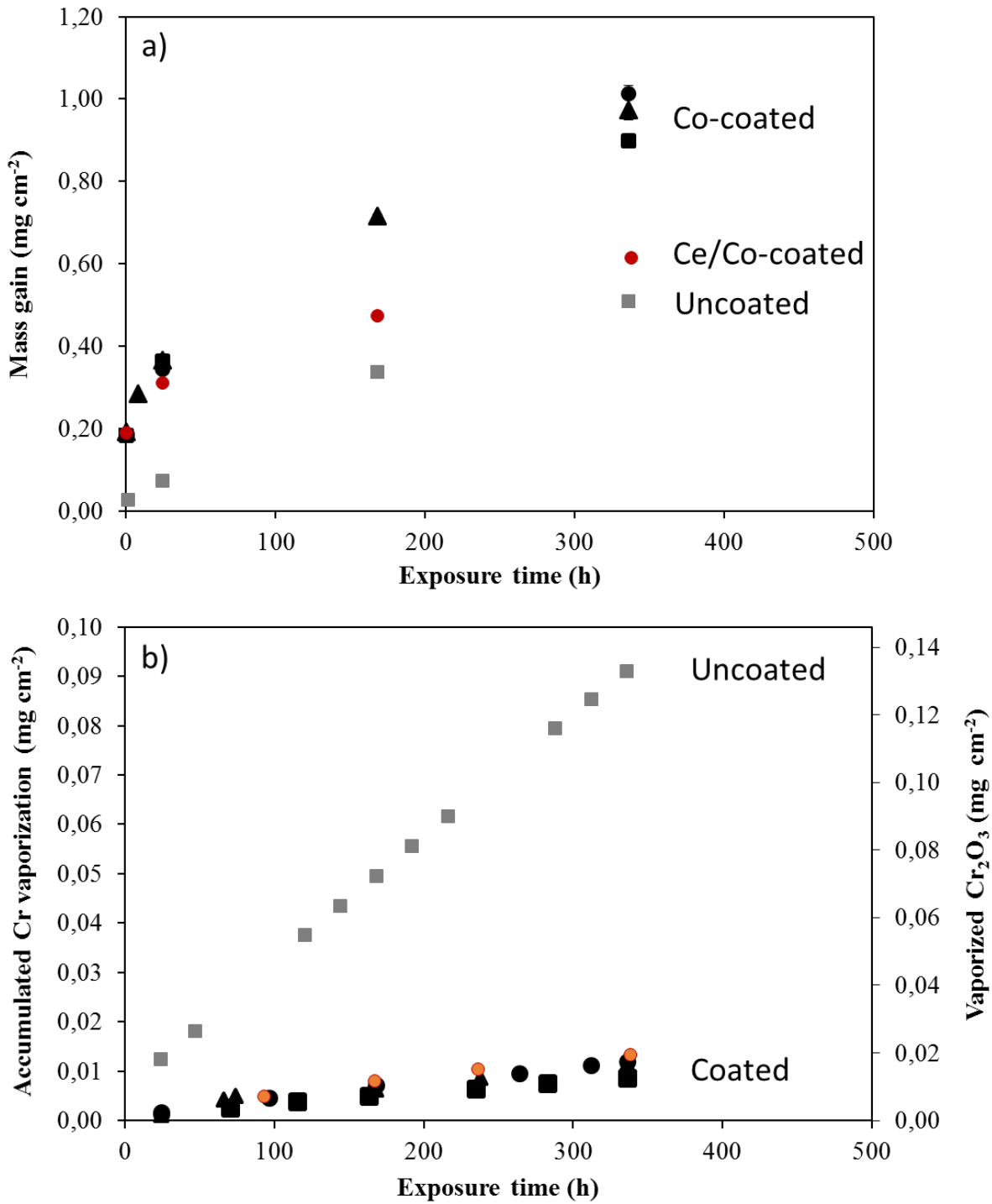
Figure 48: Mass gain (a) as a function of time at 850 °C in air-3% H_2O (6000 sml min^{-1}) shown in Figure 42 including the pre-coated Ce/Co-coated material (red dots). Uncoated undeformed (grey squares), coated undeformed (black squares), post-coated (black dots), and pre-coated (black triangles). In (b) Accumulated Cr vaporization as a function of time at 850 °C in air-3% H_2O (6000 sml min^{-1}) from Figure 43 is shown, including the Ce/Co-coated material (red dots).

5.3.2 The effect of deformation method

Ce/Co-coated AISI 441:

The shape of the interconnect is something that is unique for each SOFC manufacturer. In order to be able to study the possibility of the coated interconnect to heal upon exposure, independently of the manufacturers specific interconnect design, the effect of the deformation method was studied in this work. The ferritic stainless steel AISI 441 was coated with Ce and Co, and the pre-coated steels were then mechanically deformed by uniaxial and biaxial tensile straining and by pressing the pre-coated material into real interconnects. As references, coated but not mechanically deformed, as well as the uncoated steel, were studied. The same interconnect shape was utilized for this study as in Section 5.3.1. (Topsoe design). Table 2 shows the five different materials investigated.

Table 2. Materials investigated. The materials that were subjected to uniaxial and biaxial tensile straining were strained until rupture, which for this material was 30% for uniaxial and 13% for biaxial tensile straining.

	Substrate	Coating	Deformation
Uncoated	AISI 441		Interconnect shape
Ce/Co Flat	AISI 441	30 nm Ce + 600 nm Co	
Ce/Co IC	AISI 441	30 nm Ce + 600 nm Co	Interconnect shape
Ce/Co Biax	AISI 441	30 nm Ce + 600 nm Co	13% Biaxial
Ce/Co Uniax	AISI 441	30 nm Ce + 600 nm Co	30% Uniaxial

All mechanical deformation methods induced large cracks within the Ce/Co-coating (Figure 49). Differences in size and shape of the cracks can be seen, however, for the different deformation methods. The largest cracks were formed in the material that was pressed into a real interconnect. Nevertheless, the image in Figure 49, showing the material pressed into a real interconnect, only corresponds to the area that is most severely affected by the deformation (Area C in Figure 41) and is therefore not representative for the entire surface of the sample. Straining the coated material biaxially created cracks along two axes, similar to the cracks seen in Area C (see Figures 41 and 49) for the pre-coated material pressed into an interconnect. By straining the coated material uniaxially, cracks along only one axis are observed, similar to Area B in Figure 41. In contrast to the images for the material pressed into a real interconnect, the images for the biaxially and uniaxially strained materials represent the whole sample surface.
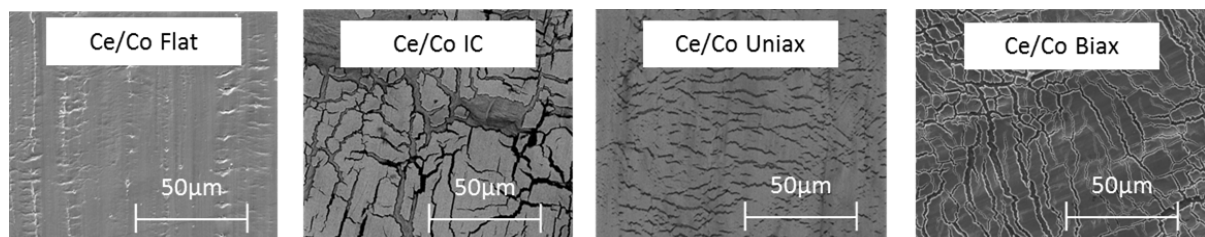
Figure 49: SEM images of the four Ce/Co-coated materials before exposure.

The observed difference in size, direction and amount of cracks, as an effect of different deformation methods, did not however have an effect on Cr vaporization (Figure 50). All 4 coated materials substantially lowered the amount of vaporized Cr compared to the uncoated material. As is the case for the Co- and Ce/Co-coated Crofer 22 APU materials (Section 5.3.1), the Ce/Co-coating on the ASIS 441 steel is able to heal upon exposure. It can therefore be concluded that more generic deformation methods, such as uniaxial and biaxial tensile straining, can be used to study the ability of the coating to heal upon exposure. Furthermore, this work also proves that the ability of thin Co- and Ce/Co-coatings to heal upon exposure is not limited to the Crofer 22 APU substrate material.
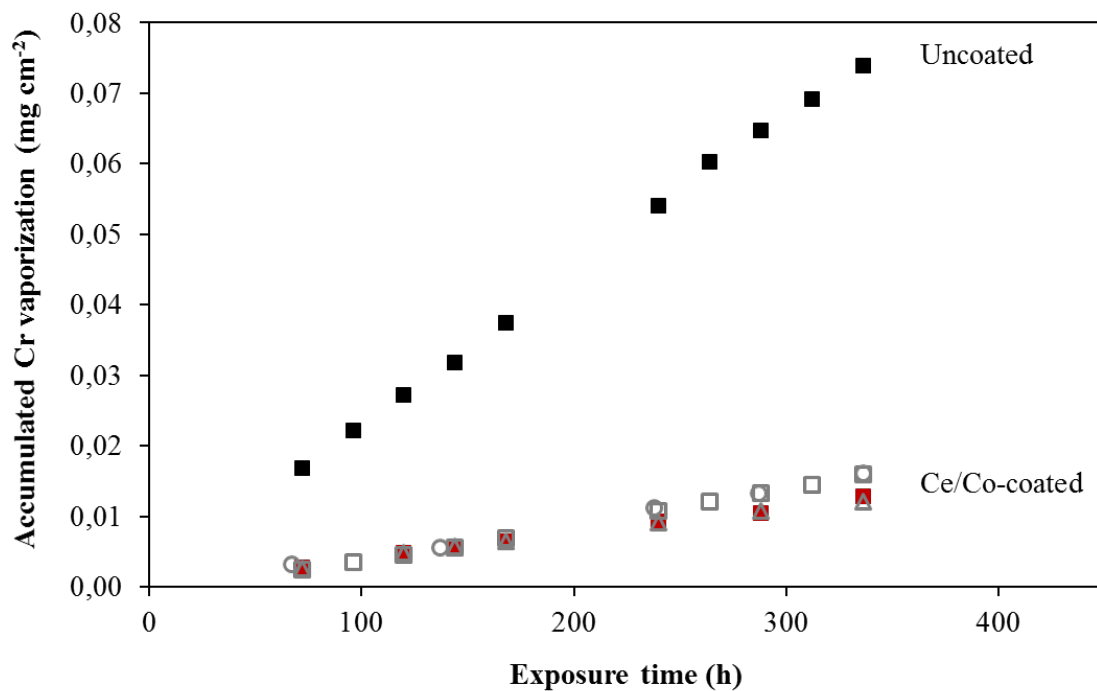
Figure 50: Accumulated Cr vaporization as a function of time at 850 °C in air-3% H_2O (6000 sml min^{-1}). Uncoated (black squares), Coated undeformed (red squares), pre-coated and pressed into a real interconnect (grey squares), pre-coated and uniaxially strained (grey triangles), and pre-coated and biaxially strained (grey circles).

5.4 Determining oxide scale growth mechanism by the use of ^{18}O-tracer experiments

Two-stage, ^{18}O$_2$ and ^{16}O$_2$, experiments, in combination with analytical methods such as Secondary Ion Mass Spectrometry (SIMS), have been used for decades in high temperature corrosion studies, with the aim to investigate the effect that alloying elements, secondary phases, surface treatments, and coatings have on the growth mechanism of thermally grown oxide scales [33, 69, 77, 118]. Traditionally, in two-stage $^{18/16}$O$_2$-tracer experiments, one would use SIMS depth profiling to study the oxide growth mechanism. However, SIMS depth profiling results are not entirely unambiguous due to the limited lateral resolution, often in the micron range or in best cases a few hundreds of nanometres. Rough surface topography and thickness variation of the oxide scale over the analysed volume adds to the ambiguity of the results. The aim of this work has therefore been to develop a method eliminating these obstacles associated with conventional SIMS sputter depth profiles.

5.4.1 SIMS-sputter depth profiles versus nanoSIMS mapping

A model alloy consisting of Fe and 20wt% Cr was exposed for a total time of 168 h at 850 °C. During the first 48 h (1st stage) the sample was exposed in an ^{18}O-rich environment (Ar-20% ^{18}O$_2$ containing ~1% H$_2$^{18}O). After 48 h in the ^{18}O-rich environment the exposure atmosphere was switched, and during the remaining 120 h (2nd stage) the sample was exposed in a ^{16}O-rich environment (Ar-20% ^{16}O$_2$ containing ~1% H$_2$^{16}O). For a more detailed description of the setup and experiment, see Paper VII. After the 168 h two-stage exposure, a chromia scale with a thickness of 1-2 μm had been formed on the surface of the model alloy (Figure 51).
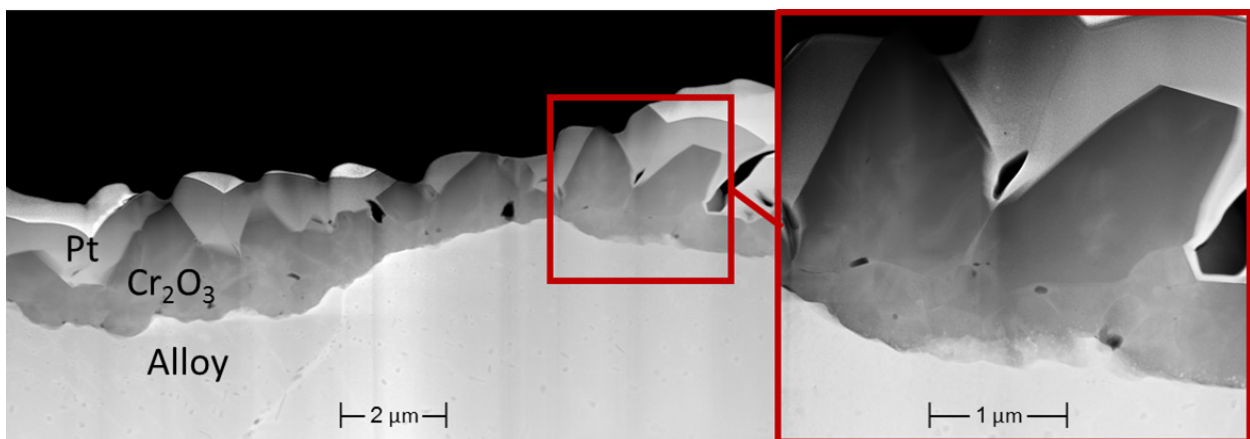
Figure 51: STEM image of the Cr$_2$O$_3$ scale formed on the Fe20Cr alloy after 168 h (48 h in Ar-20% ^{18}O$_2$ containing ~1% H$_2$^{18}O + 120 h in Ar-20% ^{16}O$_2$ containing ~1% H$_2$^{16}O) at 850 °C.

At the metal-oxide interface the grain size is very fine, whereas the grains formed at the gas-oxide interface are significantly larger (up to 1 μm in size).

From the TOF-SIMS sputter depth profiles (Figure 52) it can be seen that the oxide scale formed during the second stage (^{16}O) is located at the surface of the chromia scale and is levelling off towards the metal-oxide interface. This type of curve could be associated with inward lattice diffusion by means of oxygen ions [119]. However, since no clear border between the steel and

the oxide scale is observed (see total oxygen signal), the decrease in ^{16}O concentration towards the metal-oxide interface is an artefact caused by the large variation in oxide scale thickness. Moreover, the maximum concentration of ^{18}O (the oxide from stage 1) is at the same depth as where the total oxygen signal is starting to level off, which indicates that the oxide formed during the first stage (^{18}O) has its maximum concentration near the metal-oxide interface. With these considerations, the results from the TOF-SIMS sputter depth profile suggest that the oxide formed during the second stage (48-168 h) is formed at the gas-oxide interface, and thus the dominating mechanisms for chromia scale growth on the Fe20Cr model alloy, between 48 and 168 h, is by means of outward chromium diffusion.

Figure 52: TOF-SIMS depth profiles of the Fe20Cr model alloy exposed for 168 h (48 h in Ar-20% $^{18}O_2$ containing ~1% $H_2^{18}O$ + 120 h in Ar-20% $^{16}O_2$ containing ~1% $H_2^{16}O$) at 850 °C.

The purpose of this study, however, was to eliminate issues such as rough surface topography and variations in oxide scale thickness. This was successfully done by mapping ^{16}O and ^{18}O on the TEM lamella, utilizing nanoSIMS, which has a spatial resolution of approx. 50 nm (see Figure 53).

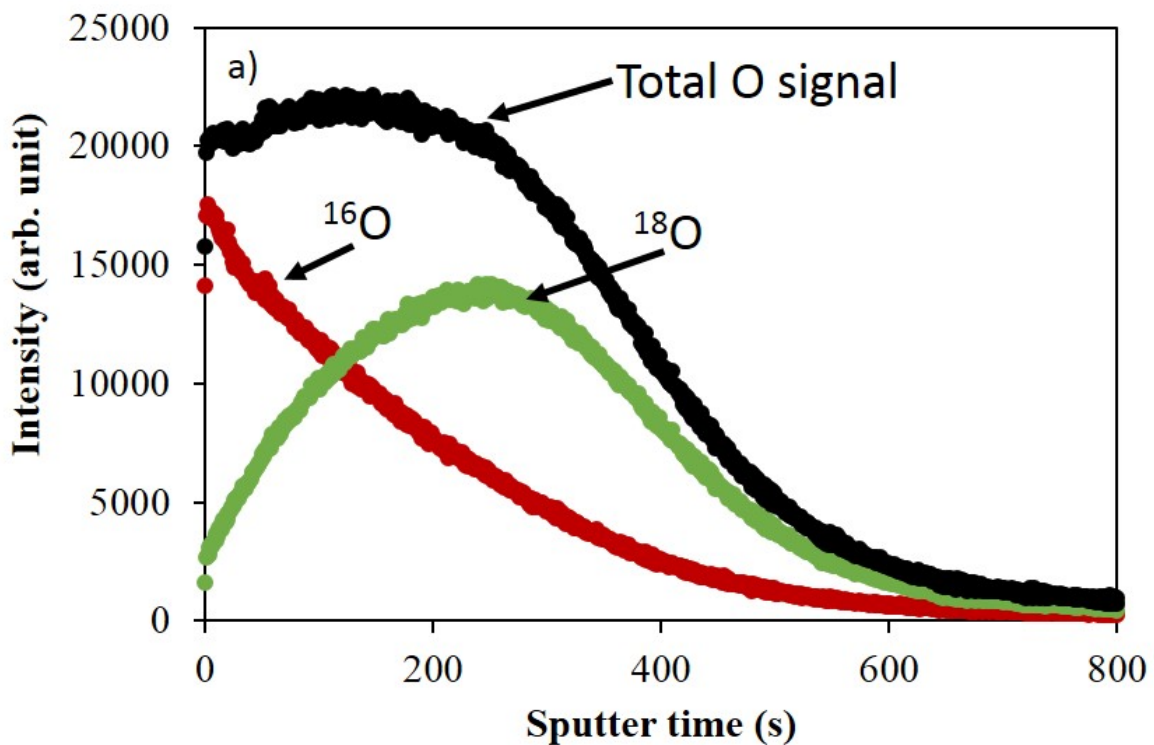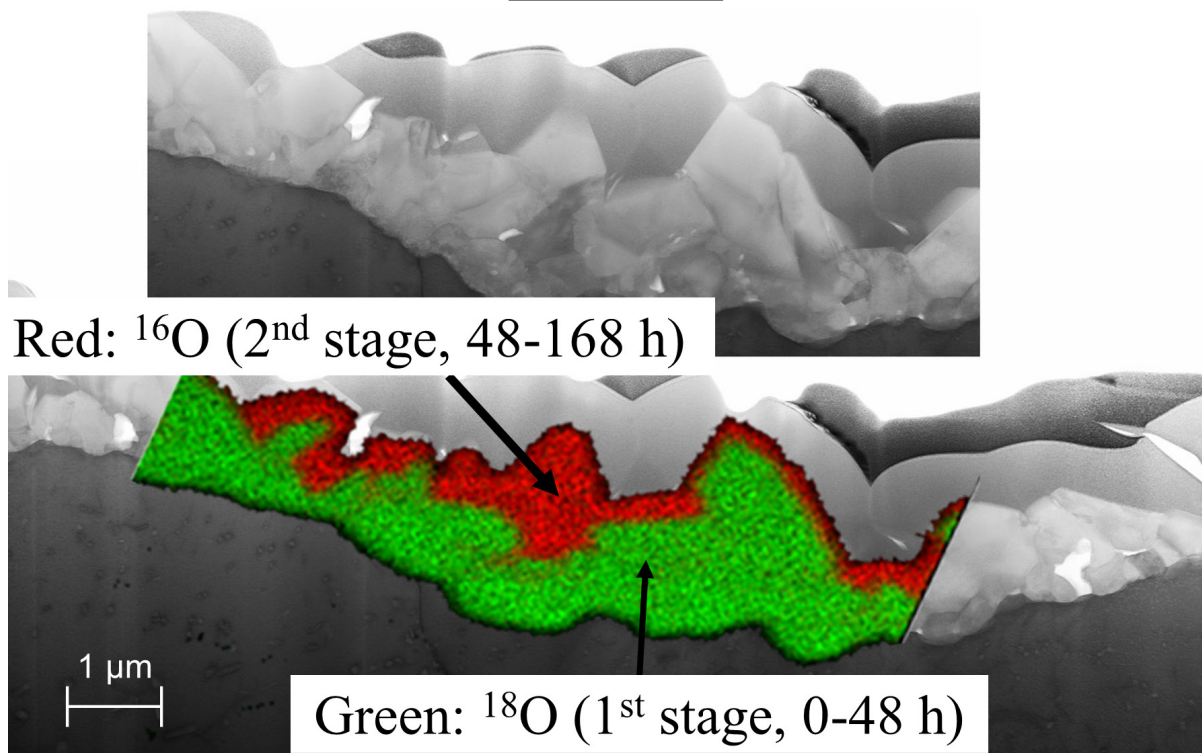**Figure 53:** ^{16}O and ^{18}O nanoSIMS maps from the TEM lamella shown in Figure 51 that was prepared from the Fe20Cr model alloy exposed for 168 h (48 h in Ar-20% $^{18}O_2$ containing ~1% $H_2^{18}O$ + 120 h in Ar-20% $^{16}O_2$ containing ~1% $H_2^{16}O$) at 850 °C.

By comparing the TOF-SIMS sputter depth profiles (Figure 52) with the nanoSIMS maps (Figure 53), it can be concluded that substantially more information can be gained from the nanoSIMS maps. From the ^{16}O and ^{18}O maps it can clearly be seen that the oxide scale, formed during the second stage (^{16}O) is formed at the gas-oxide interface, whereas the oxide, formed during the first stage (^{18}O) is located beneath. Furthermore, a clear border between the oxide layers formed during stage 1 and stage 2 can be seen (very little interdiffusion, see line scans in Paper VII; Figure 6). The ^{16}O and ^{18}O maps also show that the oxide formed during the second stage (^{16}O) is growing preferentially in certain areas. In some areas of the oxide scale, almost no increase in oxide scale thickness took place during the 120 h that the sample was exposed to a ^{16}O-rich atmosphere (2nd stage), whereas in other areas, large ^{16}O-rich grains formed during the same time interval. Such strong local variation of oxide scale growth (individual grains grow differently) is not possible to see in the TOF-SIMS sputter depth profiles and would actually contribute to an even larger $^{16}O/^{18}O$ overlap. From these results it can be concluded that when preparing a cross-section (in this study it was a TEM lamella) of the exposed sample, and then mapping the area with high resolution nanoSIMS, much more detailed and reliable data can be provided.

Ce-coated Fe-20Cr Alloy:
In sections 5.2 and 5.3 it was shown that the addition of a 10 nm Ce-coating between the steel and the Co-coating substantially improved the oxidation resistance of the ferritic stainless steels investigated at 650-850 °C. In order to gain further knowledge regarding the superior oxidation

resistance of the materials coated with Ce, the Fe20Cr model alloy was coated with 10 nm Ce (after the surface had been ground and polished). Both the uncoated sample and the Ce-coated sample were exposed simultaneously in the two-stage exposure that was previously described. After 168 h at 850 °C no obvious difference in thickness of the thermally grown chromia scales can be observed between the uncoated and the Ce-coated samples (Figure 54). A second exposure, where the two materials were exposed for 500 h, did however indicate that the Ce-coating has a beneficial effect on the oxidation resistance, also for the model alloy. After 500 h the mass gain was lower for the Ce-coated material than for the uncoated material. Moreover, parts of the oxide scale had spalled off from the uncoated material, whereas no signs of oxide scale spallation could be seen on the Ce-coated sample. TEM and nanoSIMS on these samples are planned to be carried out in the future, however, at the moment only mass gains and visual inspection are available from these 500 h samples.
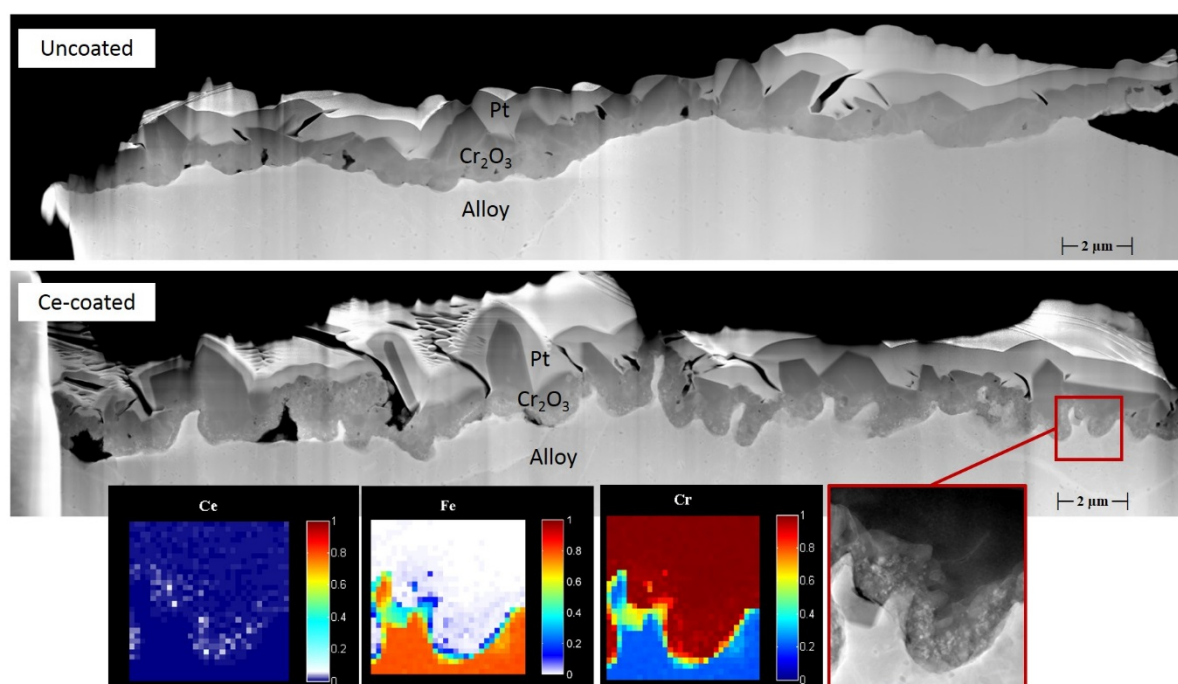
Figure 54: STEM images of the oxide scales formed on the uncoated and the 10 nm Ce-coated Fe20Cr alloy after 168 h (48 h in Ar-20% $^{18}O_2$ containing ~1% $H_2^{18}O$ + 120 h in Ar-20% $^{16}O_2$ containing ~1% $H_2^{16}O$) at 850 °C. For the Ce-coated sample EELS analyses were performed in order locate the Ce (see Ce, Fe, and Cr elemental maps in the selected area).

Nevertheless, when comparing the microstructure of the oxide scales formed after 168 h, a rather clear difference in microstructure can be seen between the uncoated and the Ce-coated material after 168 h. For the uncoated sample a smooth metal-oxide interface can be seen. This is not the case for the Ce-coated sample, where it can instead be seen that the metal-oxide interface is rather rough. The rougher metal-oxide interface for the Ce-coated sample would explain the better scale adhesion for the coated sample, and thus why no signs of oxide scale spallation were seen on the Ce-coated sample after 500 h, whereas parts of the oxide scale indeed did spall off from the uncoated sample after 500 h. Furthermore, at the surface of the

oxide scale even more localized crystal growth seems to have taken place on the Ce-coated material compared to the uncoated material.

In fact the ^{16}O and ^{18}O nanoSIMS maps indicate that even more localised oxide scale growth took place for the Ce-coated sample (Figure 56). In certain areas apparently no new oxide (^{16}O) had been formed during the second exposure stage (48-168 h). Another difference between the uncoated and the Ce-coated sample is that for the Ce-coated sample some areas at the metal-oxide interface are rich in ^{16}O (2nd stage), indicating that some of the oxide, formed during the second stage, was formed by means of oxygen inward diffusion. Nevertheless, the great majority of the oxide, formed during the second stage, was formed at the gas-oxide interface, and not at the metal-oxide interface, which indicates that also the thermally grown chromia scale that grew on the Ce-coated sample predominantly grows by means of outward chromium diffusion. From these results a change in growth direction, from predominantly outwards growth by means of chromium ions, to predominantly inwards growth by means of oxygen ions, as an effect of the Ce-coating, cannot be concluded. At least not during the studied time interval.

10 nm Ce-coated

Red: ^{16}O (2nd stage, 48-168 h)

1 µm

Green: ^{18}O (1st stage, 0-48 h)
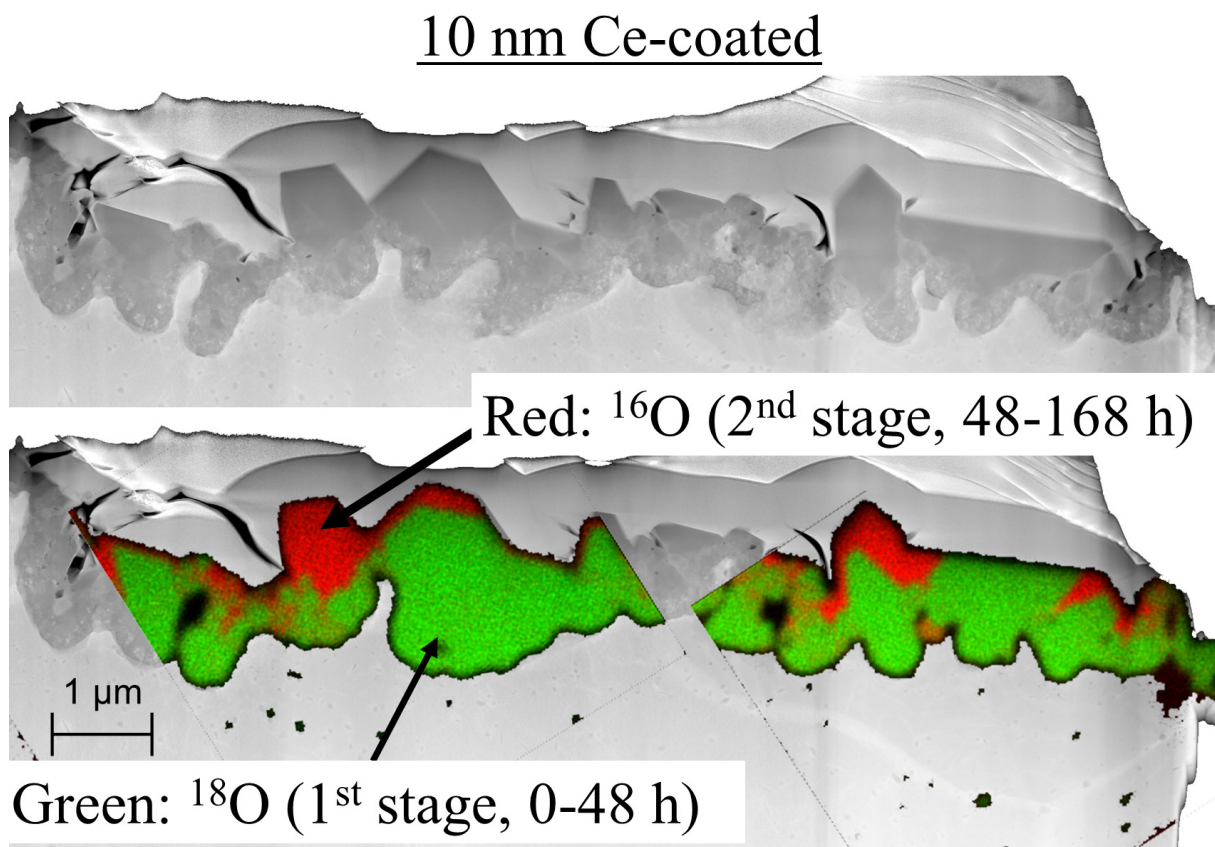
Figure 55: ^{16}O and ^{18}O nanoSIMS maps from the TEM lamella shown in Figure 54 that was prepared from the Ce-coated Fe20Cr model alloy exposed for 168 h (48 h in Ar-20% $^{18}O_2$ containing ~1% $H_2^{18}O$ + 120 h in Ar-20% $^{16}O_2$ containing ~1% $H_2^{16}O$) at 850 °C.

Moreover, further proof for the assumption that most of the oxide scale did grow by means of chromium outwards diffusion is the EELS analysis in Figure 54, where it can be seen that Ce is located near the metal-oxide interface. In Section 5.2.2 it was argued that Ce can't be used as inert markers in order to prove that the oxide scale is growing predominantly by means of oxygen inward diffusion [30]. Ce is, however, not expected to migrate towards the metal. The fact that Ce is located near the metal-oxide interface therefore supports the nanoSIMS results in Figure 56 showing that the oxide scale was primarily growing by means of outward chromium diffusion during the 2nd stage of the exposure. These results contradict the two-stage work by Papaiacovou et al. [118] where a change in the Cr_2O_3-scale growth mechanism, from cation to predominantly anion diffusion was reported, as an effect of a 4 nm CeO_2-coating on a Fe20Cr alloy at 900 °C. The cause for the controversy between the study by Papaiacovou et al. [118], and the results presented in this work might be correlated to differences in temperature, atmosphere and materials investigated. It is therefore crucial to conduct more research in this field. What is clear from both the study by Papaiacovou et al. [118] and the results in this thesis, is that a thin layer of Ce-oxide substantially improves the oxidation resistance of Cr_2O_3-formation alloys.

6. Summary

In this thesis uncoated, Co-, and Ce/Co- thin-film coated ferritic stainless steels were studied in a cathode simulated environment with the focus on the two degradation mechanisms, oxide scale growth and Cr (VI) species volatilization, which are associated with the use of ferritic stainless steels as interconnect material in SOFCs. In particular the effect of temperature in the technologically relevant temperature range (650-850 °C) was studied with focus on Cr vaporization, oxide scale growth, microstructural and chemical evolution of the oxide scales, as well as the effect these factors have on the electrical resistance of the oxide scale. The Cr vaporization measurements showed that volatilization of Cr(VI) species has a weak temperature dependency, and thus substantial amounts of Cr are volatilized even at 650 °C. In order to guarantee stable long-term performance, high quality coatings that mitigate Cr volatilization are recommended, even in the 600-700 °C temperature range. By coating the steel with thin-film metallic Co- and Ce/Co-coatings, Cr vaporization is effectively mitigated for more than 3000 h at 650-850 °C. Oxide scale growth, on the other hand, is strongly influenced by temperature (three times higher activation energy compared to Cr vaporization). For this reason, a significant reduction in chromia scale thickness was observed as an effect of decreased temperature. Also the oxidized Co-coating was affected by a temperature decrease. As the metallic Co-coating is heated in air, the metallic Co-layer is converted into a dual layered oxide consisting of a Co_3O_4 top-layer and a $(Co,Fe)_3O_4$-layer underneath. The formation of the $(Co,Fe)_3O_4$-layer can be prevented by the presence of a Ce-coating between the steel and the metallic Co-coating, or by pre-oxidising the steel before deposition the Co-coating. With prolonged exposure time, at 750 and 850 °C, Mn from the steel is diffusing out into the Co-spinel layer(s) and thus transforming the oxidized Co-coating into a highly conductive $(Co,Mn)_3O_4$ top-layer. Furthermore, at 750 and 850 °C the two Co-spinel layers, Co_3O_4 and $(Co,Fe)_3O_4$, are also homogenised with prolonged exposure time. At 650 °C, in contrast, almost no Mn had diffused out into the Co-spinel after 3300 h, and the dual layered Co-oxide (Co_3O_4 and $(Co,Fe)_3O_4$) could still be observed. The change in chemical composition of the Co-spinel did not however affect the ASR. It was shown that the contribution of the Co-spinel to the total ASR can be neglected, since the electrical conductivity of chromia is substantially lower than that of all the relevant Co-spinels formed as top-layers at 650-850 °C. Moreover, despite the semiconductive properties of the oxide scale, a decrease in temperature had a beneficial effect on the ASR. The reason for this is the much higher activation energy for oxide scale growth compared to the activation energy for electrical conduction in chromia. Nevertheless, to ensure a low ASR at 600-700 °C it is advised to use coating methods that do not require an additional heat treatment in order to densify the deposited coating, since such a heat treatment may lead to thick chromia scales. Furthermore, as long as the metallic Co-coating is thin, a low ASR can be expected at 650 °C. However, if the metallic Co-coating exceeds 1 μm the formation of a thick Cr- and Fe-rich oxide scale during the initial oxidation phase may lead to a high ASR at 650 °C. The formation of a thick Cr- and Fe-rich oxide scale during the initial oxidation phase is associated with the metal-metal contact between the steel and the Co-coating, and can be avoided by the application of a blocking layer (e.g. pre-oxidation or a Ce-coating) between the steel and the metallic Co-coating. In this work it was shown that a layer of Ce clearly improved the oxidation resistance at all studied temperatures (650-850 °C). At 750 and 850 °C the improved oxidation resistance was mainly attributed to the reactive element effect, whereas the

main benefit of a Ce-coating at 650 °C is as a blocking layer, separating the metallic Co-coating from the steel substrate.

Moreover, to reduce the costs of coated interconnects it is important to choose a coating method that allows for high volume production. Thin-film metallic Co- and Ce/Co-coatings can be applied in a roll-to-roll process using physical vapour deposition. The pre-coated steel coil can then be pressed into thousands of coated interconnects, which would allow for efficient large-scale production and lower overall costs. However, as the thin-film pre-coated Co- and Ce/Co-coated steels are pressed into the interconnect shape, large cracks were formed within the coating. However, the results showed that these cracks can heal upon exposure and form a continuous surface oxide rich in Co and Mn. As an effect of the rapid healing, no increase in Cr vaporization was measured for the pre-coated and mechanically deformed materials compared to the undeformed coated reference materials.

Furthermore, in this work a two-stage $^{18/16}$O-tracer exposure setup was used, and a new method to analyse the $^{18/16}$O-tracer experiments was developed. By mapping ^{18}O and ^{16}O on a cross-section of the oxide scale using high resolution nanoSIMS much more detailed and reliable information could be achieved compared to conventional SIMS sputter depth profiles. The results from the two-stage exposures at 850 °C showed that the dominating growth mechanism for chromia scale growth was by means of chromium outwards diffusion, both for the uncoated and the Ce-coated Fe-20Cr alloy.

7. Outlook

Although many of the original questions have been answered in this thesis, each answer always leads to new questions. All exposures in this thesis have been carried out under oxidising conditions (cathode atmosphere), and both sides of the sample coupons have been exposed in the same environment. In an SOFC stack, one side of the interconnect material is exposed to the cathode side, whereas the other side is exposed to the anode (fuel) side (dual atmosphere). Within the last decade several studies have been published showing that exposure under dual atmosphere conditions can lead to increased corrosion at the cathode side. It would therefore be both relevant and highly interesting to investigate the effect of dual atmosphere conditions on these Co- and Ce/Co-coated materials (Co-coating only on the cathode side). Another topic that is relevant in order to gain knowledge with respect to real SOFC conditions is the effect of the electrode material. In this work, platinum was used as electrode material. The aim with the ASR measurements was to measure the electrical resistance of the oxide scale, and not the cathode-interconnect interaction. As a second step the interaction between the oxidized Co-coating and actual cathode material, such as LSM and LSCF, would be of great interest and should be carried out in a future study. Furthermore, in this work Co- and Ce/Co-coated ferritic stainless steels were investigated on a component level. Due to the complexity of real SOFC stacks, such tests are, and will always be, of great importance. As a comparison it would be interesting to conduct real stack tests, and compare the results from these tests with the component level exposures from this thesis.

Finally, the results in in this thesis have shown that the addition of a thin Ce-layer between the steel substrate and the Co-coating substantially improves the oxidation resistance at 650-850 °C. The exact mechanisms behind the improved oxidation resistance with reactive elements are still under debate, and much research is still lacking regarding the Ce/Co-coatings. This is a very interesting field that needs to be further explored. Dedicated TEM/EELS analysis needs to be carried out in order to locate the Ce (is Ce present in the chromia grain boundaries or is Ce located within the grain boundaries of the spinel top-layer, as was the case in the study Sattari et al. [88]). Furthermore, these analyses need to be done with respect to exposure duration, since Ce might migrate towards the surface. By combining dedicated microscopy with the results from the new ^{18}O-tracer experiment method a more fundamental understanding can be achieved of how the oxide scale growth mechanism is influenced by the Ce-coating.

8. References

[1]   I.E. Agency. *World Energy Outlook 2016*. 2016 [cited 2016; Available from: http://www.worldenergyoutlook.org/publications/weo-2016/.

[2]   M. Powell, K. Meinhardt, V. Sprenkle, L. Chick, and G. McVay, *Demonstration of a highly efficient solid oxide fuel cell power system using adiabatic steam reforming and anode gas recirculation.* Journal of Power Sources, 2012. **205**: p. 377-384.

[3]   A. Kirubakaran, S. Jain, and R.K. Nema, *A review on fuel cell technologies and power electronic interface.* Renewable & Sustainable Energy Reviews, 2009. **13**(9): p. 2430-2440.

[4]   A.B. Stambouli and E. Traversa, *Solid oxide fuel cells (SOFCs): a review of an environmentally clean and efficient source of energy.* Renewable & Sustainable Energy Reviews, 2002. **6**(5): p. 433-455.

[5]   E.D. Wachsman and K.T. Lee, *Lowering the Temperature of Solid Oxide Fuel Cells.* Science, 2011. **334**(6058): p. 935-939.

[6]   S.C. Singhal and K. Kendall, *High Temperature Solid Oxide Fuel Cells: Fundamentals, Design, and Applications*. 2003: Elsevier.

[7]   J.W. Fergus, *Metallic interconnects for solid oxide fuel cells.* Materials Science and Engineering a-Structural Materials Properties Microstructure and Processing, 2005. **397**(1-2): p. 271-283.

[8]   W.Z. Zhu and S.C. Deevi, *Opportunity of metallic interconnects for solid oxide fuel cells: a status on contact resistance.* Materials Research Bulletin, 2003. **38**(6): p. 957-972.

[9]   J.I. Gazzarri and O. Kesler, *Short-stack modeling of degradation in solid oxide fuel cells - Part I. Contact degradation.* Journal of Power Sources, 2008. **176**(1): p. 138-154.

[10]   J.W. Fergus, *Effect of cathode and electrolyte transport properties on chromium poisoning in solid oxide fuel cells.* International Journal of Hydrogen Energy, 2007. **32**(16): p. 3664-3671.

[11]   K. Hilpert, D. Das, M. Miller, D.H. Peck, and R. Weiss, *Chromium vapor species over solid oxide fuel cell interconnect materials and their potential for degradation processes.* Journal of the Electrochemical Society, 1996. **143**(11): p. 3642-3647.

[12]   E. Konysheva, et al., *Chromium poisoning of perovskite cathodes by the ODS alloy Cr5Fe1Y(2)O(3) and the high chromium ferritic steel Crofer22APU.* Journal of the Electrochemical Society, 2006. **153**(4): p. A765-A773.

[13]   S.P.S. Badwal, R. Deller, K. Foger, Y. Ramprakash, and J.P. Zhang, *Interaction between chromia forming alloy interconnects and air electrode of solid oxide fuel cells.* Solid State Ionics, 1997. **99**(3-4): p. 297-310.

[14]   H. Kurokawa, C.P. Jacobson, L.C. DeJonghe, and S.J. Visco, *Chromium vaporization of bare and of coated iron-chromium alloys at 1073 K.* Solid State Ionics, 2007. **178**(3-4): p. 287-296.

[15]   R. Trebbels, T. Markus, and L. Singheiser, *Investigation of Chromium Vaporization from Interconnector Steels with Spinel Coatings.* Journal of the Electrochemical Society, 2010. **157**(4): p. B490-B495.

[16]   A. Petric and H. Ling, *Electrical conductivity and thermal expansion of spinels at elevated temperatures.* Journal of the American Ceramic Society, 2007. **90**(5): p. 1515-1520.

[17]   N. Shaigan, W. Qu, D.G. Ivey, and W.X. Chen, *A review of recent progress in coatings, surface modifications and alloy developments for solid oxide fuel cell ferritic stainless steel interconnects.* Journal of Power Sources, 2010. **195**(6): p. 1529-1542.

[18]   S.R. Akanda, N.J. Kidner, and M.E. Walter, *Spinel coatings on metallic interconnects: Effect of reduction heat treatment on performance.* Surface & Coatings Technology, 2014. **253**: p. 255-260.

[19]   E. Alvarez, A. Meier, K.S. Weil, and Z.G. Yang, *Oxidation Kinetics of Manganese Cobaltite Spinel Protection Layers on Sanergy HT for Solid Oxide Fuel Cell Interconnect Applications.* International Journal of Applied Ceramic Technology, 2011. **8**(1): p. 33-41.

[20]   P.E. Gannon, et al., *Enabling inexpensive metallic alloys as SOFC interconnects: An investigation into hybrid coating technologies to deposit nanocomposite functional coatings on ferritic stainless steels.* International Journal of Hydrogen Energy, 2007. **32**(16): p. 3672-3681.

[21]   Y.Z. Hu, C.X. Li, G.J. Yang, and C.J. Li, *Evolution of microstructure during annealing of Mn1.5Co1.5O4 spinel coatings deposited by atmospheric plasma spray.* International Journal of Hydrogen Energy, 2014. **39**(25): p. 13844-13851.

[22]   N.J. Magdefrau, L. Chen, E.Y. Sun, and M. Aindow, *The effect of Mn1.5Co1.5O4 coatings on the development of near surface microstructure for Haynes 230 oxidized at 800 degrees C in air.* Surface & Coatings Technology, 2014. **242**: p. 109-117.

[23]   B.K. Park, et al., *Cu- and Ni-doped Mn1.5Co1.5O4 spinel coatings on metallic interconnects for solid oxide fuel cells.* International Journal of Hydrogen Energy, 2013. **38**(27): p. 12043-12050.

[24]   J. Puranen, et al., *Influence of powder composition and manufacturing method on electrical and chromium barrier properties of atmospheric plasma sprayed spinel coatings prepared from MnCo2O4 and Mn2CoO4 + Co powders on Crofer 22 APU interconnectors.* International Journal of Hydrogen Energy, 2014. **39**(30): p. 17246-17257.

[25]   A. Harthøj, T. Holt, and P. Møller, *Oxidation behaviour and electrical properties of cobalt/cerium oxide composite coatings for solid oxide fuel cell interconnects.* Journal of Power Sources, 2015. **281**(0): p. 227-237.

[26]   S. Canovic, et al., *Oxidation of Co- and Ce-nanocoated FeCr steels: A microstructural investigation.* Surface and Coatings Technology, 2013. **215**(0): p. 62-74.

[27]   J. Froitzheim, S. Canovic, M. Nikumaa, R. Sachitanand, L.G. Johansson, and J.E. Svensson, *Long term study of Cr evaporation and high temperature corrosion behaviour of Co coated ferritic steel for solid oxide fuel cell interconnects.* Journal of Power Sources, 2012. **220**: p. 217-227.

[28]   M. Stanislowski, et al., *Reduction of chromium vaporization from SOFC interconnectors by highly effective coatings.* Journal of Power Sources, 2007. **164**(2): p. 578-589.

[29]   A. Kruk, et al., *Effect of Co deposition on oxidation behavior and electrical properties of ferritic steel for solid oxide fuel cell interconnects.* Thin Solid Films, 2015. **590**: p. 184-192.

[30]   B. Pint. *Progress in understanding the reactive element effect since the Whittle and Stringer literature review*. in *Proceedings of the John Stringer Symposium. Edited by PF Tortorelli and PY Hou. ASM, Materials Park, OH*. 2003. Citeseer.

[31]   S. Chevalier, *What did we learn on the reactive element effect in chromia scale since Pfeil's patent?* Materials and Corrosion-Werkstoffe Und Korrosion, 2014. **65**(2): p. 109-115.

[32]   J.G. Grolig, J. Froitzheim, and J.E. Svensson, *Coated stainless steel 441 as interconnect material for solid oxide fuel cells: Oxidation performance and chromium evaporation.* Journal of Power Sources, 2014. **248**: p. 1007-1013.

[33]   S. Fontana, S. Chevalier, and G. Caboche, *Metallic Interconnects for Solid Oxide Fuel Cell: Performance of Reactive Element Oxide Coating During 10, 20 and 30 Months Exposure.* Oxidation of Metals, 2012. **78**(5-6): p. 307-328.

[34]   J. Larminie and A. Dicks, *Fuel Cell Systems Explained*. 2003: J. Wiley.

[35]   B.C.H. Steele and A. Heinzel, *Materials for fuel-cell technologies.* Nature, 2001. **414**(6861): p. 345-352.

[36]   A. Mai, *Fuel cell system development at HEXIS*, 2015, HEXIS.

[37]   K.K.a.M. Kendall, *High-Temperature Solid Oxide Fuel Cells for the 21st Century* ed. S. Edition). 2015: Elsevier.

[38]   K.T. Lee, H.S. Yoon, and E.D. Wachsman, *The evolution of low temperature solid oxide fuel cells.* Journal of Materials Research, 2012. **27**(16): p. 2063-2078.

[39]   B.C.H. Steele, *Appraisal of Ce1-yGdyO2-y/2 electrolytes for IT-SOFC operation at 500 degrees C.* Solid State Ionics, 2000. **129**(1-4): p. 95-110.

[40]   J.C.W. Mah, A. Muchtar, M.R. Somalu, and M.J. Ghazali, *Metallic interconnects for solid oxide fuel cell: A review on protective coating and deposition techniques.* International Journal of Hydrogen Energy.

[41]   W.J. Quadakkers, J. Piron-Abellan, V. Shemet, and L. Singheiser, *Metallic interconnectors for solid oxide fuel cells - a review.* MATERIALS AT HIGH TEMPERATURES, 2003. **20**(2): p. 115-128.

[42]   Elcogen. *ELCOGEN. FUTURE TECHNOLOGY AVAILABLE TODAY.*; Available from: http://www.elcogen.com/images/pdf4.pdf.

[43]   P. Kofstad, *High Temperature Corrosion.* Elsevier Applied Science, 1988.

[44]   D.J. Young, *High Temperature Oxidation and Corrosion of Metals* ed. S. Edition. 2016: Elsevier Ltd.

[45]   D.J. Young, *High Temperature Oxidation and Corrosion of Metals*. 2008: Elsevier.

[46]   H.J.T. Ellingham, *Reducibility of oxides and sulphides in metallurgical processes.* Journal of the Society of Chemical Industry, 1944. **63**(5): p. 125-160.

[47]   T. Jonsson, B. Pujilaksono, A. Fuchs, J.E. Svensson, L.G. Johansson, and M. Halvarsson, *The influence of H(2)O on iron oxidation at 600 degrees C: A microstructural study.* High Temperature Corrosion and Protection of Materials 7, Pts 1 and 2, 2008. **595-598**: p. 1005-1012.

[48]   N. Birks, G.H. Meier, and F.S. Pettit, *Introduction to the high temperature oxidation of metals*. 2006: Cambridge University Press.

[49]   U.o. Cambridge, *Ellingham diagram.*

[50]   A.R. West, *Basic solid state chemistry*. 1999: John Wiley & Sons.

[51]   H. Mehrer, *Diffusion in Solids: Fundamentals, Methods, Materials, Diffusion-Controlled Processes*. 2007: Springer.

[52]   A. Muan and S. Somiya, *Phase Relations in the System Iron Oxide-Cr2o3 in Air.* Journal of the American Ceramic Society, 1960. **43**(4): p. 204-209.

[53]   C.S. Tedmon, *Effect of Oxide Volatilization on Oxidation Kinetics of Cr and Fe-Cr Alloys.* Journal of the Electrochemical Society, 1966. **113**(8): p. 766-&.

[54]   B.B. Ebbinghaus, *Thermodynamics of Gas-Phase Chromium Species - the Chromium Oxides, the Chromium Oxyhydroxides, and Volatility Calculations in Waste Incineration Processes.* Combustion and Flame, 1993. **93**(1-2): p. 119-137.

[55]   C. Gindorf, L. Singheiser, and K. Hilpert, *Vaporisation of chromia in humid air.* Journal of Physics and Chemistry of Solids, 2005. **66**(2-4): p. 384-387.

[56]   E.J. Opila, et al., *Theoretical and experimental investigation of the thermochemistry of CrO2(OH)(2)(g).* Journal of Physical Chemistry A, 2007. **111**(10): p. 1971-1980.

[57]   J. Froitzheim, H. Ravash, E. Larsson, L.G. Johansson, and J.E. Svensson, *Investigation of Chromium Volatilization from FeCr Interconnects by a Denuder Technique.* Journal of the Electrochemical Society, 2010. **157**(9): p. B1295-B1300.

[58]   A. Holt and P. Kofstad, *Electrical-Conductivity and Defect Structure of Cr2o3 .2. Reduced Temperatures (Less-Than-Similar-to-1000-Degrees-C).* Solid State Ionics, 1994. **69**(2): p. 137-143.

[59]   L. Latu-Romain, et al., *The Role of Oxygen Partial Pressure on the Nature of the Oxide Scale on a NiCr Model Alloy.* Oxidation of Metals, 2016: p. 1-13.

[60]   H. Nagai, T. Fujikawa, and K. Shoji, *Electrical-Conductivity of Cr2o3 Doped with La2o3, Y2o3 and Nio.* Transactions of the Japan Institute of Metals, 1983. **24**(8): p. 581-588.

[61]   A. Holt and P. Kofstad, *Electrical conductivity and defect structure of Mg-doped Cr2O3.* Solid State Ionics, 1997. **100**(3-4): p. 201-209.

[62]   A. Holt and P. Kofstad, *Electrical conductivity of Cr2O3 doped with TiO2.* Solid State Ionics, 1999. **117**(1-2): p. 21-25.

[63]   S.P. Simner, M.D. Anderson, G.G. Xia, Z. Yang, L.R. Pederson, and J.W. Stevenson, *SOFC performance with Fe-Cr-Mn alloy interconnect.* Journal of the Electrochemical Society, 2005. **152**(4): p. A740-A745.

[64]   M.C. Tucker, H. Kurokawa, C.P. Jacobson, L.C. De Jonghe, and S.J. Visco, *A fundamental study of chromium deposition on solid oxide fuel cell cathode materials.* Journal of Power Sources, 2006. **160**(1): p. 130-138.

[65]   Y. Matsuzaki and I. Yasuda, *Dependence of SOFC cathode degradation by chromium-containing alloy on compositions of electrodes and electrolytes.* Journal of the Electrochemical Society, 2001. **148**(2): p. A126-A131.

[66]   R. Sachitanand, M. Sattari, J.E. Svensson, and J. Froitzheim, *Evaluation of the oxidation and Cr evaporation properties of selected FeCr alloys used as SOFC interconnects.* International Journal of Hydrogen Energy, 2013. **38**(35): p. 15328-15334.

[67]   B.A. Pint, *Experimental observations in support of the dynamic-segregation theory to explain the reactive-element effect.* Oxidation of Metals, 1996. **45**(1-2): p. 1-37.

[68]   J. Quadakkers and L. Singheiser, *Practical aspects of the reactive element effect.* High Temperature Corrosion and Protection of Materials 5, Pts 1 and 2, 2001. **369-3**: p. 77-92.

[69]   W.J. Quadakkers, H. Holzbrecher, K.G. Briefs, and H. Beske, *Differences in Growth Mechanisms of Oxide Scales Formed on Ods and Conventional Wrought Alloys.* Oxidation of Metals, 1989. **32**(1-2): p. 67-88.

[70]   M. Stanislowski, E. Wessel, K. Hilpert, T. Markus, and L. Singheiser, *Chromium vaporization from high-temperature alloys I. Chromia-forming steels and the influence of outer oxide layers.* Journal of the Electrochemical Society, 2007. **154**(4): p. A295-A306.

[71]   C. Collins, et al., *Chromium volatility of coated and uncoated steel interconnects for SOFCs.* Surface & Coatings Technology, 2006. **201**(7): p. 4467-4470.

[72]   J. Froitzheim and J.E. Svensson, *Multifunctional Nano-Coatings for SOFC Interconnects.* Solid Oxide Fuel Cells 12 (Sofc Xii), 2011. **35**(1): p. 2503-2508.

[73]   J.H. Xiao, W.Y. Zhang, C.Y. Xiong, B. Chi, J. Pu, and L. Jian, *Oxidation behavior of Cu-doped MnCo2O4 spinel coating on ferritic stainless steels for solid oxide fuel cell interconnects.* International Journal of Hydrogen Energy, 2016. **41**(22): p. 9611-9618.

[74]   C. Macauley, P. Gannon, M. Deibert, and P. White, *The influence of pre-treatment on the oxidation behavior of Co coated SOFC interconnects.* International Journal of Hydrogen Energy, 2011. **36**(7): p. 4540-4548.

[75]   X.H. Deng, P. Wei, M.R. Bateni, and A. Petric, *Cobalt plating of high temperature stainless steel interconnects.* Journal of Power Sources, 2006. **160**(2): p. 1225-1229.

[76]   J. Froitzheim, et al., *Nano Coated Interconnects for SOFC (NaCoSOFC).* Solid Oxide Fuel Cells 13 (Sofc-Xiii), 2013. **57**(1): p. 2187-2193.

[77]   C.M. Cotell, G.J. Yurek, R.J. Hussey, D.F. Mitchell, and M.J. Graham, *The Influence of Grain-Boundary Segregation of Y in Cr2o3 on the Oxidation of Cr Metal .2. Effects of Temperature and Dopant Concentration.* Oxidation of Metals, 1990. **34**(3-4): p. 201-216.

[78]   E.A. Polman, T. Fransen, and P.J. Gellings, *The Reactive Element Effect - Ionic Processes of Grain-Boundary Segregation and Diffusion in Chromium-Oxide Scales.* Journal of Physics-Condensed Matter, 1989. **1**(28): p. 4497-4510.

[79]   D.E. Alman and P.D. Jablonski, *Effect of minor elements and a Ce surface treatment on the oxidation behavior of an Fe-22Cr-0.5Mn (Crofer 22 APU) ferritic stainless steel.* International Journal of Hydrogen Energy, 2007. **32**(16): p. 3743-3753.

[80]   H. Falk-Windisch, I. Mertzidis, J.E. Svensson, and J. Froitzheim. *Pre-coated Ce/Co-coated steel: Mitigating Cr vaporization, increasing corrosion resistance at competitive cost*. in *ECS Transactions*. 2015.

[81]   J.G. Grolig, J. Froitzheim, and J.-E. Svensson, *Coated stainless steel 441 as interconnect material for solid oxide fuel cells: Evolution of electrical properties.* Journal of Power Sources, 2015. **284**(0): p. 321-327.

[82]   A. Magrasó, H. Falk-Windisch, J. Froitzheim, J.-E. Svensson, and R. Haugsrud, *Reduced long term electrical resistance in Ce/Co-coated ferritic stainless steel for solid oxide fuel cell metallic interconnects.* International Journal of Hydrogen Energy, 2015. **40**(27): p. 8579-8585.

[83]   W. Qu, L. Jian, D.G. Ivey, and J.M. Hill, *Yttrium, cobalt and yttrium/cobalt oxide coatings on ferritic stainless steels for SOFC interconnects.* Journal of Power Sources, 2006. **157**(1): p. 335-350.

[84]   W. Qu, H. Li, and D.G. Ivey, *Sol-gel coatings to reduce oxide growth in interconnects used for solid oxide fuel cells.* Journal of Power Sources, 2004. **138**(1-2): p. 162-173.

[85]   R.F. Egerton, *Physical Principles of Electron Microscopy, An Introduction to TEM, SEM, and AEM*. 2016: Springer International Publishing.

[86] K.L. Scrivener, *Backscattered electron imaging of cementitious microstructures: understanding and quantification.* Cement & Concrete Composites, 2004. **26**(8): p. 935-945.

[87] C.B.C. David B Williams, *Transmission Electron Microscopy - Part4: Spectrometry.* 2009: Springer.

[88] M. Sattari, R. Sachitanand, J. Froitzheim, J.E. Svensson, and T. Jonsson, *The effect of Ce on the high temperature oxidation properties of a Fe-22% Cr steel: microstructural investigation and EELS analysis.* Materials at High Temperatures, 2015. **32**(1-2): p. 118-122.

[89] L.E.S.a.E.A. Moore, *Solid State Chemistry: An Introduction (Third Edition)*, ed. T. Edition. 2005: CRC Press.

[90] G. Gauglitz, *Ultraviolet and Visible Spectroscopy*, in *Ullmann's Encyclopedia of Industrial Chemistry*. 2000, Wiley-VCH Verlag GmbH & Co. KGaA.

[91] H. Nygren and P. Malmberg, *High resolution imaging by organic secondary ion mass spectrometry.* Trends in Biotechnology, 2007. **25**(11): p. 499-504.

[92] P. Hoppe, S. Cohen, and A. Meibom, *NanoSIMS: Technical Aspects and Applications in Cosmochemistry and Biological Geochemistry.* Geostandards and Geoanalytical Research, 2013. **37**(2): p. 111-154.

[93] B. Pujilaksono, T. Jonsson, M. Halvarsson, I. Panas, J.E. Svensson, and L.G. Johansson, *Paralinear oxidation of chromium in O(2)+H(2)O environment at 600-700 degrees C.* Oxidation of Metals, 2008. **70**(3-4): p. 163-188.

[94] B. Hua, Y.H. Kong, W.Y. Zhang, J. Pu, B. Chi, and L. Jian, *The effect of Mn on the oxidation behavior and electrical conductivity of Fe-17Cr alloys in solid oxide fuel cell cathode atmosphere.* Journal of Power Sources, 2011. **196**(18): p. 7627-7638.

[95] F.H. Stott, F.I. Wei, and C.A. Enahoro, *The Influence of Manganese on the High-Temperature Oxidation of Iron-Chromium Alloys.* Werkstoffe Und Korrosion-Materials and Corrosion, 1989. **40**(4): p. 198-205.

[96] I.H. Jung, *Critical evaluation and thermodynamic modeling of the Mn-Cr-O system for the oxidation of SOFC interconnect.* Solid State Ionics, 2006. **177**(7-8): p. 765-777.

[97] T. Brylewski, J. Dabek, and K. Przybylski, *Oxidation kinetics study of the iron-based steel for solid oxide fuel cell application.* Journal of Thermal Analysis and Calorimetry, 2004. **77**(1): p. 207-216.

[98] H. Hindam and D.P. Whittle, *Microstructure, Adhesion and Growth-Kinetics of Protective Scales on Metals and Alloys.* Oxidation of Metals, 1982. **18**(5-6): p. 245-284.

[99] E.A. Gulbransen and K.F. Andrew, *Kinetics of the Oxidation of Chromium.* Journal of the Electrochemical Society, 1957. **104**(6): p. 334-338.

[100] A.M. Huntz, et al., *Oxidation of AISI 304 and AISI 439 stainless steels.* Materials Science and Engineering a-Structural Materials Properties Microstructure and Processing, 2007. **447**(1-2): p. 266-276.

[101] A.C.S. Sabioni, et al., *Atmosphere dependence of oxidation kinetics of unstabilized and Nb-stabilized AISI 430 ferritic stainless steels in the temperature range 850-950 degrees C.* Materials at High Temperatures, 2010. **27**(2): p. 89-96.

[102] A.W.B. Skilbred and R. Haugsrud, *Sandvik Sanergy HT - A potential interconnect material for LaNbO4-based proton ceramic fuel cells.* Journal of Power Sources, 2012. **206**: p. 70-76.

[103] W.C. Hagel and A.U. Seybolt, *Cation Diffusion in Cr2o3.* Journal of the Electrochemical Society, 1961. **108**(12): p. 1146-1152.

[104] I. Panas, J.E. Svensson, H. Asteman, T.J.R. Johnson, and L.G. Johansson, *Chromic acid evaporation upon exposure of Cr2O3(S) to H2O(g) and O-2(g) - mechanism from first principles.* Chemical Physics Letters, 2004. **383**(5-6): p. 549-554.

[105] J.G. Grolig, J. Froitzheim, and J.E. Svensson, *Effect of Cerium on the Electrical Properties of a Cobalt Conversion Coating for Solid Oxide Fuel Cell Interconnects - A Study Using Impedance Spectroscopy.* Electrochimica Acta, 2015. **184**: p. 301-307.

[106] Z.G. Lu, J.H. Zhu, E.A. Payzant, and M.P. Paranthaman, *Electrical conductivity of the manganese chromite spinel solid solution.* Journal of the American Ceramic Society, 2005. **88**(4): p. 1050-1053.

[107] N. Sakai, et al., *Material transport and degradation behavior of SOFC interconnects.* Solid State Ionics, 2006. **177**(19-25): p. 1933-1939.

[108] S. Chevalier, G. Caboche, K. Przybylski, and T. Brylewski, *Effect of nano-layered ceramic coatings on the electrical conductivity of oxide scale grown on ferritic steels.* Journal of Applied Electrochemistry, 2009. **39**(4): p. 529-534.

[109] J.H. Park and K. Natesan, *Electronic Transport in Thermally Grown Cr2o3.* Oxidation of Metals, 1990. **33**(1-2): p. 31-54.

[110] K.Q. Huang, P.Y. Hou, and J.B. Goodenough, *Characterization of iron-based alloy interconnects for reduced temperature solid oxide fuel cells.* Solid State Ionics, 2000. **129**(1-4): p. 237-250.

[111] M. Linder, et al., *Model-based prediction of the ohmic resistance of metallic interconnects from oxide scale growth based on scanning electron microscopy.* Journal of Power Sources, 2014. **272**: p. 595-605.

[112] L. Chen, E.Y. Sun, J. Yamanis, and N. Magdefrau, *Oxidation Kinetics of Mn1.5Co1.5O4-Coated Haynes 230 and Crofer 22 APU for Solid Oxide Fuel Cell Interconnects.* Journal of the Electrochemical Society, 2010. **157**(6): p. B931-B942.

[113] Y. Zhang, A. Javed, M.M. Zhou, S.Q. Liang, and P. Xiao, *Fabrication of Mn-Co Spinel Coatings on Crofer 22 APU Stainless Steel by Electrophoretic Deposition for Interconnect Applications in Solid Oxide Fuel Cells.* International Journal of Applied Ceramic Technology, 2014. **11**(2): p. 332-341.

[114] F.Y. Shen and K. Lu, *CoxFe1-x oxide coatings on metallic interconnects for solid oxide fuel cells.* Journal of Power Sources, 2016. **330**: p. 231-239.

[115] A.M. Dayaghi, M. Askari, H. Rashtchi, and P. Gannon, *Fabrication and high-temperature corrosion of sol-gel Mn/Co oxide spinel coating on AISI 430.* Surface & Coatings Technology, 2013. **223**: p. 110-114.

[116] D.J. Young, J. Zurek, L. Singheiser, and W.J. Quadakkers, *Temperature dependence of oxide scale formation on high-Cr ferritic steels in Ar-H-2-H2O.* Corrosion Science, 2011. **53**(6): p. 2131-2141.

[117] Battelle, *MANUFACTURING COST ANALYSIS OF 1 KW AND 5 KW SOLID OXIDE FUEL CELL (SOFC) FOR AUXILLIARY POWER APPLICATIONS*, 2014, Battelle Memorial Institute.

[118] P. Papaiacovou, R.J. Hussey, D.F. Mitchell, and M.J. Graham, *The Effect of Ceo2 Coatings on the Oxidation Behavior of Fe-20cr Alloys in O-2 at 1173-K.* Corrosion Science, 1990. **30**(4-5): p. 451-&.

[119] K.P.R. Reddy, J.L. Smialek, and A.R. Cooper, *O-18 Tracer Studies of Al2o3 Scale Formation on Nicral Alloys.* Oxidation of Metals, 1982. **17**(5-6): p. 429-449.